Imperial College London

Advanced damage modelling of free machining steels

A Thesis submitted for the Degree of Doctorate of Philosophy of Imperial College London

by
Michael Kaye

2012

Supervised by:
Dr Daniel Balint
Professor Jianguo Lin
Dr Didier Farrugia

Department of Mechanical Engineering
Mechanics of Materials Division

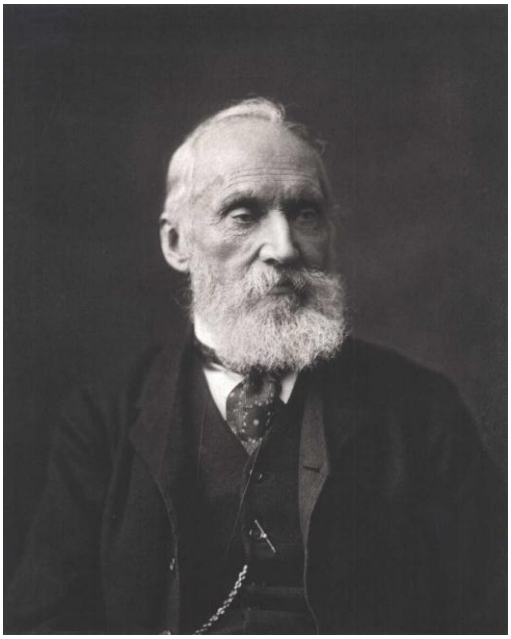

When you can measure what you are speaking about, and express it in numbers, you know something about it; but when you cannot measure it, when you cannot express it in numbers, your knowledge of it is of a meager and unsatisfactory kind; it may be the beginning of knowledge, but you have scarcely, in your thoughts, advanced it to the stage of science.

Sir William Thompson, Lord Kelvin (1824-1907)

Acknowledgments

I would like to express my sincere thanks to Prof. J Lin, and Dr. D. Balint for their support and advice during this project.

I would like to thank my family, co-workers and especially Mirella who helped me in the PhD process. My thanks go to P. Zhang, M. Mohamed and M. Karimpour in particular for our good discussions, their advice and helping with the code written for this project.

The microtomographic investigation was possible due to the time given to us by Prof. P. Lee. I would like to give a special thanks to Chedtha Puncreabator who helped immensely with the analysis of the raw data.

Dr. Didier Farrugia, of Tata steel, supplied the industrial problem. He has been a gold mine for good ideas for this project as well as supplying the test material and assistance.

The work was financed by an EPSRC in partnership with Tata steel. I hope that this excellent partnership continues to finance students through their postgraduate education.

Diamond-Light-Source's I-12 Beamline for materials support and facilities, and Robert C. Atwood and Richard W. Hamilton for help with image reconstruction and running the synchrotron experiments.

Abstract

The current available damage models do not accurately predict effective plastic strain to failure in low triaxiality stress states. A damage model was developed for low triaxiality that is appropriate to hot rolling of steel.

This work focuses on nucleation and growth of damage as well as the effect of the strain and stress path. The latter is especially important for the rolling of bar and other complex cross-section products. A study of damage mechanisms and methods to model them has been undertaken. It is pointed out that the many models are only useful under certain conditions but can be used when the expected damage mechanisms are active.

Several test types were evaluated to assess their ability to simulate stress state in rolling. A program has been written to evaluate the stress state for plane and axisymmetric tests, which allows one to choose the most appropriate test-piece geometry. A test has been designed and implemented. Thermal and mechanical data was gathered, which has been used to relate the stress triaxiality to damage growth and identify appropriate damage growth models.

The size and spacing distributions of inclusions in free cutting steels have been measured. The different distributions have an effect on the ductility of the different steels. This effect has been found to change at different strain rates and temperatures. By better accounting for the effect of inclusions on damage growth under a range of test conditions, the damage model can be significantly improved.

Free cutting steels that contained different additions of heavy metals were tested. The ductility and damage mechanisms were compared in each of the steels. The effect of the precipitation of the different heavy metals at the inclusion to matrix boundary was highlighted. The same damage mechanisms were observed in each steel but the ability to accommodate damage varied between the steels.

Ex-situ synchrotron x-ray micro-tomography was used to better measure and quantify the distribution of inclusions and damage evolution in a free cutting steel. Localised damage coalescence away from the centre of the uniaxial tensile test-piece was attributed to the effect of inclusion clustering.

This research was used to develop a realistic damage model, which can predict damage growth and coalescence for a range of forming parameters and different stress-state conditions related to hot rolling applications. The micro-mechanics based model includes the effects of inclusion distribution on damage. The model is calibrated using twenty six temperature based material constants.

Nomenclature

a_x	material constant
A_x	Material constant in Liu's damage model
b	material constant
B	Boltzmann constant (Watts.m^{-2}.K^{-4})
c_x	Material constant for recovery
C_p	Specific heat at constant pressure (J.mol^{-1}.K^{-1})
d	Grain size (μm)
d_x	Material constant exponent in Liu's damage model
D	Damage area fraction
$\mathbf{D}$	Damage tensor
e_{mis}	Emissivity
E	Young's Modulus (GPa)
f	Void volume fraction (Gurson model)
f_n	Volume fraction of potential void nucleation sites
f_g	Volume fraction of void growth
f_c	Critical void volume fraction
f_f	Void volume fraction at final fracture
H	Hardening term
k_0	Yield stress in shear (MPa)
k_x	Material constant
K	Drag stress (MPa)
l	Distance between voids (μm)
m	Mass (kg), Taylor factor
n	Hardening exponent
n_x	Material constant
P	Heat emitted (Watts/m^2)
q_x	Material constant for GTN model
Q	Energy (J)
Q_x	Activation energies (J.mol^{-1})
r_d	Void diameter (μm)
r	Equivalent inclusion radius (μm)
R	Isotropic hardening (MPa)
S	Cross sectional area (m^2)
S_D	Cross sectional area of damage (m^2)
t	Time (s)
t_{rec}	Interrupt time (s)
T	Temperature (K unless stated as °C)
T_m	Material melting temperature (°C)
V	Void volume fraction
x	Subscript, integer
y	Damage strain energy release rate
z_x	Material constant for damage model

α	Material constant
β	Scalar damage variable
E	Total equivalent strain
ε_f	Plastic equivalent strain to failure
ε_f^{uni}	Plastic equivalent strain to failure in uniaxial tension
ε_{IC}	Max principle strain at intervoid matrix
ε_p	Plastic equivalent strain
ε_{eq}	Elastic equivalent strain
γ	Shear strain
γ_y	Shear strain in yield
γ_x	Material constant for exponents in damage model
λ	Spacing between inclusions (μm)
ϕ	Inclusions' nearest neighbour (μm)
ρ_d	Dislocation density
$\overline{\rho}$	Normalised dislocation density
φ	Potential of dissipation
σ	Stress (MPa)
σ_{crit}	Critical stress for decohesion (MPa)
σ_{eq}	Equivalent stress (MPa)
σ_{field}	Far field stress (MPa)
σ_m	Hydrostatic stress (MPa)
σ_y	Yield stress (MPa)
σ_1	Maximum principal stress (MPa)
σ_{IC}	Plastic limit load stress (MPa)
ν	Poisson's ratio
ω_x	Inclusion distribution factor
Ω	Inclusion distribution factor

Table of contents

List of figures

Chapter 1 Motivation for project

1.1 Introduction

The following describes the global steel industry, expected future trends and how they relate to the current research project. Some prevalent problems with the hot rolling of free cutting steels are presented. The general aims of, and the motivations for, the research are discussed.

1.2 Global and UK steel industry and research

The UK has much strength in its manufacturing but the rest of the world is not standing still. Research into manufacturing is one of the ways the UK government is aiming to improve the organic growth of business (BIS 2010). The share of the UK economy taken up by manufacturing has declined. However, over the past three decades the value of the goods has increased and up to the economic downturn of 2007 there was strong economic growth in manufacturing, with output being a third higher than in 1980, as shown in Figure 1.1.

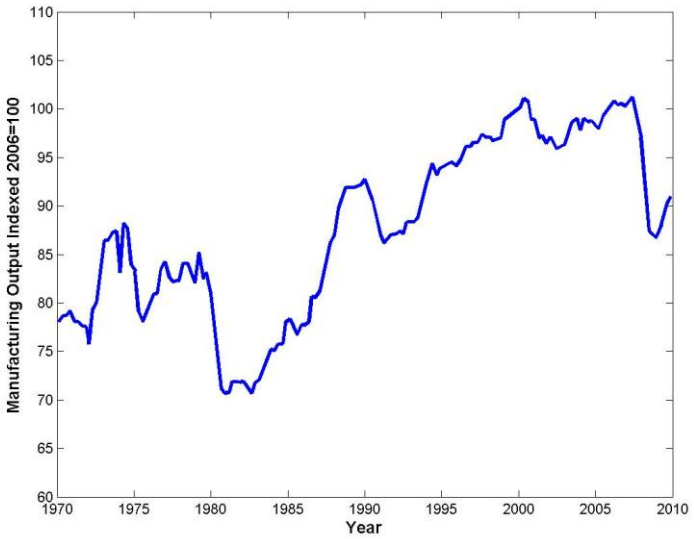

Figure 1.1. Manufacturing industries' output, indexed where 2006 value is 100.

The UK can only effectively compete in high added value products due to its generally high wages (BIS 2010). Changing demographics will soon offer new market opportunities. With India's economy growing at 7% and China's at 9%, there will be huge opportunities for high added value products in the global market place. Research is essential to grow the economy, accommodate unforeseen events and stay competitive with high added value products.

Steel is a versatile material which has good strength, formability and machinability. It is readily available as its main constituent, iron, is ubiquitous on earth. Steel can be used for construction, aerospace and many other varied applications. Corus, which used to be Europe's largest steel producer, was purchased by Tata steel in 2007. Arcelor Mittal has been the largest single steel producer for several years due to their merging in 2006; the steel production rankings are shown in Figure 1.2. This conglomeration of companies is expected due to global pressures.

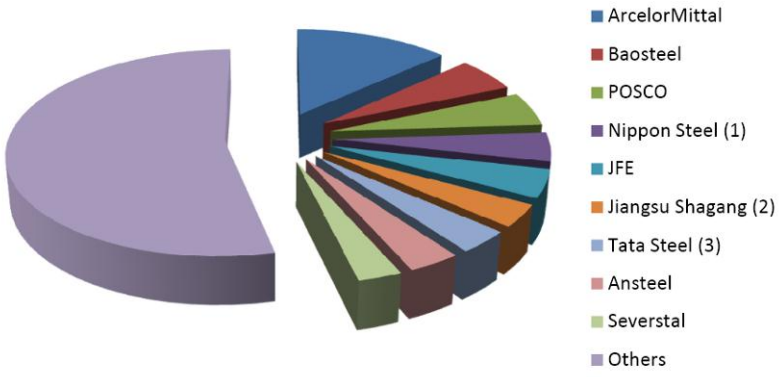

Figure 1.2. World steel producers 2009 Source (WSA 2009). [1]

[1] (1) does not include share of Usiminas production (1.6 mmt)
(2) does not include Yonglian (4.4 mmt) and Xixing (1.4 mmt)
(3) includes Corus and NatSteel
mmt = million metric ton

One way steel manufacturers maintain their position is by retaining quality. This requires that damage generated during production is obviated. This will ensure the specified in-service ductility, strength, fatigue lifetime and creep lifetime are met.

1.3 Problem description

Ideally, steel utilized in rolling processes should be ductile; Schey suggested that ductility exhaustion is a key reason for edge cracking in hot rolling of steel (Schey 1966). Typically, higher ductility implies a softer material, therefore a lower rolling force will be required and possibly less wear on the rolls (Kalpakjian 1984). However, rolled steel may also need to be machined, and a ductile material would have a poor surface finish. Thus, a compromise in chemical composition and processing treatments must be reached.

When machining low-carbon steels, adding quantities of bismuth, tellurium and lead improves chip formation and enhances surface quality as they act as internal lubricants. Nevertheless, the previously mentioned additions lower the ductility. Therefore any rolling with these additions, even at high temperatures, will be prone to edge cracking or crocodiling (Kalpakjian 1984; Hwang, Lee et al. 2005). This will be equally true for processing heat-treatable, bearing, forging and stainless steels. When the steel is damaged it must be removed, which decreases product yield and thereby increases costs. This makes it exceptionally important to be able to predict how a material will react to processing. Predictions can be realised with a model that is based on the underlying mechanisms.

1.4 Aims of research

This thesis focuses on nucleation and growth of damage in hot rolling applications and the effect of the strain and stress path (i.e. triaxiality inversion). The latter is especially important for the rolling of bar and other complex cross-section products. The objective of this research is to develop a mechanistic model to predict deformation and damage features during hot forming of steel.

1.5 Outline of thesis

Chapter 2 reviews the rolling process and the applicable material mechanisms. The fundamental aspects of the deformation and softening mechanisms are discussed. Chapter 3 uses this information to identify the relevant damage mechanisms, the models that capture these and the models' shortcomings.

In order to achieve the required understanding, a new test-piece design was created to establish damage initiation and growth mechanisms under stress states representative of those in hot rolling. Chapter 4 discusses a series of deformed specimens that were studied at macroscopic and microscopic levels. The deformation and damage mechanisms were examined. The damage was measured from the micrographs using digital methods and then related to the stress state using finite-element models. Based on previous research, and the enlightenment from the information gathered in testing, the governing mechanisms and relevant interactions were established.

Chapters 5 to 7 describe uniaxial tensile tests that were conducted on the same free cutting steels. The material responses at different temperatures and strain rates were recorded. Following this, the microstructure of the deformed samples was examined using a variety of methods to establish the evolution of features during deformation. The methods included scanning electron microscopy, x-ray microtomography and standard optical microscopy.

Chapter 8 details the constitutive model, which takes into account the key microstructural features, such as grain size, dislocation density, and inclusion or precipitate volume fraction and size. Interplay of mechanisms and microstructural features were modelled using unified viscoplastic damage constitutive equations, which were implemented into finite-element analysis (FEA) software. The equations were calibrated based on uniaxial tensile tests.

Chapter 2 The rolling process

2.1 Introduction

In the following section, the fundamental aspects of the industrial rolling process are given and information directly from engineers at the foundry is presented. The applicable deformation mechanisms are described. There is a focus on the dominant damage mechanisms expected in hot rolling and the significant parameters affecting ductility. The final section details methods to inhibit and prevent damage.

2.2 Background

Rolling is a forming operation, where billets (round cross-section) and bloom and slab (square cross-section) are passed between rolls, which can be used to change the cross-sectional shape and reduce the thickness. Rolling can be undertaken in ambient conditions or at high temperatures. Cold forming occurs at less than thirty percent of the melting temperature, T_m, warm forming occurs between thirty and seventy percent of T_m and hot forming occurs above seventy percent of T_m. Hot rolling is often used on an as-cast material as it removes the dendritic structure and coarse, non-uniform grains, creating a wrought structure with a finer grain size and reduced porosity. After pickling or scarfing to remove scale, cold rolling is sometimes performed after hot rolling to improve the strength, surface finish and tolerances.

It has been reported by Kalpakjian that during a rolling operation, isotropic phenomena occur in the material but as elongation of grains occurs anisotropy is increased and must be taken into account (Kalpakjian 1984). The surface is hardened, leading to a greater stiffness and resistance in the thickness direction. The fibres are oriented in the rolling direction, changing directional response in the sheet plane. This thesis will focus on the isotropic phenomena and in particular the issue of ductility.

2.2.1 Parameters in the rolling process

The equivalent strain rate experienced by the bloom during rolling alters with the rolls' rotation speed, separation distance and radius. In the initial stages the material has a lower velocity through the rolls and lower strain rates are experienced. As the material is compressed the velocity increases. Therefore if the same amount of straining takes place as in the previous roll set, then the strain rate would be higher. It must be noted that increased strain rate can adversely affect material properties. The strain rate is reduced predominantly by increasing the separation distance of the rolls. Nevertheless the strain rate alters significantly during rolling and it will range between 0.1 s^{-1} and 10 s^{-1}.

2.2.2 Typical deformation routes in rolling

The size of the rolls will alter how the billet is strained. Larger rolls will deform more of the bulk while smaller rolls predominantly deform the bloom material closer to the rolls. The blooms are passed through several different rolls, which rotate about different axes. This allows the generation of complex cross-section products. It also propagates complex stress states.

Larger rolls tend to create larger average stresses but there is also more contact between the rolls and the billet leading to surface tension. This creates a range of stresses within the billet during forming. There is often a stress distribution and spatial inversion of stress similar to that shown in Figure 2.1. As the billet progresses through the rolls, the stress state in a particular location changes. The geometry of the material affects the stress state during the process. This creates a range of stress triaxialities both compressive and tensile, the effect of which is still not fully understood (Gao, Zhang et al. 2010).

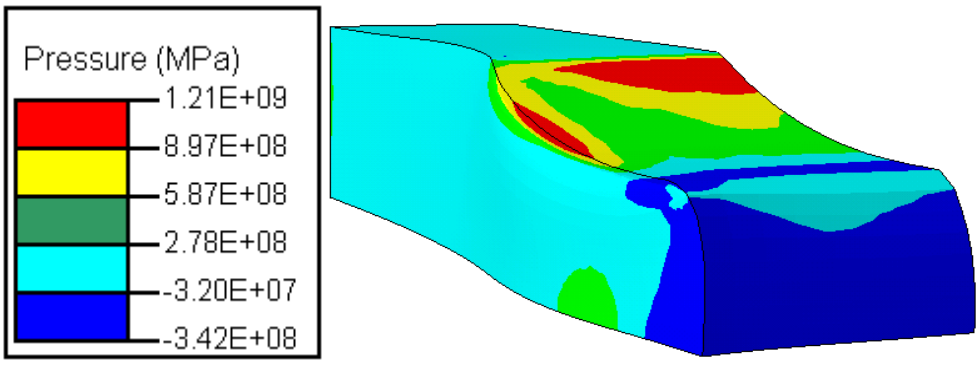

Figure 2.1. Distribution of pressure, σ_m, in a rolled billet.

2.2.3 Temperature profile of billet during rolling

The billets are reheated in a furnace prior to high-temperature rolling, which homogenises the microstructure. At the exit of the furnace the material is at 1200 °C. An oxide layer forms on the billet surface, which is removed using a roughing mill and blasted off using high pressure steam jets. These processes, combined with radiative cooling, cause the billet to cool. The heat generated due to deformation at each roll stand decreases the rate of cooling. The material exits the final roll stand at roughly 900 °C.

The cooling causes a temperature gradient within the billet. Since there are many temperature-related phenomena, such as annealing processes and creep, the temperature gradient has a significant effect on the range of material response. The graph shown in Figure 2.2 shows the ductility of a free cutting steel at various temperatures. The lower ductility in the trough at around 800 °C is identifiable. The higher temperatures permit greater ductility, until close to the melting temperature, as the material can better accommodate the deformation. It is clear that temperature has a significant effect on ductility.

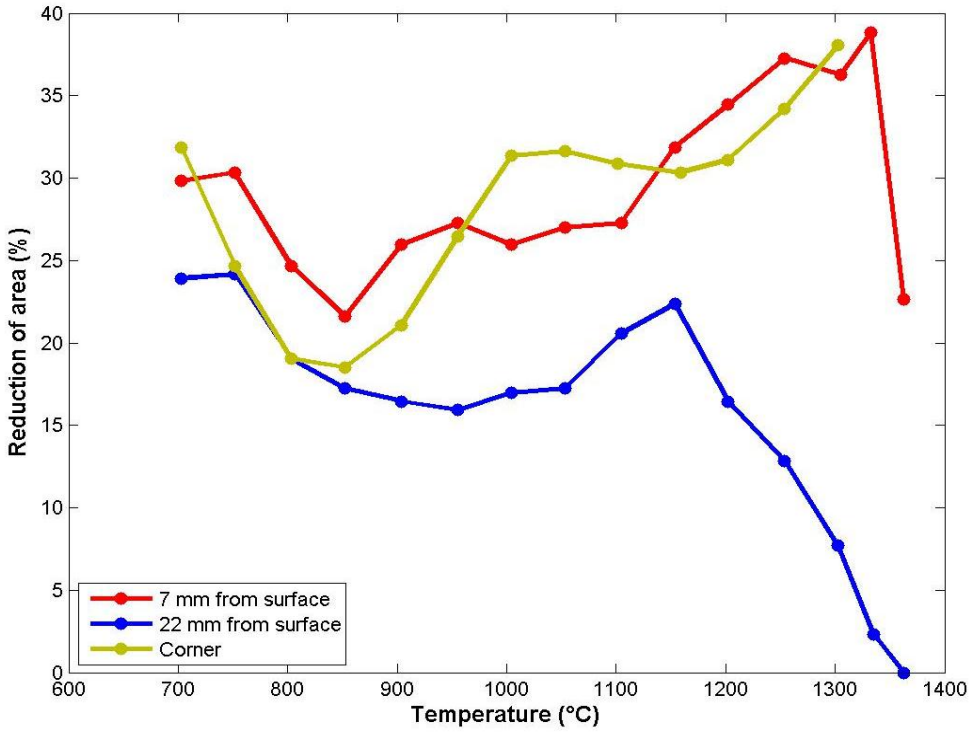

Figure 2.2. Tensile ductility of steel, 9SMn28, versus temperature (material taken from different locations in an as-cast billet), adapted from (Farrugia, Baillie et al. 2007).

2.3 Deformation mechanisms

The temperatures and strain rates experienced permit a range of deformation mechanisms. Knowledge of these underlying *deformation* mechanisms aids in the understanding of the active *damage* mechanisms. Several fundamental aspects of deformation, hardening and softening behaviour are discussed in the following sections.

2.3.1 Dislocations

The theory of dislocations as a means to understand the behaviour of ductile materials was first proposed by Volterra in 1905 (Volterra 1905). Taylor, and independently Orowan and Potanyi, created a description of dislocations for plastic deformation in 1934, and later many models for dislocations have been put forward, these have been reviewed in the following: (Hirth. John. and Jens 1992; Andrade Pires, de Souza Neto et al. 2004). Dislocations are line defects that come in two classes: edge and screw. A range of a material's mechanical properties and processes are based in some way on dislocations (Fionn and Petrinic 2005). An excellent introduction to some dislocation processes is presented in (Ashby and Jones 1996). A fundamental concept is that work hardening is primarily due to the decrease in mobility of dislocations and their mutual interactions. Hardening is also affected by grain growth and grain boundary rotation (Lin and Dunne 2001). Dislocation movement is resisted by an intrinsic lattice resistance, an obstructing effect of secondary and tertiary particles and the increase in dislocation density and hence tangling. The blockages can be overcome via sufficient applied stresses and diffusive mechanisms.

There are two mechanisms for diffusion in the bulk of a crystal; one requires either interstitials or vacancies and the other is based on substitution. These processes occur over relatively long periods of time. In dislocation creep (or power law creep) the diffusion of atoms can 'unlock' dislocations via dislocation climb. The movement of freed dislocations under applied stress leads to dislocation creep.

Recrystallisation is a softening mechanism, which will occur during the rolling process at temperatures above $0.3T_m$ (Humphreys and Hatherly 1996). Recrystallisation forms new grains with low dislocation densities, which grow into existing grains from nucleation sites. This process is different from recovery, which acts to annihilate pairs of

dislocations and form subgrains. Due to the limited time in the rolls it is less likely that the recrystallisation will be dynamic and instead static recrystallisation between rolling stands will dominate, see Figure 2.3. The newly formed grains will have a lower energy state and fewer dislocations.

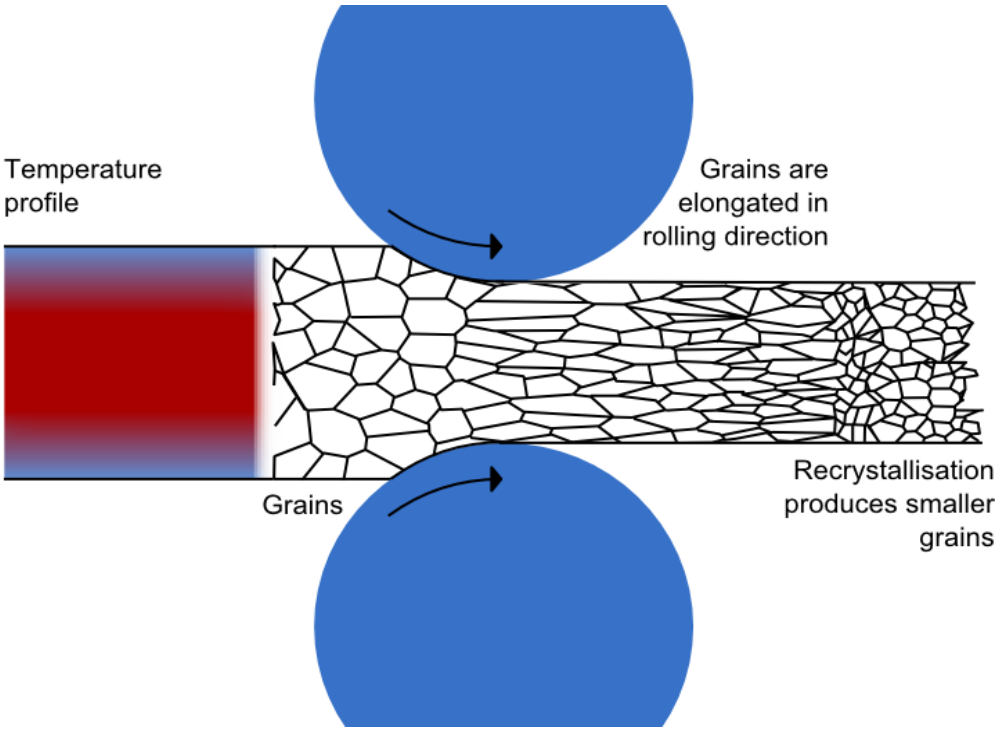

Figure 2.3. Static recrystallisation altering the size of grains.

The fully recrystallised specimen will have a more homogeneous grain size, which will no longer be elongated in the rolling direction, permitting the continued use of an isotropic material model. The grain size, d, will affect the yield stress, σ_Y, in accordance with the Hall-Petch relationship, given in Equation 2-1, where k_0 is a material constant and σ_0 is a material constant relating to the resistance of the lattice to dislocation motion. The change in grain size permits different damage mechanisms.

$$\sigma_Y = \sigma_0 + k_0 d^{-1/2} \qquad \textbf{Equation 2-1}$$

Nucleation sites for recrystallisation are areas of high Gibbs free energy. A dislocation can be thought of as an area of higher potential energy due to the forced

separation and attraction of surrounding atoms. When the temperature is high enough the material has enough energy to release the structure and a new stacking occurs, releasing the stored energy as heat. This substitution diffusion process acts to reduce the Gibbs free energy.

It is possible to measure the amount of recrystallisation that occurs. Cho et al. examined the grain boundaries using an innovative etching technique and observed the difference in grain size for a large number of rolling temperatures (Cho, Choi et al. 2008). Denissen et al. analysed the amount of recrystallisation by the amount of energy it took to initiate (Denissen, Liebe et al. 2006). However, it was pointed out using the JMAK model that two different enthalpic processes are present during recrystallisation: nucleation and growth. It was found by Denissen et al. that the activation energy for recrystallisation nucleation is larger than that of grain growth (Denissen, Liebe et al. 2006). The precision of measurement of the temperature change relative to the forming temperature makes this method problematic.

There are methods to inhibit and even stop recrystallisation. Revidriego et al. discussed the recrystallisation stop temperature (RST), which is the minimum temperature for recrystallisation to occur (Revidriego, Gutierrez et al. 1996). The RST was found to decrease with increasing interpass time. Additions, such as vanadium, can slow the recrystallisation process but do not stop it (Garcia-Mateo, Lopez et al. 1999), although neither of the papers explained the possible mechanisms. Additions could increase stability of the dislocations so less energy is immediately available for the process to start.

Temperature has been noted to be the most important aspect for recrystallisation (Kovac and Cizelj 2005), particularly in the centre of the billet (Duan and Sheppard 2002). However, roll-friction was claimed to be the most important at the surface of the material (Duan and Sheppard 2002). It was also claimed that the fraction of recrystallisation falls from the centre to the surface. This could effect surface damage and hence edge cracking. It has also been suggested that a certain critical amount of strain is required before recrystallisation will initiate (Petkovic, Luton et al. 1975). It was suggested that, if this strain is not reached, softening takes place by static recovery instead. However, Foster, who has generated a series of dislocation-based models, has

argued that a limiting factor for the initiation of recrystallisation is the dislocation density (Foster, Dean et al. 2007). The dislocation density increases with increasing strain, therefore both claims are not exclusive but heavily related. However, dislocation density is a better indication of stored energy.

The dislocation density also affects damage softening. An investigation of this was carried out by Liu (Liu, Farrugia et al. 2005). Using a high strain rate, of 10 s^{-1}, it is less likely that there will be any dynamic recrystallisation. However, by interrupting the test at high temperatures of 1100 °C, it is possible that static recrystallisation will occur. As the grain growth process is not instantaneous, the time of interruption, t_{rec}, has an effect on material response, as can be seen in Figure 2.4 (a) and (b). It is clear that the ductility can be improved by static recovery, which is likely to occur during the inter-stand time between rolls in the industrial process. However, after a certain interrupt time the improvement in ductility decreases, although it remains higher than without any interruption. Nevertheless, it has been reported that, in most strip rolling operations, the speeds are so fast that the interpass times are less than 1 second (Phaniraj, Behera et al. 2006). Therefore, it is likely that if static recrystallisation does occur, it will be incomplete. It has been found that a smaller austenite grain size decreases the incubation time for static recrystallisation (Medina, Chaves et al. 2007). However, it may not be possible to control this and encouraging static recrystallisation in the industrial process may not be possible.

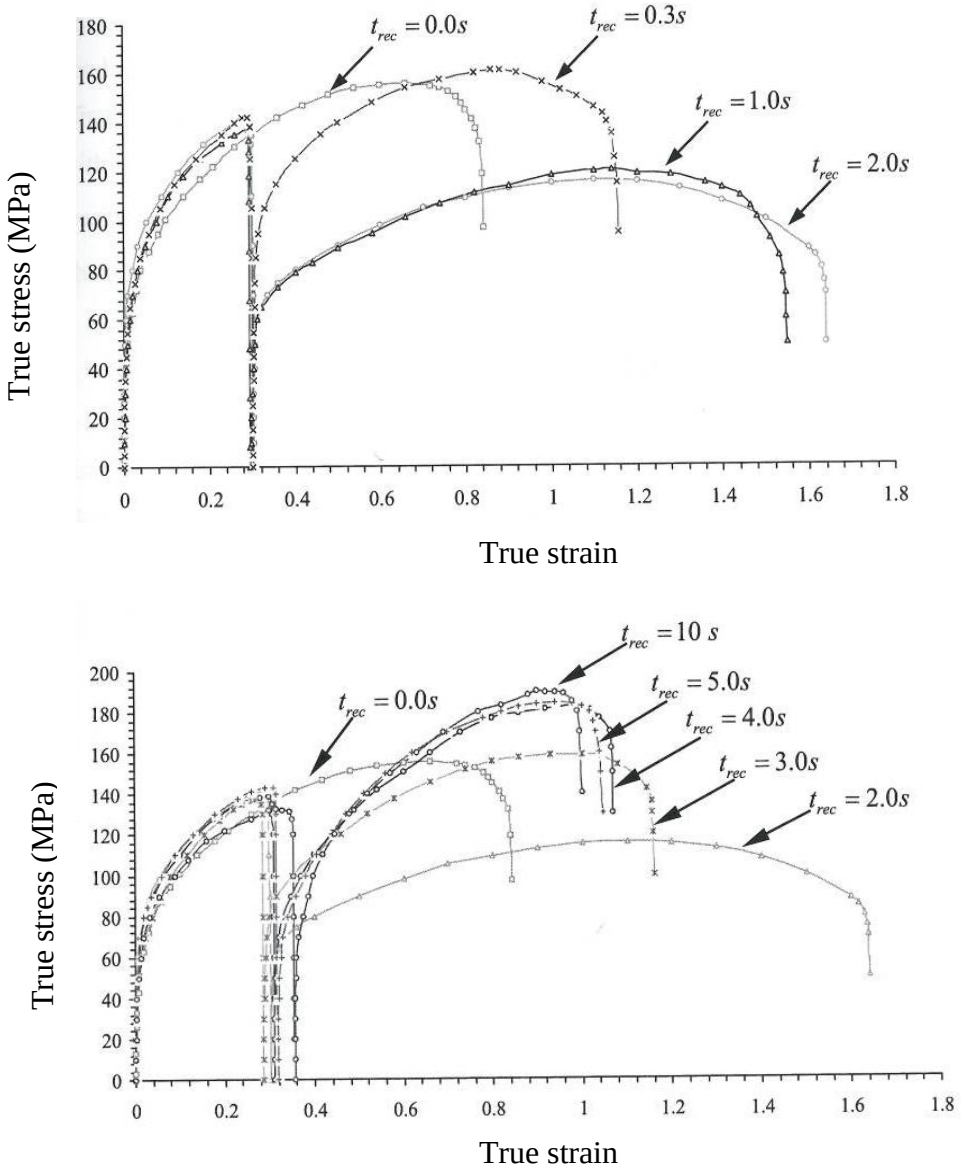

Figure 2.4. The effect of interrupt time, t_{rec}, on the true-stress true-strain curves during uniaxial tensile tests at $\dot{\varepsilon}$ = 10 s^{-1} and T = 1273 K. Each curve represents a different interrupt time a) Short interrupt times b) long interrupt times.

The importance of controlling recrystallisation was highlighted by Zhu and Subramanian who suggested that "Refinement of grain size is the most effective approach to obtain high toughness especially at low temperature with high strength level" (Zhu and Subramanian 2006). The paper describes controlling static and dynamic recrystallisation to eliminate mixed grain size, hence better control of material properties. The resulting

models are not accurately representing the physical tests. However, the trends are similar for the stress-strain graphs presented, and optimized rolling schedules were produced for homogenous ultra-fine grain sizes.

It has been suggested by Belov that there is a limit for damage after which it cannot be healed (Belov, Bogatov et al. 1985). It was also shown that cyclic heat treatment with phase recrystallisation will lead to more complete healing of the damage than recrystallisation annealing. Troiano even stated that the process of heating can be repeated to 'heal' fatigued parts but again some damage could not be healed for damage past certain limits (Troiano, Cote et al. 1997). Healing has been shown to be possible with high temperatures where it is thought that the expansion caused by heat creates compressive stresses (Zhou, Qin et al. 2000). Han has suggested that damage healing should be at the forefront of current research and has also investigated heating to induce healing (Han, Zhao et al. 2007). Bogatov described the heating as annealing leading the 'healing' processes (Bogatov 2003). Gomuc found that creep hold compression could be used to investigate healing. It may be possible that Gomuc has evidence of void collapse, followed by a diffusion process, which would entirely heal the void and restore the load-bearing section (Gomuc and Bui-Quoc 1986). It is likely that at high temperatures diffusion bonding between two '*clean*' surfaces is possible. However, any open surface cracks will permit oxidation and this will prevent diffusion bonding.

2.4 Damage mechanisms

Edge cracking is a well known form of damage leading to product rejection in hot rolling (Saxena 1997). Figure 2.5 shows edge cracking at different scales and the associated damage. However, macroscopic damage is not the sole consideration; a product must not experience accumulated damage at the micro-scale that may lead to fracture in service. Some manufacturing standards dictate that a product may fail to meet manufacturing specifications with a frequency no greater than 1 in 10^6 (Harry 1988). Therefore, the material processes contributing to damage need to be understood.

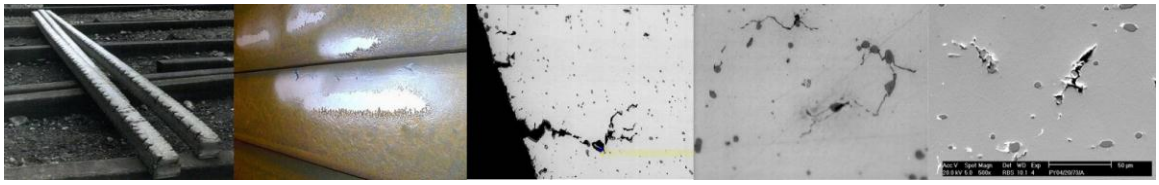

Figure 2.5. Edge cracking is due to damage at various scales.

Hot forming usually refers to processing at temperatures above two thirds of the melting temperature (Kalpakjian 1984). These temperatures allow the activation of several deformation mechanisms within the material. In the hot metal forming process examined here (rolling), the strain rates are typically up to 10 s^{-1} (Liu 2004). Damage at grain boundaries is observed at high temperatures, which is more likely to occur at relatively low strain rates, of 1 s^{-1} or less, as it is diffusion rate-limited (Hayhurst, Lin et al. 2008). Higher strain rates reduce grain boundary diffusion and sliding therefore dislocation-based, plasticity-induced damage around inclusions will dominate (Lin, Liu et al. 2005; Besson 2010). The following gives a broad overview of damage, and subsequently a review of the damage mechanisms that occur under conditions similar to hot rolling are presented.

2.4.1 Generic damage process

Damage may be characterised as the unwanted reduction in the stress-carrying capacity of a material section or the appearance of new surfaces in a material. The generic damage process includes a three-stage development: nucleation, growth and coalescence.

Nucleation: Incongruity at stress concentrations gives rise to initial creation of damage within the material. The probability of nucleation is thought to be dependent on the Gibbs free energy, which is described in order of lowest to highest free energy: homogeneous sites, vacancies, dislocations, stacking faults, grain boundary with inter-phase boundaries, free surfaces (Porter and Easterling 2001).

Growth: As material surrounding the damage site plastically deforms, the damage feature will enlarge. The macro flow stress is negatively offset at this stage due to reduced cross sectional area at the micro-scale.

Coalescence: At a critical level of damage, damage features converge or material between damage features becomes significantly weakened and cracks form between cavities. The coalesced cracks grow quickly to form macro-scale cracks.

2.4.2 Observing damage

Thomson et al. suggest that there are three reasons for edge cracking: limited ductility and uneven rolling i.e. a concave/convex profile and transverse variations in stresses, particularly by tight edges (Thomson and Burman 1980). Engineers at Tata steel, through empirical studies, suggest three other reasons for material damage: Billet quality, die scratching and maladjusted rolls. The first two factors relate to the lack of homogeneity in the processing and the latter is based on the changing stress distribution. These effects have to be predictable. To make predictions, an understanding of the underlying mechanisms is required. Plasticity-induced and grain boundary damage can co-exist in a proportion that depends on the temperature, strain rate, microstructure and chemical composition in a particular process (Reed 2006; Dunne, Wilkinson et al. 2007). The dependence of the rate of damage accumulation on the strain rate and temperature are critical information required for an appropriate damage model. The stress state, on the other hand, determines whether damage will propagate (Gao, Zhang et al. 2010).

Porosity can be present in cast metals. There is a difficulty in differentiating porosity from other microstructural defects, such as inclusions, making detection challenging (Gawdzinska, Grabian et al. 2003). Porosity can form in cast metals due to unsaturated gas, gas emission during coagulation and during contraction of the matrix. These defects get passed on to the rolling process. It has been shown that defects such as cracks, as well as central and peripheral segregation, have been found in as cast and hence rolled material (Mamuzic, Longauerova et al. 2005). Eddy Current surface defect detection and hybrid Laser-EMAT (ElectroMagnetic Acoustic Transducer) are used on industrial products due to the high sampling speeds. However, the typical spatial resolution is 1 mm, according to the patent (Moroli and Piancaldini). Therefore, the resolution is too low for the microscopic analyses required in this research.

Damage affects the material response. It is possible to measure the changes in the material response due to damage through interrupted testing. The Young's modulus, *E*, can be evaluated for damage using Equation 2-2, where $\tilde{E}$ is the Young's modulus after some amount of plastic deformation, measured during the removal of the applied load and *D* is the damage fraction.

$$D = 1 - \tilde{E}/E \qquad \text{Equation 2-2}$$

An example of the effect of damage on Young's modulus is shown for a pure copper sample deformed at room temperature in Figure 2.6. Various precautions to ensure the accuracy of the measurement of the Young's modulus must be made. Nevertheless, the damage can only be evaluated with a precision of +/-5% (Lemaitre and Chaboche 1990). As discussed previously, interrupting the test permits static annealing processes meaning that the measurement of material response more than once in a test sample would give erroneous results for the latter measurements, unless the complex annealing processes are adequately included. A final reason that this method may not be used is due to the viscoplastic response of the material at high temperatures, making the initial measurement of *E* in the virgin material challenging.

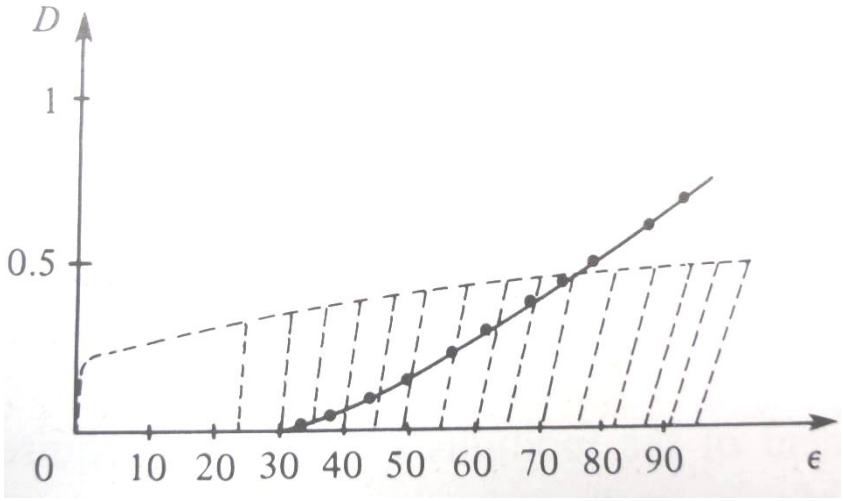

Figure 2.6. Interrupted test showing the evolution of Young's modulus, *E*, with plastic strain, *ε*, in pure copper (Lemaitre and Chaboche 1990).

Microscopic damage sites can be observed using optical methods. The void volume fraction can be measured by quantitative metallography and also precision density measurements (San Marchi 2002). Damage mechanisms can be established by examining micrographs of sections of deformed material and fracture surfaces (Besson 2010). Recent efforts have been made in evaluating the amount of void growth (Ghadbeigi, Pinna et al. 2010). The ease of preparation of samples means that optical methods are very useful in evaluating damage.

Sectioning and polishing has the disadvantage of being destructive, as the deformed sample must be cut. The polishing process is also known to fill the smaller voids and this makes it difficult to accurately quantify the damage volume fraction (Babout, Maire et al. 2001). In-situ tensile tests of a polished sample using a scanning electron microscope (SEM) avoids this but the surface stress state does not represent the internal stress state.

A method measuring the density of mild steel hollow cylinders during torsion tests is described in (Rosochowski and Olejnik 1988). The minute changes in density increased exponentially with strain and were considered to be due to void growth. However, it is likely that the material did not remain in purely torsional stress state, as deformation progressed and the material rotated on itself a more tensile stress state would be encouraged. This method is useful but not practical in high temperature tests due to the loss of material due to scale build up.

High-resolution synchrotron X-ray tomography can allow visualisation and quantification of the damage throughout the microstructure in three dimensions (Phillion, Hamilton et al. 2011). There have been several authors who have taken measurements of the damage in various metals with a second phase (Toda, Sinclair et al. 2004; Maire, Bouaziz et al. 2008; Weck, Wilkinson et al. 2008). Typically they took in-situ measurements from uniaxial tensile tests, interrupting the deformation whilst capturing the images. This allows tracking of the progression of individual damage sites. However, until the rate of capture increases, during high-temperature tests this pause will allow the material to recrystallise, which greatly affects damage propagation due to the annihilation of dislocations (Humphreys and Hatherly 1996; Liu 2004).

When the damage is analysed for use in quantification, statistical methods are used for the entire sample and examining individual damage sites is redundant. Therefore, running the tests ex-situ and quenching to freeze the microstructure gives a better representation of damage propagation during straining and retains the necessary information to quantify damage. An additional benefit of ex-situ tomography is that the resolution can be higher than the in-situ tests, as the signal-to-noise ratio and resolution are proportional to the time available, which is significantly less during in-situ testing due to the static changes that occur at high temperatures.

2.4.3 Creep-type damage

Multiplication of mobile dislocations occurs as metal creep proceeds (Dyson 1988) and is termed mobile dislocation strain softening (Othman, Lin et al. 1993). This mechanism relies on the supposition that creep is controlled by kinetics of mobile dislocation multiplication, not dislocation recovery. This mechanism causes softening of materials, which increases creep rates but it does not determine failure (Dyson 1988).

Creep-type damage is based on diffusion processes and is therefore time and temperature dependent, and the rate of deformation has a significant effect on the mechanism by which creep occurs. Globular cavities, which occur at lower stress levels than peak stress, lead to grain cracks (Dyson and McLean 1983). Many low-ductility metals can fracture by the mechanism of creep constrained grain boundary cavity nucleation and growth. The rate of the cavity nucleation and growth rates influences deformation resistance and fracture mode (Liu, Farrugia et al. 2006).

The mechanism of continuum cavity growth is similar to creep-constrained grain boundary cavity nucleation and growth, but occurs at higher stress levels. The voids are again at grain boundaries but are more often oval-shaped due to the higher strain rate. However, if the diffusion is rapid the void remains spherical. Voids grow by a combination of plastic flow and diffusion of atoms away from the void and onto grain boundaries. A void can also grow by power law creep of the surrounding matrix. Continuum cavity growth is the predominant mechanism when damage is large (Hayhurst, Lin et al. 2008).

In some cases the microstructure also alters the supportable mechanisms. Superplastic void growth only occurs with a fine grain size of less than 10μm, temperatures above $0.7T_m$ and strain rates of $0.01s^{-1}$ to $0.1s^{-1}$ (Perevezentsev, Rybin et al. 1992; Lin and Dunne 2001). The dominant deformation mechanisms are grain rotation and grain boundary sliding (Kim 1999). Balluffi suggested that grain boundary diffusion, which is required for accommodation of grain rotation and grain boundary sliding, is 10^6 times greater than bulk diffusion under similar conditions (Balluffi, Allen et al. 2005). Vetrano et al. have reported that if the accommodation by distribution of matter within the mantle adjacent to grain boundaries fails to meet imposed requirements by deformation rate, stresses at grain boundaries are not relaxed sufficiently and subsequently cavities nucleate (Vetrano, Simonen et al. 1999). Three distinct mechanisms of superplastic void growth have been observed (Han, Zhao et al. 2007).

1. Stress-directed vacancy, or conventional diffusion, which usually dominates initially (Pardoen, Dumont et al. 2003). Vacancies from neighbouring grain boundaries are directed into a void, and hence it grows. The growth rate decreases with increasing cavity radius. An equation for the void volume fraction, *V*, can be given in terms of the equivalent plastic strain as:

$$V \propto \varepsilon \qquad \textbf{Equation 2-3}$$

2. Superplastic diffusion is significant when the void diameter is greater than the average grain size and less than 10 μm, and the strain rate is less than 1×10^{-4} s^{-1} (Lin and Dunne 2001). Cavities absorb vacancies similar to conventional diffusion but they are found along more than one grain boundary.

$$V \propto \varepsilon^{1/3} \qquad \textbf{Equation 2-4}$$

3. When the strain rate is greater than $1\times10^{-4}\,s^{-1}$, plastic deformation supersedes the other mechanisms (Chokshi 1987; Duprez 2002). This is thought to be the most important mechanism for overall void growth. The translation of neighbouring grains tends to enlarge grain boundary cavities.

$$V \propto \varepsilon^{1/n} \quad (n>1)$$ **Equation 2-5**

The creep-type damage mechanisms occur at the lowest strain rates studied in this project. However, it is more likely that higher strain rates will permit dislocation motion to occur instead of diffusive processes, and plasticity-induced damage will dominate.

2.4.4 Plasticity-induced damage

In cold metal forming processes, there is no grain boundary sliding and multiplication of dislocations is the dominant deformation mechanism, causing voids to nucleate around second-phase particles within grains (Brust and Leis 1992). Second-phase particles are also known as inclusions, and the terms will be used interchangeably. Inclusions are random distributions of a continuous material inside another continuous material, forming a composite. During the casting process, whilst the material solidifies, manganese (added to getter sulphur) combines with sulphur and precipitates forming inclusions. The steels tested in this project, provided by Tata Long Product Rolling Department, contains manganese sulphide (MnS) inclusions, which aid chip formation but are known to have a detrimental effect on the ductility (Moody, Garrison et al. 1993; Horstemeyer and Gokhale 1999).

Inclusions can be seen in the microstructure of a free cutting steel studied, in Figure 2.7. There is a distribution in the size of inclusions between 1 and 50 μm. This permits a range of different effects that inclusions can have on the material response. However, it has been reported that these inclusions only affect the ductility and not hardening characteristics for a given volume fraction and different sizes and spacing of inclusions (Foster, Lin et al. 2006; Bouchard, Bourgeon et al. 2008). This agrees with Thomason who found that inclusions of 0.01 μm would interact with dislocations, and hence affect hardening, but inclusions greater than 1 μm would not and should be modelled using continuum methods (Thomason 1990).

Figure 2.7. Micrograph of MnS inclusions in steel matrix of a free cutting steel studied in this thesis.

The inclusions are known to promote damage by acting as nucleation sites and further to this act as stress raisers to promote damage growth (Luo 2001). Nucleation can be strain- or stress-based (Thomason 1990). Stress-based nucleation will be affected by the distribution of inclusions (Garrison and Wojcieszynski 2007). Free cutting steels (FCS) have small additions of heavy metals to improve their machinability. It has been shown that the additions precipitate at the boundary between the MnS inclusions and the matrix. At the high temperatures typical of hot forming FCS, 850-1100^{o}C, the additions melt leaving negligible bond strength and the inclusions debond from the matrix immediately during straining (Foster, Dean et al. 2007). An example of a leaded FCS, or LFCS, which is studied in this thesis is shown in a scanning electron microscope image, Figure 2.8. The figure highlights the inclusion and the lead addition at the inclusion-to-matrix interface. The inclusions play an integral role in the rate of damage accumulation in the material.

a) b)

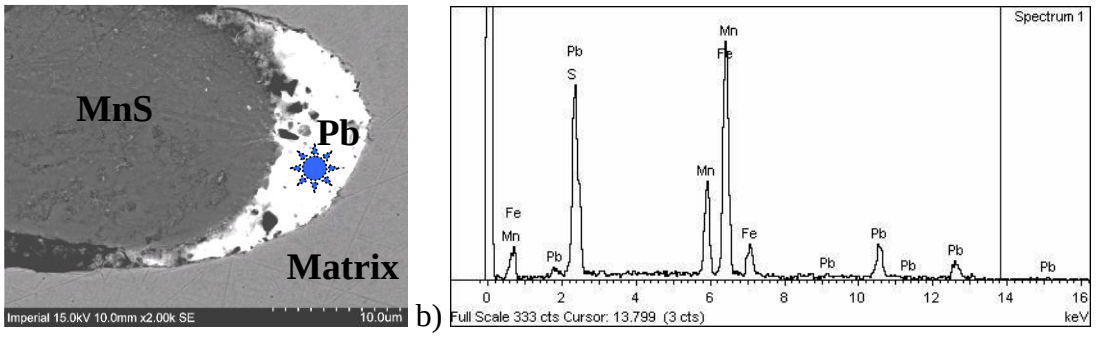

Figure 2.8. a) SEM of polished Free Cutting Steel surface showing MnS inclusion and lead at boundary b) EDX showing lead (at highlighted circle).

MnS inclusions are relatively soft compared to other second-phase particles, which means that their shape can evolve during the rolling process. This leads to anisotropy in the material (Hosseini, Temmel et al. 2007). The orientation of the deformed inclusions relative to the applied stress affects the ductility (Bouchard, Bourgeon et al. 2008). Though this aspect of material response is important it is not investigated in this research as the significance of the effect is outweighed by the complexity of anisotropic damage.

The distribution of inclusions will have the greatest effect if the stress discontinuities caused by inclusions interact. This was highlighted by Argon who developed separate models for whether inclusions interacted or not (Argon, Im et al. 1975). Various ratios based on measurements from the microstructure exist (Thomason 1990; Hammi and Horstemeyer 2007). However, to summarise, they demonstrate that the strain to failure is proportional to the reciprocal of the volume fraction of inclusions (Garrison and Wojcieszynski 2007). The volume fraction has been shown to relate to the radius and spacing of inclusions by Ashby in Equation 2-6 (Shercliff and Ashby 1990). The volume fraction is calculable from the chemical composition but it does not truly reflect the effect that the inclusions have on the microstructure as the radius for a given volume fraction will alter the possible material mechanisms.

$$f = \frac{2\pi}{3}\left(\frac{r}{l}\right)^2$$ **Equation 2-6**

There have been attempts to model the effect of inclusion distributions, both including and excluding their interactions. A common method for modelling non-interacting inclusions uses periodic boundary conditions (Luo 2001). This method has also been used for interacting inclusions (Böhm, Eckschlager et al. 2002). The homogeneous nature presented by this technique does not fully accommodate the stress localisation observed due to clustering of inclusions. Using the distributions directly from micrographs it was possible to highlight the stress localisation created by clustering of inclusions through a finite element model (Foster, Lin et al. 2006). The model, assuming

plane stress, used one fixed edge and applied a constant positive strain rate by displacing the opposite edge. Typical results of the modelled clustering are shown in Figure 2.9, where bands of stress can be seen perpendicular to the applied stress between the closest inclusions.

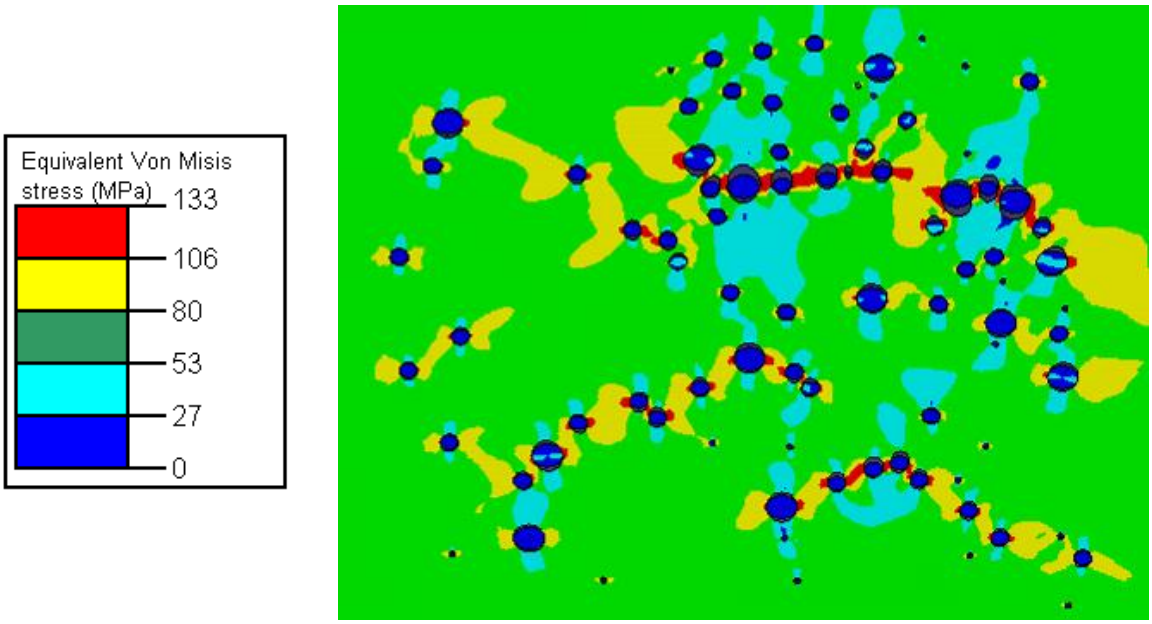

Figure 2.9. Simulation of cluster of inclusions showing stress localisation (adapted from (Foster, Lin et al. 2006)).

In summary; the voids are nucleated in a plastically deforming matrix by cracking or debonding between matrix and second-phase particles or inclusions. This causes localised stress and strain at the void surface, which does not bear any load (Tvergaard and Needleman 2001). This continues and amplifies the distortion; the microcavities or microvoids grow with increasing tensile strains to macroscopic failure (Staub and Boyer 1996).

2.5 Inhibiting damage

Bridgman investigated large plastic flow and fracture with special emphasis on the effects of hydrostatic pressure (Bridgman 1953). By investigating more than 20 types of steel Bridgman found that increased ductility was possible with increased hydrostatic

pressure. Bridgman also found that any tensile stress less than the applied hydrostatic stress would not cause fracture. This was explained by stating that fracture is an energy releasing mechanism. If the material cannot release the stored energy due to the hydrostatic pressure it will not fracture. Bridgman also examined the collapse of spherical and cylindrical cavities under hydrostatic stress and found that no permanent change in external dimension could be detected after the release of the hydrostatic pressure.

Moreover, French and Weinrich looked at the effect of hydrostatic stress in the fracture of brass, copper and aluminium (French 1975; Weinrich and French 1976). Weinrich found that the strain to fracture increased with increasing externally applied hydrostatic stress. Under examination with an SEM they found that nucleation, growth and coalescence of damage decreased with increasing hydrostatic stress. Similar results were found by several authors (Kao 1990; Lewandowski 1991; Margevicius 1991).

Controlling the grain size can influence damage. It has been noted that large grains permit less grain boundary sliding and grain rotations under hot conditions, which leads to lower grain boundary damage (Lin, Liu et al. 2005). However, a larger grain size will have higher dislocation movement and hence plasticity-induced damaged increases. When grains are very small (<10μm) grains rotate and slide past each other with greater ease, hence damage accumulation is low (Lin and Dunne 2001). When grains are of medium size the damage is maximized. After recrystallisation occurs, the nucleated grains grow. If the recrystallisation is modelled appropriately, it is possible to avoid deforming the material when the grains are in the size region leading maximum damage.

Upsetting tests have shown that fracture is less likely when there is zero friction between the die and the test-piece (Thomason 1990). When the upsetting tests are performed with friction, barrelling occurs. The largest diameter of the barrelled cylinder, the equatorial line, develops furthest from the effect of friction and tensile hoop stress builds up. This localised tensile stress propagates damage.

Trattnig et al. looked at pre-damage in nickel alloys by deforming specimens under torsion, then applying tensile loads to the specimens until failure and comparing to specimens without the prior torsion (Trattnig, Kleber et al. 2008). This revealed that the test-pieces with prior deformation under torsion fractured at lower strains and therefore had a pre-damaged structure. Since the torsion could not initiate void growth, it must

have allowed damage nucleation meaning that more energy was available for void growth when tension was applied. It is not possible to see nucleated damage under an SEM. However, the paper shows that it is possible to quantify the amount of nucleated damage via comparisons. It would be useful to apply torsion followed by compression and then compare these specimens to those that have not been deformed. This would allow investigation into damage nucleation.

Bao and Wierzbicki found a cut-off point for the average stress triaxiality ratio at minus one-third, beneath which fracture would not occur, see Figure 2.10 (Bao and Wierzbicki 2005). It is important to note that the paper examined the average triaxiality across the area of deformation and did not take into account localised tensile stresses. Locations of areas of localised tensile stresses have a significant effect on damage accumulation.

Bao and Wierzbicki suggested that, at negative stress triaxialities, the fracture is no longer related to void growth but instead relates to shear-based highly localised fracture (Bao and Wierzbicki 2005). The related paper by Mirone argues that in compressive stress states it is possible for voids to be moved closer together to the point that they coalesce, and this allows microcracking (Mirone 2007). Bao and Wierzbicki also state that they are not certain what occurs at the transition between shear and void fracture; they suggest that the transition is at a triaxiality ratio of about 1/3 but it depends on the material. They looked at the transition in a tensile specimen, which has been shown to have variable triaxiality ratio (Mirone 2007).

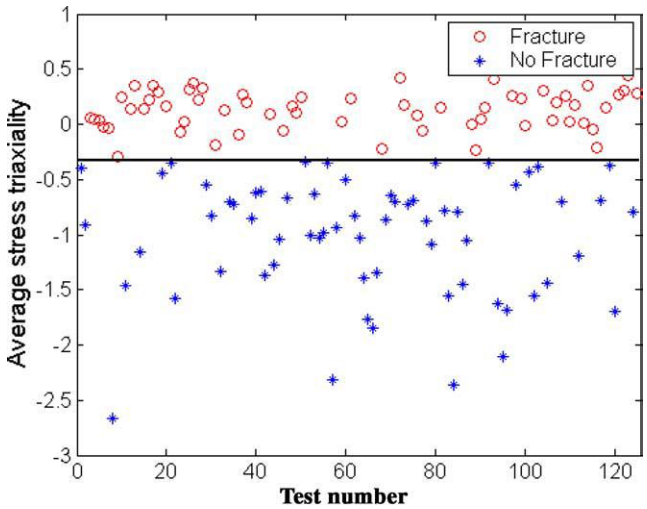

Figure 2.10. Average stress triaxiality in tensile tests and relation to fracture (Bao and Wierzbicki 2005).

Mirone looked at the effect of triaxiality on the rupture of tensile specimens using the Boa and Wierzbicki model to predict the location of where failure occurs (Mirone 2007). It was found that the triaxiality changes significantly over the necking test-piece, see Figure 2.11. However, the models successfully predicted the location of failure initiation, proven by micrograph examination of the fracture points on the test-pieces.

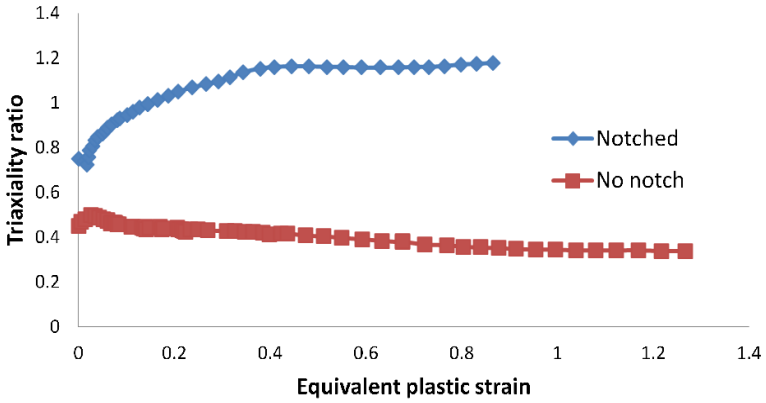

Figure 2.11. History of triaxiality ratio vs. equivalent plastic strain, for Cu 99.97% unnotched and AISI T304 R2 notched specimens (Mirone 2007).

2.6 Conclusions

The processing route for the hot rolling of free cutting steels has been evaluated and the ranges of strain rate, temperature and stress levels were highlighted. This led to a review of the salient material mechanisms expected in the hot rolling process. Several researchers have investigated ductility exhaustion in different crystalline materials under a range of conditions, revealing a variety of damage mechanisms. This information can be used to develop an understanding of the factors affecting the damage mechanisms. This has been achieved by several authors who have developed models of these processes; the following chapter gives a review of applicable models.

Chapter 3 Modelling damage

3.1 Introduction

The following is a preface to some of the prevalent ductile damage models, their origins and developments. The derivations of the models are not included in most cases, but an explanation of the assumptions is given, as it relates to how applicable the models are for hot rolling of free cutting steels.

Two of the foremost methods that have been used to establish constitutive equations and capture the stress state are based on micromechanical response and, the more phenomenological, continuum damage mechanics (CDM). One of the earliest examples of the former was by Gurson, where voids in a porous matrix were considered (Gurson 1977). CDM was introduced by Kachanov; the main aspect of this method is that a damaged relative-volume-element can be equated to an effective undamaged volume (Kachanov 1958). It uses state variables to account for damage and is versatile enough to be used for a range of problems including creep and ductile plastic damage (Leckie and Hayhurst 1977; Spindler 2004; J. Cao 2008). Attempts have been made in both methods to account for the stress state. The stress triaxiality, which is the mean stress divided by the von Mises, or equivalent stress, σ_m/σ_{eq}, is an appropriate parameter for monitoring damage in a three-dimensional stress state, such as that in hot rolling. Several damage equations that use the stress triaxiality will now be reviewed in chronological order.

3.2 Damage at grain boundaries

3.2.1 Gurson-Tvergaard-Needleman

Reliable damage models can have a series of material and process-specific constants that are found through physical testing of a material under suitable conditions. An example of such a model is the Gurson model, which generates a yield function to accommodate the effect of void growth on softening (Gurson 1977). The model is based on spherical voids dilating inside an incompressible matrix. An important aspect of the Gurson model is that it accounts for pre-damaged material. It requires two material

constants in order to be implemented. The original Gurson model was further developed by Tvergaard and Needleman to include coalescence (Viggo 1985; Tvergaard and Needleman 2001). Size is disregarded in the Gurson model. However, there is evidence that there is size dependence of voids (Traiviratana, Bringa et al. 2008).

The rate of increase of void volume fraction is based on the rate of void nucleation and growth, according to Equation 3-1.

$$\dot{f} = \dot{f}_n + \dot{f}_g \qquad \textbf{Equation 3-1}$$

It has been suggested that a nucleation term is not required as all voids are nucleated at the beginning of plastic deformation so can be accounted for using an initial volume fraction, f_0 (Lenard, Pietrzyk et al. 1999). However, there have been several suggestions for nucleation terms (Tvergaard 1990). Gurson also suggested a nucleation term based on equivalent plastic strain, ε_{eq}^{p}, and volume fraction of inclusions, f_e, as shown in Equation 3-2:

$$\dot{f}_n = f_e \cdot \varepsilon_{eq}^{p} \cdot \dot{\varepsilon}_{eq}^{p} \qquad \textbf{Equation 3-2}$$

However, the voids that are already nucleated will grow purely due to plastic deformation (Gurson 1977). The rate of increase in void fraction is given by Equation 3-3, where $\boldsymbol{I}$ is the 2nd order unit tensor. $\boldsymbol{I}$ is required as the equivalent plastic strain rate is a tensor and the void growth rate is a scalar.

$$\dot{f}_g = (1-f)\dot{\varepsilon}_{eq}^{p} : I \qquad \textbf{Equation 3-3}$$

The model was updated by Tvergaard to account for different-shaped voids using terms q_1 and q_2. These parameters have been further updated by several authors and values of q_1 =1.25 to 1.5 and q_2=1.0 were found to improve the performance of the yield

condition by 50% (Tvergaard 1981; Koplik and Needleman 1988; Tvergaard 1990). The updated model takes the form given in Equation 3-4.

$$\Phi = \left(\frac{\sigma_m}{\sigma_{eq}}\right)^2 + 2q_1 f \cosh\left(\frac{3q_2\sigma_m}{2\sigma_y}\right) - \left[1 + \left(q_2 f\right)^2\right] = 0 \qquad \textbf{Equation 3-4}$$

Coalescence has been implemented by updating the void volume fraction using a different method after a certain critical value is met (Tvergaard and Needleman 2001). It could be argued that the physical basis for this is the ligament length of the inter-void matrix (Hammi and Horstemeyer 2007). The new calculation for the void volume fraction is used when a critical value, f_c, is met; see Equation 3-5, where $f_u^* = 1/q_1$. The volume fraction can then increase until it reaches the value associated with final fracture, f_f.

$$f^*(f) = \begin{cases} f & f \le f_c \\ f_c - \dfrac{f_u^* - f_c}{f_f - f_c}\left(f - f_c\right) & f > f \end{cases} \qquad \textbf{Equation 3-5}$$

These combinations and updates have made what is known as the Gurson-Tvergaard-Needleman (GTN) model. This model is often used as it is simple to implement. However, the accuracy of the model is subject to debate (Thomason 1990). For example, one key aspect that the model lacks is the interaction of voids.

3.2.2 Lemaitre

Lemaitre's work built upon the original work of Kachanov, which used the equivalent stress (Kachanov 1958). The model is based on a continuum and therefore individual cracks and voids are not considered. A porous volume can be sectioned normal to an applied stress, creating a plane of area *S*. The cross-section will have an area of voids S_D, therefore damage can be defined as $D = S_D/S$. Since $0 \le S_D \le S$, it can be stated that $0 \le D \le 1$. A volume of porous material can be made equivalent to a 'clean'

volume with a smaller cross-sectional area and the equivalent stress can be used, see Equation 3-6.

$$\tilde{\sigma} = \frac{\sigma}{(1-D)} \qquad \textbf{Equation 3-6}$$

D is a scalar variable representing the damage fraction. When *D* is zero, the material is in a totally undamaged state, and when *D* is one, the material has no load-carrying capacity. This assumption was used by Lemaitre in forming the following model for isotropic damage and hardening. If the stress is higher than a particular value, there is damage, which is characterised by a yield surface. The final assumption is that damage is affected by deviatoric, as well as hydrostatic stresses. Using the elastic energy release rate criterion, w_e, coupled with linear elasticity, damage and effective stress, it is possible to derive an equation for yield, Equation 3-7.

$$w_e = \frac{1}{2E(1-D)}\left(\frac{2}{3}(1+\nu)\sigma_{eq}^2 + 3(1-2\nu)\sigma_m^2\right) \qquad \textbf{Equation 3-7}$$

It is possible to equate a simplified damaged stress state to the multiaxial stress state by stating that the energy in a particular stress state is equivalent to that in a uniaxial stress state. The form of the equation seen in Equation 3-8 is the most common form of Lemaitre's model. By relating the equation to the von Mises yield criterion, as shown in Equation 3-9, it is possible to create an equation that relates directly to damage. This form is shown in Equation 3-10, where *K* is the drag stress, *E* is the Young's modulus, S_o and s_o are temperature-dependent material constants, and *n* is the hardening exponent.

$$\sigma^* = \sigma_{eq}\left[\frac{2}{3}(1+\nu) + 3(1-2\nu)\left(\frac{\sigma_m}{\sigma_{eq}}\right)^2\right]^{1/2} \qquad \textbf{Equation 3-8}$$

$$-Y = \frac{\sigma^{*2}}{2E} = \frac{\sigma_{eq}^2}{2E(1-D)^2}\left[\frac{2}{3}(1+\nu) + 3(1-2\nu)\left(\frac{\sigma_m}{\sigma_{eq}}\right)^2\right]^{1/2} \qquad \textbf{Equation 3-9}$$

$$\dot{D} = \left[\frac{K^2}{2ES_0} \left(\frac{2}{3}(1+\nu) + 3(1-2\nu)\left(\frac{\sigma_m}{\sigma_{eq}} \right) \right) \left(\varepsilon_{eq}^{p} \right)^{2/n} \right]^{s_0} \dot{\varepsilon}_{eq}^{p} \qquad \textbf{Equation 3-10}$$

3.3 Plastic damage

3.3.1 Rice and Tracey

An early damage model by Rice and Tracey was based on the rate of change of volume of spherical voids in high triaxiality (Rice and Tracey 1969). Equation 3-11 is based on a concept of a void in a cylinder undergoing dilatational growth due to tensile stress triaxiality. Coalescence occurs once the voids grow to the point that they intercept. Boyer et al., amongst others, extended the model for non-spherical voids (Thomason 1990; Boyer, Vidal-Sallé et al. 2002). The void growth models can be implemented into a yield function to model the shrinkage of yield surface of materials in plastic deformation.

Bacha et al. extended the Rice and Tracey model to argue that 'voids nucleated by decohesion or cracking of second-phase particles' is common (Bacha and Daniel 2008). Bacha et al. considered a material containing a periodic array of rectangular voids, which deforms homogenously under small loads (Thomason 1990; Bacha, Daniel et al. 2008). Bacha et al. produced a model of void coalescence for low triaxialities.

$$\frac{\varepsilon_f}{\varepsilon_f^{uni}} = \frac{0.521}{\sinh\left(\frac{3}{2} \frac{\sigma_m}{\sigma_{eq}} \right)} \qquad \textbf{Equation 3-11}$$

3.3.2 Brozzo

This model was originally developed by Cockcroft and Latham, and involved the integration of the maximum principle stress with the equivalent plastic strain (Cockcroft and Latham 1968). Several damage models that were based solely on the equivalent stress are reviewed by Clift et al. and are found to be a useful tool for evaluating damage (Clift, Hartley et al. 1990). The addition of the equivalent stress by Oh permitted the evaluation of more complex stress states, as shown in Equation 3-12.

$$D = \int_0^{\varepsilon_f} \frac{\sigma_I}{\sigma_{eq}} d\varepsilon$$ **Equation 3-12**

Brozzo also developed the Cockcroft and Latham model and explicitly included the mean stress, as it had been found to decrease the growth of voids and permitted analysis of multiaxial states of stress on creep-constrained cavity growth (Brozzo, Deluca et al. 1972). A similar approach was used by Leroy, where the difference in principal and hydrostatic stress was taken (Leroy 1981). The model by Brozzo is shown in Equation 3-13, where σ_I is the maximum principle stress.

$$D = \int_0^{\varepsilon_f} \frac{2\sigma_I}{3\left(\sigma_I - \sigma_m\right)} d\varepsilon$$ **Equation 3-13**

3.3.3 Argon

A set of equations for the nucleation of damage were proposed that specifically includes particle distribution (Argon, Im et al. 1975). Once the stress at the inclusion to matrix interface, σ_{rr}, is equal to a critical stress, σ_c, then decohesion will occur. The nucleation terms are for both interacting inclusions, Equation 3-14, and non-interacting inclusions, Equation 3-15, where, k_0 is the yield stress in shear, γ is the shear strain, γ_y shear strain in yield, m is the Taylor factor, λ is the inclusion spacing and r is the inclusion radius.

$$\sigma_{rr} = k_0 \left[\left(\frac{\gamma}{\gamma_y} \right)^{1/n} + \sqrt{3} \left(\frac{\sqrt{6}\left(n+1\right)}{m} \frac{\gamma}{\gamma_y} \right)^{\frac{1}{n+1}} \right]$$ **Equation 3-14**

$$\sigma_{rr} = k_0 \left[\left(\frac{\gamma}{\gamma_y} \right)^{1/n} + \sqrt{3} \left(\frac{\sqrt{3}}{\frac{\lambda}{\rho}} \frac{\gamma}{\gamma_y} \right)^{\frac{1}{n}} + \frac{\sqrt{6}}{m} \frac{\lambda}{r} \right]$$ **Equation 3-15**

Therefore ductility is lower for larger inclusions by a factor of 1/*n*. Experiments have shown that σ_c is equal to 990 to 1920 MPa for many steels. An equation that is also based on a critical stress at the inclusion-to-matrix boundary is shown in Equation 3-16, where σ_{IC} is the plastic limit load stress and $\dot{\varepsilon}_{IC}$ is the maximum principle strain rate at the intervoid matrix neck (Thomason 1990). It was also shown that, for cylindrical voids, the plastic limit load can be related to the volume fraction of inclusions using Equation 3-17, where $k = \sigma_1 - \sigma_m$.

$$\left(\sigma_{IC} - \sigma_1\right)\dot{\varepsilon}_{IC} = 0 \qquad \textbf{Equation 3-16}$$

$$\frac{\sigma_{IC}}{2k} = 1.43 f^{-1/6} - 0.91 \qquad \textbf{Equation 3-17}$$

3.4 Other damage characterisations

3.4.1 Horstemeyer and Gokhale

Fracture toughness can be influenced by the initial volume fraction of inclusions as Gangalee and Gurland observed for aluminium alloys, Hahn et al. observed for several steel and aluminium alloys and Moody et al. observed for powder-processed titanium alloys (Gangalee and Gurland 1967; Hahn, Kanninen et al. 1972; Moody, Garrison et al. 1993). Hence, the initial volume fraction of inclusions is included in the nucleation rate, $\dot{D}_{nuc}$, from Gangalee and Gurland as seen in Equation 3-18 (Horstemeyer and Gokhale 1999), where *d* is a length-scale parameter, which can be the average radius of an inclusion. J_1, J_2 *and* J_3 are the Jacobian stress transformations, *f*, is the volume fraction of inclusions and *a*, *b* and *c* are material constants. K_{1C} is the stress intensity factor, given by Equation 3-19, where σ_y is the yield stress r_p is the plastic zone size and $\lambda(w)$ is a function based on the geometry of a specimen (Irwin 1958). The fracture probability of the particles increases with increasing particle size and decreasing silicon content. Gangalee and Gurland looked at the fracture of silicon precipitates in an aluminium matrix, which are more brittle than MnS inclusions.

It was postulated that more than one void could nucleate at a particle, but this is unlikely and has not been seen in SEM work so far. Nevertheless, this would imply that the greater the size of the inclusions, the greater the number of nucleation sites.

$$\dot{D}_{nuc} = \frac{|\dot{\varepsilon}| d^{1/2}}{K_{1C} f^{1/3}} D_{nuc} \left\{ a\left[\frac{4}{27} - \frac{J_3^2}{J_2^3}\right] + b\frac{J_3}{J_2^{3/2}} + c\left|\frac{I_1}{\sqrt{J_2}}\right| \right\} \qquad \textbf{Equation 3-18}$$

$$K_{1C} = \sigma_y \sqrt{2 r_p}\, \lambda(w) \qquad \textbf{Equation 3-19}$$

3.4.2 Liu

This model allows prediction of two damage mechanisms: Grain boundary type and plasticity-induced damage. This allows the model to be further justified by examining the microstructure where the proposed dominant damage mechanism is clearly evident. However, the equations in the model were built on the hypothesis that high strain rates (10 s^{-1}) encourage plasticity-induced damage, D_P, and low strain rates (0.01 s^{-1}) promote grain boundary damage, D_{GB}, see Equation 3-20 and Equation 3-21 respectively, where η is a factor representing grain size and a_x and n_x are material constants. Therefore it is not too surprising that it correctly predicts the trends in the dominant damage mechanism. Nevertheless, there is an increasing error in the model at lower strain rates. There is also the hindrance of the plethora of material constants that are required.

$$\dot{D}_{GB} = \eta \cdot \left(\left[a_4 \left(1 - D_{GB}\right) \cdot \dot{\bar{\rho}} \right] + \left[\left(\frac{1}{\left(1 - D_{GB}\right)^{n_2}} - \left(1 - D_{GB}\right) \right) \right] \cdot \left| \dot{\varepsilon}_p \right| \right) \qquad \textbf{Equation 3-20}$$

$$\dot{D}_{Pi} = a_5 \cdot \left(\left[a_4 \left(1 - D_{Pi}\right) \cdot \dot{\bar{\rho}} \right] + \left[a_6 \frac{D_{Pi} \cdot d}{\left(1 - D_{Pi}\right)^{n_2}} \cdot \left| \dot{\varepsilon}_p \right|^{n_4} \right] \right) \qquad \textbf{Equation 3-21}$$

It takes an extended time to calculate the large number of constants. Some of the constants, such as those with temperature dependence, require the input of two other

derived constants and an accurate measurement of temperature. By using the data gathered from the simple tests, it was possible to calibrate the constants for the full, physically-based constitutive equation set. However, if the chemical composition of the material was altered even slightly, this damage model is no longer valid and the tests have to be repeated to allow calibration of the material constants. With an increasing number of matching parameters there will be a larger range of values that appear to calibrate the equation set. The non-uniqueness of the parameters increases the difficulty in reaching the most accurate calibration. Conversely, the increased number of parameters means that they can be calibrated to any data set regardless of whether the phenomena are included in the model.

The damage equations are in terms of grain boundary and plasticity-induced damage, although, both sets of equations are similar. Both nucleation rate terms are based on the rate of increase of dislocation density and existing damage.

The damage growth rate equations are also similar (Equation 3-23 and Equation 3-26). They are both strain rate-dependent and both increase with pre-existing damage. However, the difference between them is mainly due to the grain size term and the exponent on the strain rate in Equation 3-26, n_6, which acts to reduce plasticity-induced damage at lower strain rates. On the other hand, the grain size term increases plasticity-induced damage with larger grain sizes.

The third equation in each set includes a stress-state term, as seen in Equation 3-24 and Equation 3-27. The damage grows in the direction of maximum principal stress and is related to the existing damage. Below a certain grain size, d_c, grain boundary sliding is less likely and dislocation-based deformation supersedes. This critical grain size is included in the grain boundary damage rate equation.

There is currently no interaction between inclusion-related damage coalescence and grain boundary coalescence, as shown in Equation 3-22 to Equation 3-27. The growth of grain boundary damage and plasticity-based damage are integrated together to create their total effect in Equation 3-28. However, this doesn't take into account their relative effect on softening behaviour. This may make the transition region, where both mechanisms are active, seem to be more ductile than should be expected.

$$\dot{D}_{gb}^{N} = a_7 \cdot \left(1 - D_{gb}\right) \cdot \dot{\bar{\rho}} \qquad \textbf{Equation 3-22}$$

$$\dot{D}_{gb}^{G} = \left[1 \Big/ \left(1 - D_{gb}\right)^{n_3} - \left(1 - D_{gb}\right)\right] \cdot \dot{\varepsilon}_p \qquad \textbf{Equation 3-23}$$

$$\dot{D}_{gb} = a_4 \cdot \eta \cdot \left(\frac{\sigma_1}{\sigma_{eq}}\right) \cdot \left(\dot{D}_{gb}^{N} + \dot{D}_{gb}^{G}\right) \qquad \textbf{Equation 3-24}$$

$$\dot{D}_{pi}^{N} = \left(1 - D_{pi}\right) \cdot \dot{\bar{\rho}} \qquad \textbf{Equation 3-25}$$

$$\dot{D}_{pi}^{G} = a_8 \cdot D_{pi} \cdot d \Big/ \left(1 - D_{pi}\right)^{n_5} \cdot \left(\dot{\varepsilon}_p\right)^{n_6} \qquad \textbf{Equation 3-26}$$

$$\dot{D}_{pi} = a_9 \cdot \left(\frac{\sigma_I}{\sigma_{eq}}\right) \cdot \left(\dot{D}_{pi}^{N} + \dot{D}_{pi}^{G}\right) \qquad \textbf{Equation 3-27}$$

$$\dot{D}_T = \dot{D}_{gb} + \dot{D}_{pi} \qquad \textbf{Equation 3-28}$$

This is a true phenomenological damage model with many constants to fit the results appropriately, since the damage model is based on experimental and empirical evidence.

One constitutive damage model, developed by Liu et al., was designed to be simpler (Liu, Farrugia et al. 2005). In Equation 3-29 the first term models nucleation of damage and the second term models growth of damage. The damage equation is coupled with the effective plastic strain rate equation. Though this model is less sophisticated it still requires calibration of five material constants.

$$\dot{D} = A_1 D \dot{\varepsilon}_p^{n_2} + A_2 \dot{\varepsilon}_p^{n_3} \cosh\left(A_3 \varepsilon_p\right) \qquad \textbf{Equation 3-29}$$

3.4.3 Foster

The model developed by Foster assumes that damage nucleation is a thermally activated process (Foster 2007). Therefore there is no nucleation term. There are two damage equations in the constitutive equation set. Equation 3-30 has two aspects: It includes a function of stress triaxiality and terms representing plasticity-induced damage. The stress triaxiality term is based on the Cocks and Ashby damage growth model (Cocks

and Ashby 1982). In the Cocks and Ashby model, *n* is the stress exponent for steady-state creep, which is a significant factor and it has to be determined for the model to be accurate. The model is based on grain boundary cavities growing by creep of the surrounding matrix.

The strain rate is included to relate the plastic growth of voids to the macroscopic plastic strain. The differences in the inclusion distribution factor, $\omega\left(=r^2/l^2\right)$, where *r* is the average inclusion radius and *l* is the average distance between inclusions.

$$\dot{D}_i = z_1 \omega \dot{\varepsilon}_p^{\gamma} \frac{\sinh\left[2\left(\frac{n-0.5}{n+0.5}\right)\frac{\sigma_m}{\sigma_{eq}}\right]}{\sinh\left[\frac{2}{3}\left(\frac{n-0.5}{n+0.5}\right)\right]} \qquad \textbf{Equation 3-30}$$

Equation 3-31 has several aspects to emulate observed features in hot fracture. The $\langle\ \rangle_+$ means that the value is zero if the contents are less than zero. This means that damage coalescence will only occur in a tensile stress state. The equivalent plastic strain rate is included as uniaxial test results have shown that strain to failure decreases with increasing strain rates. Coalescence in this model is based on a cracking mechanism. A localised stress concentration due to build up of dislocations eventually becomes so large that it can break the cohesive bonds in the vicinity and this will nucleate a crack tip. The crack will sink into the areas with high dislocation density, due to the available energy, and will terminate at the next void it encounters.

This would infer the possibility that coalescence is based on the local dislocation density around the damage site and not the average as is used for the coalescence equations. The works by Taylor and Forrest have shown that the mean free path of dislocations is proportional to the inverse of the square root of the dislocation density (Taylor 1938). The critical parameter for crack initiation is the reciprocal of the mean free path dislocations can travel. This is why the exponential function of the square-root of the dislocation density term is used. The sinh term controls the exponential increase in

damage coalescence that occurs at a certain volume fraction of damage and dislocation density.

$$\dot{D}_c = z_2 \cdot \dot{\varepsilon}_p \cdot \omega \left\langle \frac{\sigma}{1-D_c} \right\rangle_+ \cdot \sinh\left(z_3 \cdot \sqrt{\rho} \cdot D_i \right) \qquad \textbf{Equation 3-31}$$

3.4.4 Bau and Wierzbicki

All the aforementioned models follow a similar trend of increasing strain to failure with decreasing triaxiality. However, Bao and Wierzbicki proposed a dip in effective strain to failure as the triaxiality approaches zero due to the effect of mixed mode fracture on failure initiation, see experimental results in Figure 3.1 (Bao and Wierzbicki 2005).

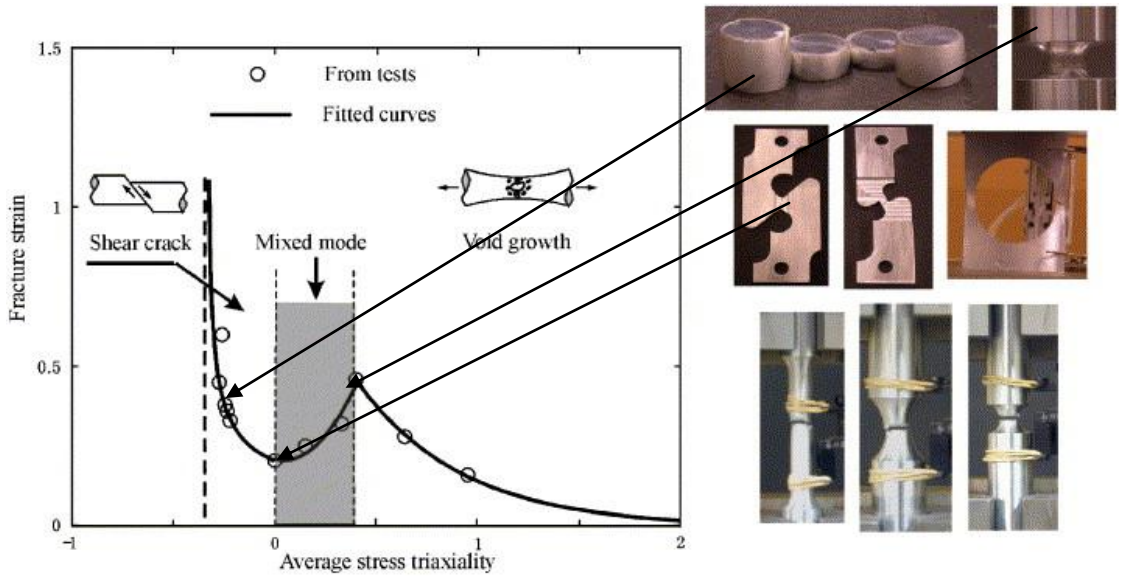

Figure 3.1. Bao–Wierzbicki fracture locus obtained through 11 different tests (of 11 different stress states), composed of four different regions (Bao and Wierzbicki 2005).

Wright looked at dynamic void nucleation and growth where the voids were modelled as thick wall spheres in an incompressible material (Wright and Ramesh 2008). It was argued that void growth is a function of pressure and time (see Figure 3.2).

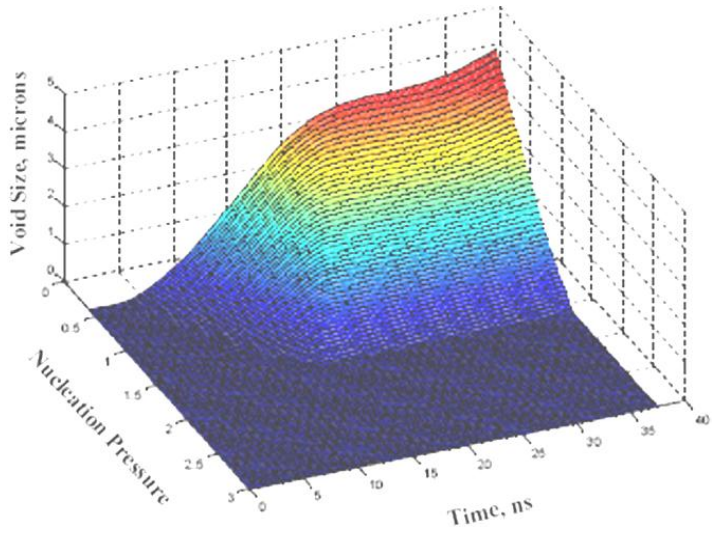

Figure 3.2. Surface plot of void size vs. nucleation pressure and time (Wright and Ramesh 2008).

3.5 Summary

The deformation parameters related to hot rolling were used to identify the active damage mechanisms were reviewed in Chapter 2. This information was used to identify the pertinent damage models. There are several established damage models whose origins are applicable for the hot rolling application.

There are several simple damage models, which are simplified by a range of assumptions. The assumptions allow for close approximations to be made over a limited range of temperatures and strain rates. The more complex models have the benefit of versatility by accommodating a greater range of deformation mechanisms. However, the number of constants requiring calibration makes the more sophisticated models difficult to implement.

Chapter 4 Design of high-temperature test for characterisation of damage in hot rolling

4.1 Introduction

An investigation into available test geometries is presented. Based on the investigation a test-piece was designed to emulate stress states similar to those in hot rolling and specifically for the evaluation of damage in hot rolling. Algorithms were developed to quantify the usefulness of the available test-piece designs. High temperature tests of the most appropriate design were performed. The conditions of the test are given and the test rig design is illustrated. The theoretical results, encompassing finite element analysis (FEA) of the damage models are compared to the experimental results, concerning damage measured from micrographs. The combination of FEA and micrographs allow the relation between stress triaxiality and damage to be evaluated.

4.2 Objective of test-piece designs

The test-piece design is integral to the gathering of good data. Any physically based models are only as good as the input data. This project is focusing on edge cracking in hot rolling and hence the mechanisms behind the formation of damage have to be investigated. As reported, a key factor in damage growth is the stress triaxiality ratio. The following section is a review of general testing methods and a critique for each test's ability to emulate the triaxiality inversion seen in hot rolling.

It has been reported by Kalpakjian that during rolling operations two phenomena occur in the material: The surface is hardened, leading to a greater stiffness and resistance in the thickness direction, and the fibres are oriented in the rolling direction, changing the directional response in the plane parallel to the rolling direction (Kalpakjian 1984). This project will focus on the former, which is effectively a ductility issue.

4.3 Survey of test-piece designs

The following is a description of several tests that can represent distinct stress states. The ranges of stress triaxiality are given, their uses and limitations are discussed. The fundamental aspect is whether they can be used to represent the stress states found in hot rolling. Therefore, the range of triaxiality is given first. These can be calculated from finite element simulations as well as analytical methods.

4.3.1 Uniaxial tension

$$0.33 < \frac{\sigma_m}{\sigma_e} < 1.5$$

This is a very useful test type due to the accuracy and range of average strain rate. It also bears the benefit of good uniformity of the deforming section up to a point. Uniaxial tension can be achieved in plane stress and axisymmetric conditions. The benefit that axisymmetric tension has over plane stress tension is that torsion can be applied as well as tension allowing controlled alterations to the stress state. The axisymmetric geometry's effect on triaxiality has been researched by Bonora who produced Figure 4.1 (Bonora 1997). Bonora et al. developed uniaxial tests with varying notch sizes to further analyse the triaxialities above one third.

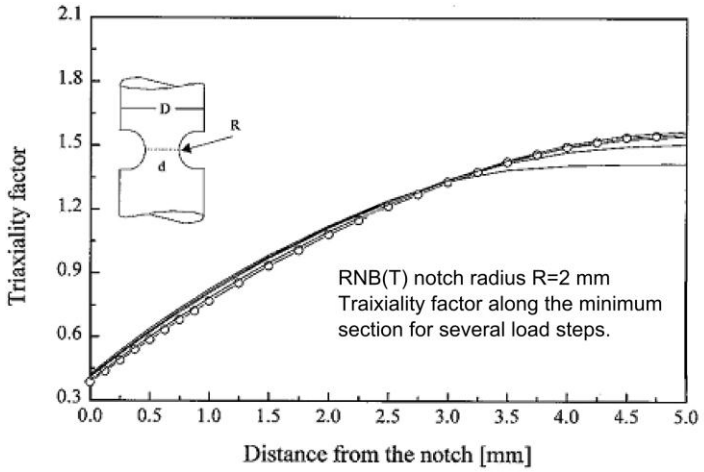

Figure 4.1. Range of triaxiality ratios in a uniaxial tensile specimen (Bonora 1997).

Liu et al. investigated axisymmetric tension as it is a method widely used to examine the microstructure and material properties of metals (Liu, Farrugia et al. 2005). Both single and double dog bones have been investigated. The single dog bone allows the failure surface to be revealed with micro and macro examination. The second notch can be sectioned to analyse the microstructure just prior to failure.

Upon necking, the stress state deviates from pure tension. Bonora argues that after necking the triaxiality ratio is larger in the centre leading to damage nucleating and growing faster at the centre of the test-piece generating cup-cone fracture (Bonora, Newaz et al. 2005). Therefore the microstructural response may be difficult to relate to the stress state.

Attempts to account for this have been made using the so called Bridgman method in uniaxial tensile tests, where the neck shape can be equated to a particular stress triaxiality (Bridgman 1953). X-ray tomography was used to quantify damage and relate it to the triaxiality in this way (Maire, Buffiere et al. 2001; Maire, Bouaziz et al. 2008). However, the spatial variation in stress state changes as the neck shape evolves and it is not possible to control and maintain a constant stress state after necking. Furthermore, the strain rate in the neck is difficult to control, complicating attempts to correlate damage to the conditions of loading.

Uniaxial tension has been related to rolling and it has been reported that the area of reduction and failure are proven to be proportional to reduction in rolling (Schey 1966). However, Thompson and Burmen argued to the contrary as well as Nicholson who found no corner cracking with strain up to 160% effective strain to failure (Nicholson, Smith et al. 1968; Thomson and Burman 1980). This test type is repeatable and useful for the calibration of constitutive equations but it does not allow accurate investigation into the effect of triaxiality on damage. There is difficulty in quantifying the stress state as the triaxiality is complicated by the influence of evolving notch size, changing notch radius and temperature localization during deformation.

4.3.2 Hot rolling tests

$$-0.4 < \frac{\sigma_m}{\sigma_e} < 1.6$$

Hot rolling tests have been used to investigate damage by several authors (Dodd and Boddington 1980; Thomson and Burman 1980). It has been reported that it is possible to add chamfer angles giving some control of the stress states to induce edge cracking (Cusiminsky and Ellis 1967). Wang et al. examined the effect of gas pressure on pore closure during hot rolling tests (Wang, Thomson et al. 1996). The hot rolling test will be representative of industrial rolling. However, there is a lack of precise user control on the stress state material temperature and strain paths making it hard to perceive damage mechanisms. It will be difficult to identify and hence examine the effect of triaxiality on void growth.

4.3.3 Torsion

$$\frac{\sigma_m}{\sigma_e} = 0$$

Several authors have investigated hot torsion (Trattnig, Kleber et al. 2008). However, in pure torsion the triaxiality ratio is zero, hence the stress state generated is not similar to rolling. However, tension and torsion combinations have been applied by Lin et al. for a variety of stress states. The torsion acts to lower the triaxiality (Lin, Liu et al. 2005; Lin, Liu et al. 2005). The hydrostatic stress is zero in pure torsion and it may be considered that the voids do not grow. However, damage can nucleate and existing voids will increase in length and decrease in width until they effectively become cracks. The stress building up between the voids leads to localised deformation and the material cracks. Due to the large strains possible, this method is useful for investigating damage under tensile triaxiality, especially ductile damage (Farrugia 2006). Torsion tests demonstrate that void nucleation, void growth and void coalescence occur by appreciably different mechanisms and are affected differently by stress state (Bao and Wierzbicki 2005). This contradicts models by Needleman et al. and Liu (Tvergaard and Needleman 2001; Liu, Farrugia et al. 2005).

4.3.4 Plane strain compression

$$-1.64 < \frac{\sigma_m}{\sigma_e} < 2.38$$

During plane strain compression the triaxiality ratio can range between –1.64 to 2.38 within a single simple sample (Foster, Lin et al. 2006). The test-piece can be sectioned along plane perpendicular to the section and the effect of stress state can be related to the damage generated in the sample. The stress state will be fairly uniform throughout the length of the test-piece allowing several comparable planes for examination.

It has been commented that rolling can be viewed as a plane strain compression (Rajak and Reddy 2005). However, the corners in the rolling process, which are of particular interest to this project, are not in plane strain.

4.3.5 Axisymmetric compression

This process allows investigation of a more complex stress condition. In simple upsetting tests there are mainly compressive forces but tensile hoop stresses formed on the equatorial line are similar to longitudinal stresses in the convex edges seen in rolling. It has been argued that this process is less useful for investigating causes of failure due to fast fracture (Clift, Hartley et al. 1990). However, failure has been investigated using this method. Thomason altered the friction, which causes barrelling, leading to observable fracture progression (Thomason 1990). Fracture using the upsetting method was also investigated by Clift et al. who found longitudinal fracture top to bottom (vertically) and oblique fracture at an inclined angle across test-piece barrelled surface depending on the height to diameter ratio (Clift, Hartley et al. 1990). It is also possible to deform a cylinder with a hole through the longitudinal centre to quantify the friction coefficient on the die surface. The ratio of D_{inner}/D_{outer} can be altered to change the triaxial stress state.

An axisymmetric test-piece can have many areas under the same stress state during deformation. However, it can be argued that an axisymmetric test-piece, such as a

cylinder, cannot demonstrate triaxiality inversion for investigation as the inversion is over such a small section (Foster 2007). However, the axisymmetric ‘double collar’ test-piece generated by Urshwood can show useful triaxiality inversion over a greater distance (Farrugia 2006). The same test-piece was investigated by Gouveia, who found that when the flange is cold it is in pure tension (Gouveia, Rodrigues et al. 1996)**.**

In a test by Yoshizawa and Ohsawa conical shaped dies match a conical shape removed from each end of the test-piece (Yoshizawa and Ohsawa 1997). This test (as seen in Figure 4.2) can be used to fine tune barrelling by altering the angle of the cone and hence triaxiality.

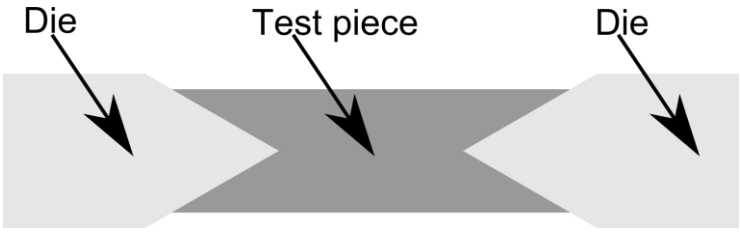

Figure 4.2. Axisymmetric test-piece design with conical ends.

Foster combined the above into a cylinder with longitudinal hole and conical base to allow better control of the triaxiality (Foster 2007). The hole acted to increase lateral spread, the internal conical shape at the base acted to reduce the effect of friction and increased the radial spread, resulting in high tensile hoop stresses towards the edge of the billet. High friction on the flat die and low friction on the conical die had the effect that the material was displaced outside the direct longitudinal compression path, which meant that high tensile triaxialities were created. The conical section gave a smoother transition between stress states. However, there are two issues in the test. The first issue is instantaneous cracking due to localized crack propagation and secondly, the stress inversions are over a relatively small area so their effects are difficult to analyse. If these issues can be solved the test will demonstrate damage mechanisms very effectively.

4.4 Survey conclusions

The most appropriate test to simulate the hot rolling of free cutting steel is hot axisymmetric compression. However, there are a range of appropriate tests and combinations of tests that fit within this specification. The ideal test-piece allows investigation into several of the highlighted stress factors, mentioned in the literature review, that are known to affect damage.

There are two ways that the triaxial stress can change, which are the instantaneous change in triaxial stress at a particular strain across a section of the test-piece or a change in triaxial stress for a sector of material during the straining. During the rolling process it is a sector of material that goes through triaxial stress inversion across the time of deformation. However, there is merit in investigating both varieties of stress inversion.

Triaxialities of -1/3 to 1/3 are often found in hot rolling (Kalpakjian 1984). Several test-piece designs exist for the evaluation of damage under stress triaxiality levels such as those found in hot rolling (Foster, Lin et al. 2009). The studies looked at a variety of plane strain and axisymmetric geometries and observed the damage formed after hot deformation. One plane strain test-piece was a flattened cube design with chamfers on the longest edges. The test-piece was compressed and produced different triaxial stress states by varying the initial chamfer angle. An axisymmetric test-piece, a tall ring with a concave conical base, produced a range of triaxiality similar to that in hot rolling. Different stress ratios and their relation to damage were investigated in each of the test-pieces by using finite element models. Damage models were implemented and compared to the observed damage found in experiments. The physical and experimental tests showed that the models matched the trends of the damage and highlighted its temperature dependence. However, there are nevertheless significant limitations with all the geometries available.

One limitation is that the volume in which damage can be observed relative to the size of the test-piece is often too small for meaningful conclusions. In many of the test-pieces the rate of change in triaxiality across the test-piece was too great and the spatial distribution of stress was not constant throughout deformation, making it difficult to relate the final damage formed to the stress state. Hence it is necessary to develop a test-

piece that can capture the effects of a range of stress states and stress components on damage.

Bao and Wiezerbicki recorded the strain to failure in cold forming aluminium for a variety of test-piece geometries (Bao and Wierzbicki 2004). They argued that each test-piece represented a particular value of stress triaxiality, which was plotted versus the strain to failure in the respective test-piece. The main problem with this approach is that for most geometries tested, the stress state was not constant throughout the deformation, therefore the test does not show the effect of any particular stress states on damage propagation.

4.5 Improving existing test-piece designs

Another limitation is that there may be effects of the inhomogeneity of the batch test material, hence each test will be slightly different, making it difficult to compare the results of particular test-piece geometries. A larger test-piece would mitigate the effects of the inhomogeneities, but this is not always practical due to limitations of material availability and loading capability. A smaller test-piece would have less chance of containing porosity or other randomly distributed defects. However, if high temperatures are used then a small test-piece will have localised cooling, hence reduced ductility, which would invalidate results. It would be preferable to have a single test-piece with a spatial variation of stress state that is relevant to the damage mechanisms being evaluated. Plane strain and axisymmetric test-pieces under compressive loading offer the best results in terms of the possible range of stress states, and provide large areas under the same stress state that could be compared.

It was necessary to compare the stress distribution using finite element simulations. A quad-dominated, structured mesh with axisymmetric, four-node elements, with linear interpolation was used. An explicit integration scheme was used and default hour glass control. The dies were modelled as rigid bodies and initially set in contact to the test-piece. A standard kinematic contact algorithm was used with a friction coefficient of 0.2 consistent with the findings of Munther et al. (Munther and Lenard 1995). Though it is known that the friction coefficient decreases somewhat during the rolling process, an

increase in temperature decreases the friction coefficient. Hence the friction coefficient was kept constant in the model as the variation is low over the range of temperatures considered (Lin, Huang et al. 1991; Munther and Lenard 1995).

A material model developed and calibrated for leaded free-cutting steels, LFCS, by Foster et al. was implemented using an *ABAQUS* Variable User MATerial, *VUMAT*, subroutine for explicit calculations (Foster 2007). It is a physically-based, temperature-dependent set of constitutive equations, which include parameters for the dislocation density, damage, strain rate and temperature. The other damage models reviewed in Chapter 3 were also implemented via the VUMAT subroutine. The commercial software *ABAQUS* was used to create finite element models of available geometries, several of which can be seen in Figure 4.3. The minimum mesh density was roughly 2 elements per mm^2. However, higher densities were used in areas of interest.

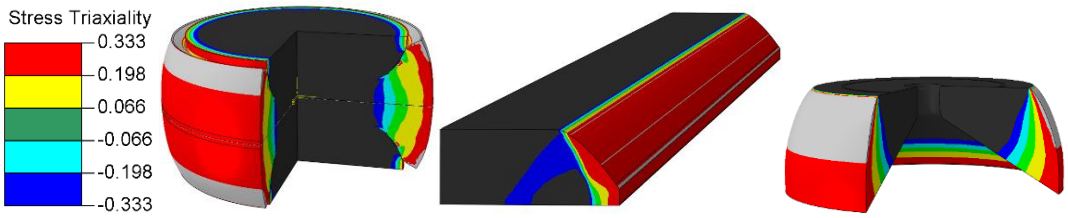

Figure 4.3. Compressive test-pieces (a) double collar, (b) plane strain hexagon and (c) cylinder with conical hollow. The values greater and lower than the legend are grey and black respectively.

Directly comparing by inspection the stress states between two different test-piece geometries is subjective. A program was developed, which provides a reliable and effective method for quantitatively comparing the various test-piece geometries. This facilitates the development of new test-pieces by iteratively combining the desirable aspects of known geometries by FEA. The key parameter used in the test-piece evaluation procedure was the stress triaxiality, however the program can be easily adapted to examine other parameters, e.g. the principal stress.

4.6 Evaluation of triaxiality gradient for optimum test-piece

The microstructure can be examined using micrographs of a polished section. In a single micrograph the entire microstructure will not have experienced the same stress and strain; a smaller range of stress (in this case triaxiality) in a micrograph allows a more accurate correlation between stress state and damage. In order to facilitate this, either the test-piece can be made larger for a given geometry or the geometry itself can be modified.

A scheme was developed for planar and axisymmetric FE models, which finds the spatial line on the model's cross section between two locations having specified limiting stress values, along which triaxiality varies monotonically with the optimal combination, using equal weighting, of lowest mean and standard deviation in slope of the triaxiality. This is desirable because it gives the greatest opportunity for studying the microstructure for the effects of triaxiality. For example the two lines shown in Figure 4.4 have the same mean slope, however line A has a standard deviation in slope of zero, whereas line B has a high standard deviation in slope. Line B effectively allows correlation of only a single triaxiality value to the microstructure (the plateau value).

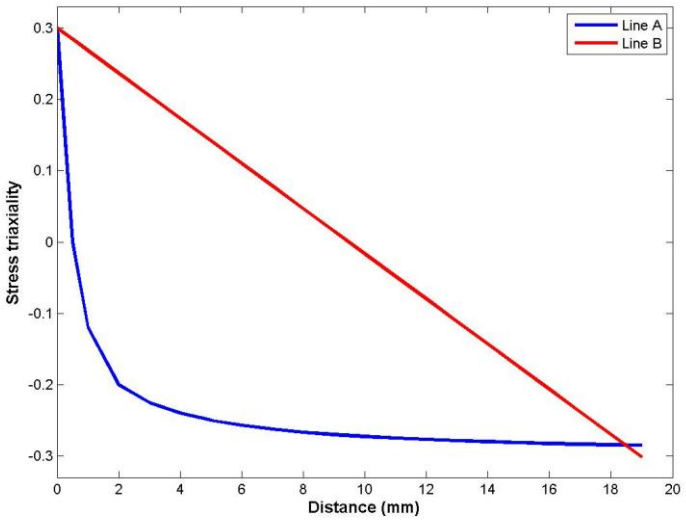

Figure 4.4. Graph of triaxiality with different spatial variations.

The coordinates and triaxiality at each node were exported from Abaqus into Matlab. A Delaunay tessellation algorithm connects a node to its three nearest neighbours with line segments. The algorithm assigns a number to each node and returns an *m* x 3 matrix, where *m* is the number of triangles required to fill the domain. Therefore each row relates to one triangle, where the three numbers in the row are the indices of the vectors of the triangle. The coordinates of each node are stored as vectors.

The slope of a plane is the change in the parameter in the *z*-axis over distances *dx* and *dy* in the *z-x* and *z-y* planes, respectively. Therefore, the gradient is calculated separately for the x and y coordinates such that:

$$\underline{\nabla} z = \frac{\delta z}{\delta x}\underline{i} + \frac{\delta z}{\delta y}\underline{j} \qquad \textbf{Equation 4-1}$$

The gradient at each node is associated with the gradients of triangles around it. The gradients of the projections of each line segment of a triangle are calculated in the z-x and z-y planes, illustrated in Figure 4.5(a). As each node is at the vertex of several triangles the gradients of each node are calculated from the weighted average of the gradients of the line segments around them, see Figure 4.5(b). The weight for a given node and line segment is the ratio of the distance from the node to the centroid of the line segment divided by the sum of those distances for all three intersecting line segments. Therefore, the spatial change of the triaxiality per unit distance was calculated for each node. The next section details how the code selects the optimal line through the test-piece taking into account these gradients.

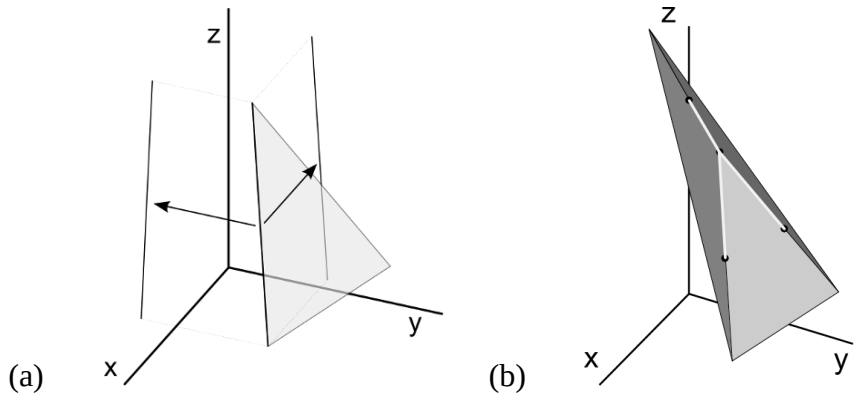

Figure 4.5. Calculating gradients at nodes: (a) Decomposition of line segments into *z-x* and *z-y* planes, (b) applying calculated gradients to node using weighted average.

The bounds for the investigation are the nodes whose associated parameter is equal to the specified, upper and lower, values. In this case the bounds are 1/3 or -1/3 stress triaxiality. Therefore, some nodes need to have associated values of 1/3 or -1/3. However, if the stress triaxiality at the nodes is not exactly 1/3 or -1/3 then the locations of the bounds cannot be identified. An iterative approach was taken to increase the range of each bound (i.e. $1/3 \pm 0.005n$, where n is the iteration number) to ensure that at least 30 nodal points were found on each bound. Lines from each node on the upper bound to each node on the lower bound are created. Figure 4.6 (b) illustrates a single line, in this case the 'optimum line', drawn between the upper and lower bounds.

The process for assessing a line, referred to as the original line, between the nodes on the upper and lower bounds will be considered in this paragraph. Two parallel lines, the outer lines, are created either side of, and parallel to, the original line. These lines are created to find the nodes in proximity to the original line, these nodes will be between the outer lines. There will be at least 15 nodes between the outer lines by increasing the distance between the outer lines. All nodes between the outer lines are said to be in proximity to the original line. The spatial change of the triaxiality per unit distance calculated for the nodes in proximity to the original line are recorded. The mean and standard deviation of the spatial change of the triaxiality per unit distance of the nodes is calculated. This process is repeated for the lines between the nodes on the upper and lower bounds. The longest line length and lowest average and standard deviation are the desirable qualities that used to compare each line. The process is demonstrated in Figure 4.6, with a representative example using a plate with a range of values of stress triaxiality.

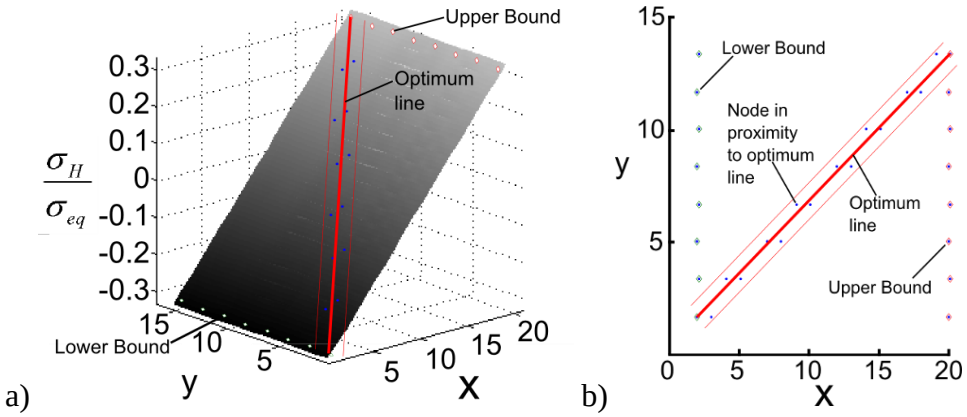

Figure 4.6. Sheet with a range of triaxiality applied to its nodes (a) 3D image of plane (b) representation of the code's output.

For each result, the line length and standard deviation in the slope of the triaxiality were compared to other test-piece designs. The various geometries were reviewed and where necessary further development and analysis was taken. The chosen geometry has the lowest and most constant rate of change of triaxiality between the chosen bounds across its section.

4.7 New test-piece design

The area of interest in terms of triaxial stress in an upsetting test is the location of barrelling, where triaxiality is tensile, hence where the propensity for damage is greatest. Similar stress states are created in test-pieces where radial spread occurs. This could be achieved in a test-piece in several ways, but the common obstacle is increasing the spatial size where the distribution of 1/3 to -1/3 stress triaxiality occurs and maintaining the distribution during deformation. Cross-sections of several typical geometries with contours of triaxiality are shown in Figure 4.7 (simulations were carried out as described in section 2). It was found that some geometries (e.g. 1, 3 and 4) initially displayed good stress triaxiality distributions but they were not maintained throughout the simulation, hence areas of interest experienced varied stress states during deformation. This is unavoidable but can be minimised through suitable alterations to the geometry.

Option 3, in Figure 4.7, has the lowest average slope in triaxiality, shown as greatest line length, and lowest standard deviation of the slope but the stress state

changed continuously throughout the deformation. This can most easily be shown by displaying the bounds of 0.1 to -0.1MPa of hydrostatic stress on the design, as in Figure 4.8; a point in the highlighted section of material experiences a certain stress state at a respective strain, but experiences a different stress state further into the deformation. This makes the relation of the damage to a particular stress state impossible.

By introducing a stem as shown in option 4 of Figure 4.7; the stress state can be maintained to a greater extent throughout the deformation whilst maintaining good line length and standard deviation in the slope of the triaxiality. It was possible to optimise the diameter of the stem. Option 4 is the new test-piece design.

Original geometry (dimension in mm)		Deformed geometry (optimum line highlighted)	Line length (mm)	Standard deviation of gradient	Percentage (max) variation at node with highest stress triaxiality
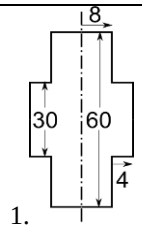	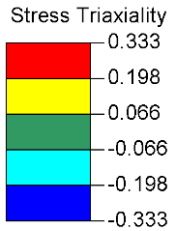	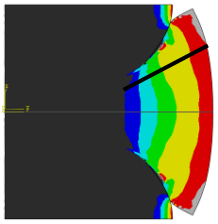	8.25	4.311	24% Max: 0.368 Min: 0.279
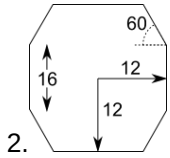		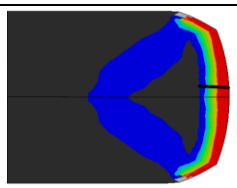	6.21	0.563	6% Max: 0.330 Min: 0.317
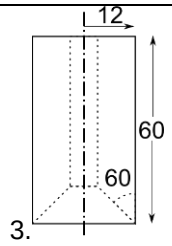		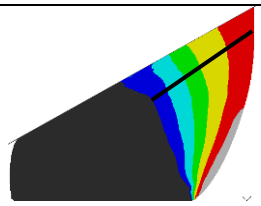	12.95	0.011	37% Max: 0.307 Min: 0.149
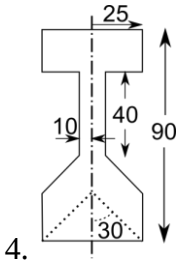		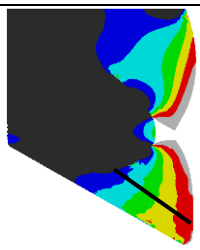	9.03	0.039	13.10% Max: 0.306 Min: 0.266

Figure 4.7. Comparison of several test-piece designs' stress triaxiality distributions during deformation.

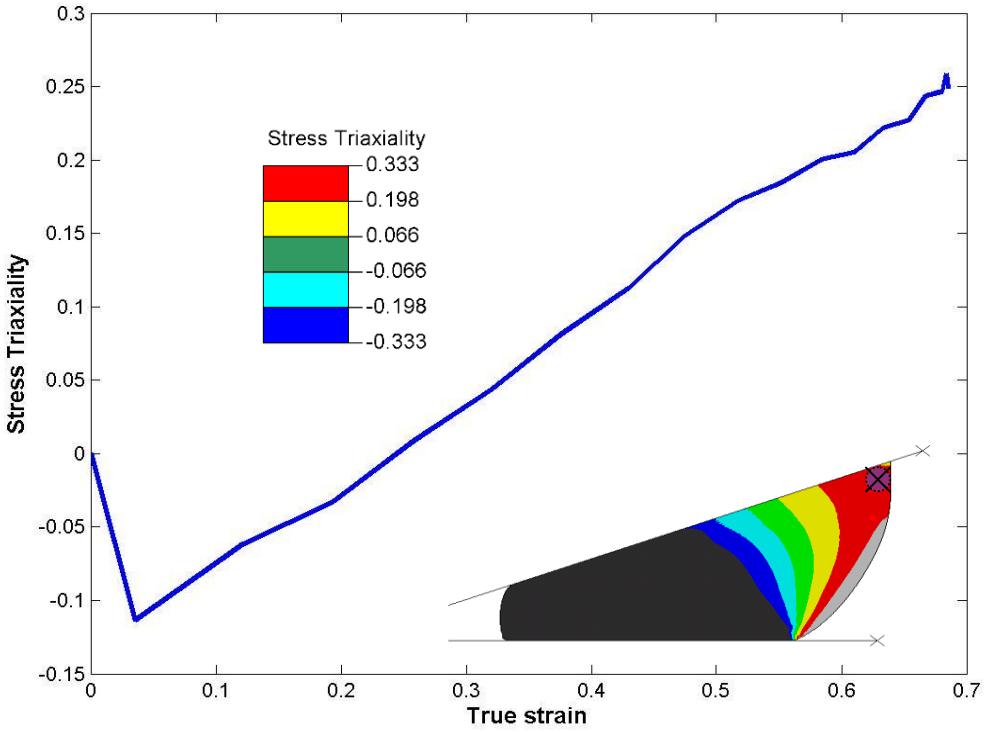

Figure 4.8. Highlighted point on option 3 test-piece experiences different stress triaxiality during deformation.

The new test-piece has three sections (see Figure 4.9); each section has a different stress state during deformation, allowing comparisons of the effect of different stress states on damage. However, the main area of interest is the conical section, where the useful distribution of triaxiality occurs. In addition to facilitating the creation of a desirable stress state in the conical sections, the other two sections reduce the heat loss from the conical section to the dies before deformation. The thinner the stem, the more stable the distribution in triaxiality during deformation, however the test-piece is more likely to buckle and the final strain in the conical section is reduced. The conical faces increase the radial strain in the conical section compared to a flat-faced cylinder. This test-piece can be used reliably for the quantification of the effect of stress state on damage in hot rolling.

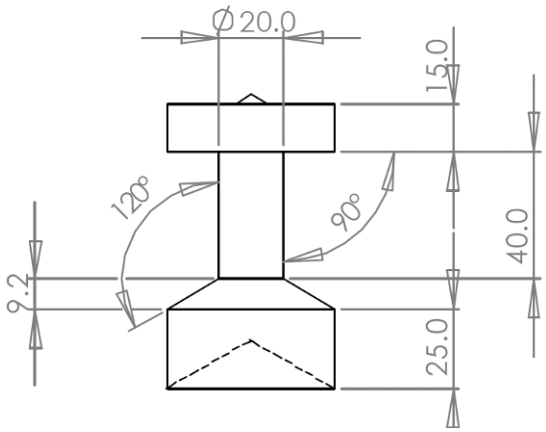

Figure 4.9. Chosen test-piece (units in mm).

4.8 Affect of increasing the test-piece size

The title of this section does not relate to *typical* size effects (such as grain size) but those relating the time for heating and cooling to the size of the specimens. The ductility does not relate to the size of the sample in the sizes being examined in this thesis. The required work per ligament area for the initiation of ductile fracture at the blunt notches in bending was shown to scale linearly with test-piece size (Krompholz and Kalkhof 2003).

The larger the test-piece, the smaller the range of hydrostatic stress over a given cross section of the material. Therefore, the exact stress state in a given microstructure study can be identified with greater precision. However, there are two effects of changing the size of the test-piece: The rate of temperature change during heating, transfer, forming and quenching, as well as the amount of force needed for compression are affected. Further, any inhomogeneities are better accommodated by a larger test-piece. Although, the as-cast porosity can be as large as 4 mm and will grossly affect any size of test-piece if present.

Air cooling will have a limited effect as long as scale builds up sufficiently to encase the test-piece. The rate of change in temperature for a simplified version of the test-piece geometry was calculated using the Boltzmann equation and the standard heat equation (see Equation 4-2 and Equation 4-3 below, where P is the energy (heat) emitted, ε is the emissivity, B is the Boltzmann constant, T is the temperature, Q is the heat

energy, m is the mass, C_p is the coefficient of heat transfer at constant pressure and ΔT is the change in temperature). The two equations can be calculated on an incremental basis; where the emitted energy is determined, using Equation 4-2, and the reduction in energy used to calculate the temperature drop using Equation 4-3 in each increment. The constants were based on those of a similar mild steel (Metaxas 1996). This simple model, based on a one-dimensional assumption, suggested a maximum temperature loss of 90 ºC from 1100 ºC over 20 seconds.

$$P = \varepsilon B T^4 \qquad \textbf{Equation 4-2}$$

$$\dot{Q} = mC_p \Delta \dot{T} \qquad \textbf{Equation 4-3}$$

Since the rate of temperature change for a larger test-piece (of the same geometry) will be lower, the temperature loss can be kept within reasonable bounds during the transfer from the furnace to the dies. The critical design consideration is the deformation force required.

During deformation the force required increases for several reasons: Work hardening, increase in cross sectional area normal to the applied force and a possible fall in temperature, leading to a harder material response. As stated previously, the temperature change should be small and therefore have a negligible effect, especially with a larger test-piece. However, it is necessary to calculate the maximum force, including work hardening, which will be required to deform the test-piece.

The force increases exponentially with increasing diameter of the test-piece. If the material is assumed to have constant volume and a yield stress, σ_y, of 124MPa then the force required to compress an equivalent cylinder, of diameter D, can be calculated using Equation 4-4, where the friction coefficient, μ, is 0.2 (Hearn 1997). Norton work hardening was included with a strain hardening exponent of 1.31 and a strength coefficient of 0.34 GPa, which were taken from a similar material in (Liu 2004). The strain was calculated using Equation 4-5, where h_0 is the original height of the test-piece and h is the current height (Kalpakjian 1984). The maximum test-piece diameter is 72 mm, set by the available material. A maximum required force of 5.5 MN will be required to compress a 72 mm diameter cylinder for a plastic strain of 1.4 and a strain of only 0.4

is possible on a 100 ton machine. Similarly, for a 52 mm diameter cylinder the force required is 2.5 MN at a strain of 0.6 and a strain of 0.87 is possible at the maximum 100 tonne force available on the machine.

$$F = \sigma_y \left(1 + \frac{\mu D}{3h}\right)\left(\frac{\pi D^2}{4}\right) \qquad \textbf{Equation 4-4}$$

$$\varepsilon = \ln\left(\frac{h_0}{h}\right) \qquad \textbf{Equation 4-5}$$

The FEA simulation of the hot deformation of the test-piece, described in Section 4.5, was used to analyse the three appropriate test-piece diameters. The reaction force in the direction of loading was recorded via a reference point attached to the top die. The 52 mm diameter version of the geometry is the most appropriate as it requires 60 tonne when at 1100 °C. However, the test-piece requires 90 ton at 850 °C, which is approaching the 100 tonne limit of the test machine and emphasises the importance of performing the deformation before the material cools on the dies. As reported earlier; if the test is conducted properly the test-piece will not cool beyond appropriate limits of 90 °C.

4.9 Experimental method

The tests were conducted at the upper and lower limits of the forming parameters seen in hot rolling; as described in Section 1 the temperature ranges between 850 °C and 1100 °C, and the strain rate ranges between 0.1 and 10 s^{-1}. The dominant damage mechanisms are labile within this range of strain rates and temperatures. The test parameters were chosen so that the effects of the various damage mechanisms would be visible in the microstructure of the deformed test-pieces. Therefore, the test-piece's suitability for studying particular phenomena could be established.

Leaded free cutting steel was studied in all tests; the chemical composition of steel is given in Table 4-1. The material was machined from an as-cast billet with a 500 mm square cross section. All material was taken at least 100 mm from the surface of the as-cast billet for a more homogenous microstructure, particularly in terms of precipitate size. There is an inhomogeneous distribution of 30-40 μm MnS inclusions within the material tested (Foster, Lin et al. 2006).

Table 4-1. Chemical composition of leaded free cutting steel (LFCS).

Element	C	Si	Mn	P	S	Other (Pb)
%weight	0.07	0.01	1	0.05	0.3	<0.5

The tests were conducted using a 100 tonne hydraulic press. The die set was designed specifically for the test-piece, see Figure 4.10. The dies are attached to mild steel platens; one is fixed to the columns, the other is free to glide vertically. Springs on the columns return the top platen to the starting position so that the test-piece can be placed between the dies. The lower die is circular and flat with a small conical impression matching a conical feature on the test-piece to locate the centre of the test-piece in the centre of the die. The upper die has a conical shape to match the test-piece.

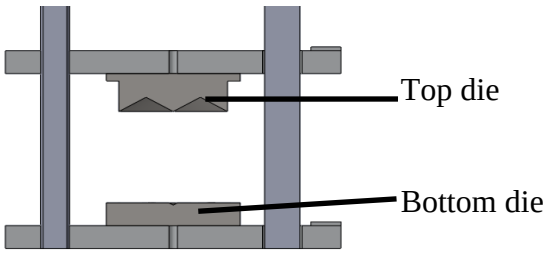

Figure 4.10. Die set; conical die on upper plate.

The material was heated to a temperature characteristic of hot rolling, in the range defined in Chapter 2. A schematic of the thermal history of the test-piece is shown in Figure 4.11. The test-piece had to be quenched by immersion in water with forced convection. It is important that the test-piece is cooled quickly to stop any recrystallisation, grain growth or other static changes. The outer surface of the test-piece cools much faster than the core. Thermocouples were inserted into the test-piece at different locations and depths. They were used to record the temperature during the heating, deformation and quenching of the test-piece. The difference in temperature at different depths within the sample was negligible relative to the temperature. The lowest heating and cooling rate is shown in Figure 4.11. The procedure is as follows:

1. The test-piece was heated in a muffle furnace to the desired temperature (either 850 °C or 1100 °C, for ‘cold’ and ‘hot’ tests respectively).
2. It was then held at the desired temperature to homogenise the microstructure and temperature distribution, during which time an oxide layer formed.
3. The dies were coated with a graphite lubricant, in accordance with (New York : Marcel 2004).
4. The test-piece was then transported to the test rig, during which time cooling occurred due to radiation and convection.
5. During deformation, plastic work lead to a temperature rise within the test-piece. However, cooling increased due to increasing contact with the cold tooling and exposure to air. Heat lost from the test-piece was mainly conductive but also radiative, which caused a drop in temperature of less than 40 °C by the end of the deformation.
6. The test-piece was compressed between the two dies by means of the actuator moving the top plate. The actuator was operated at 0.5 ± 0.01 ms^{-1} and 0.125 ± 0.01 ms^{-1} for the fast and slow deformation rates, respectively. During the deformation the stem of the test-piece deforms, which incurs barrelling, and the conical section deforms.
7. The diameter of the conical section increases and the material deforms until damage progression leads to coalescence and the conical section forms surface cracks.
8. After the forming process, the test-piece was quenched to freeze the microstructure.

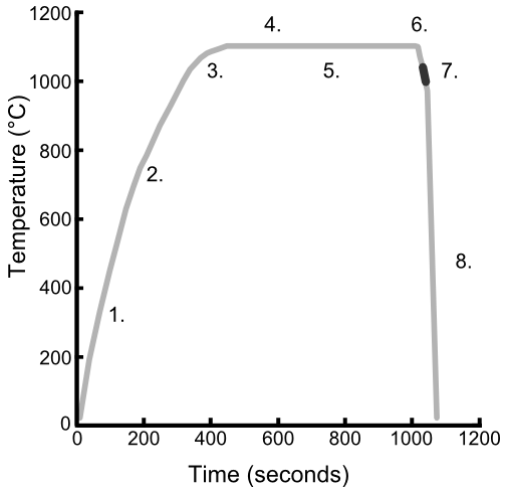

Figure 4.11. Temperature profile of test-piece during heating, soaking, deformation and quenching.

The rate of change of temperature (as shown in Figure 4.12) can be calculated from the thermocouple data using standard numerical differentiation; such as the cosec method and the seven point polynomial method. The test-piece was heated gradually in a muffle furnace at a rate of roughly 3.5 °C/s. It was then removed and placed on the dies (at 1000 s into the test). The average cooling rate for the test-piece on the die was -4.3 °C/s. The test-piece dropped roughly 35 °C in the 8 seconds whilst on the die.

The quenching rate alters significantly with time. This is probably due to the salt in the water interacting with and removing the insulating oxide layer. The average rate of change in temperature can be calculated at -76 °C/s. The test-piece cooled from 900 °C/s to 650 °C/s in 4 seconds.

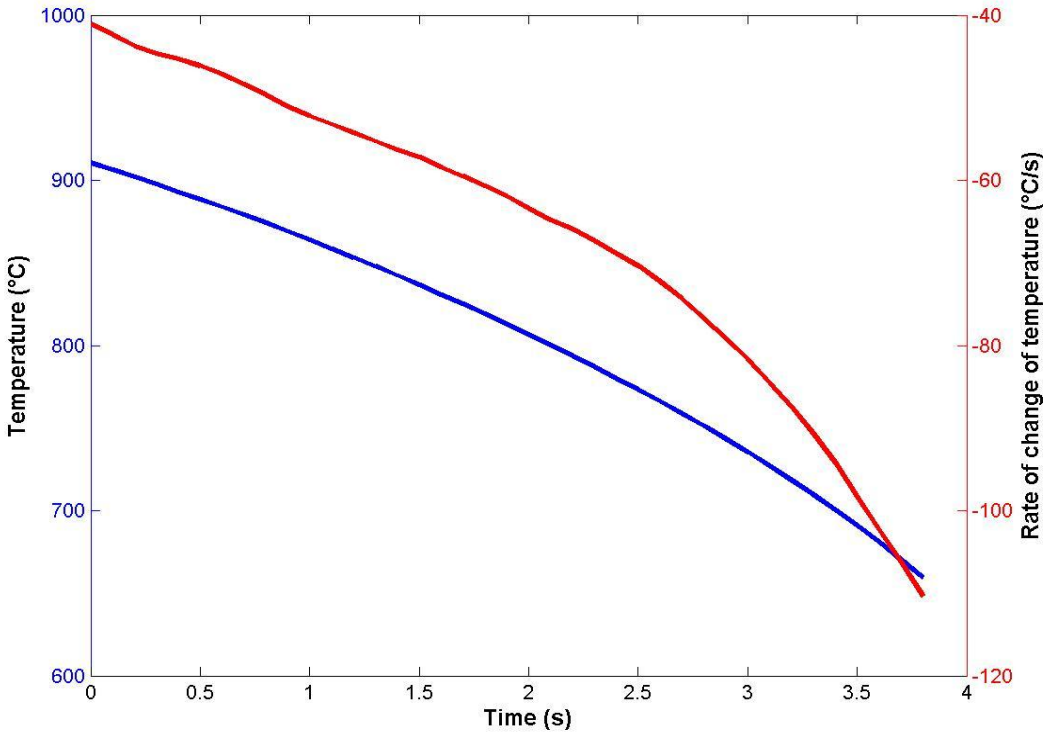

Figure 4.12 Temperature and quenching rate of test-piece during water quenching.

The quenching information is only useful when compared to a time-temperature-transformation diagram, see Figure 4.13. According to the figure the test-piece should form a fully martensitic structure. The fully martensitic structure, shown in Figure 4.14, was strong evidence that the material was fully homogenised during soaking and quenched successfully.

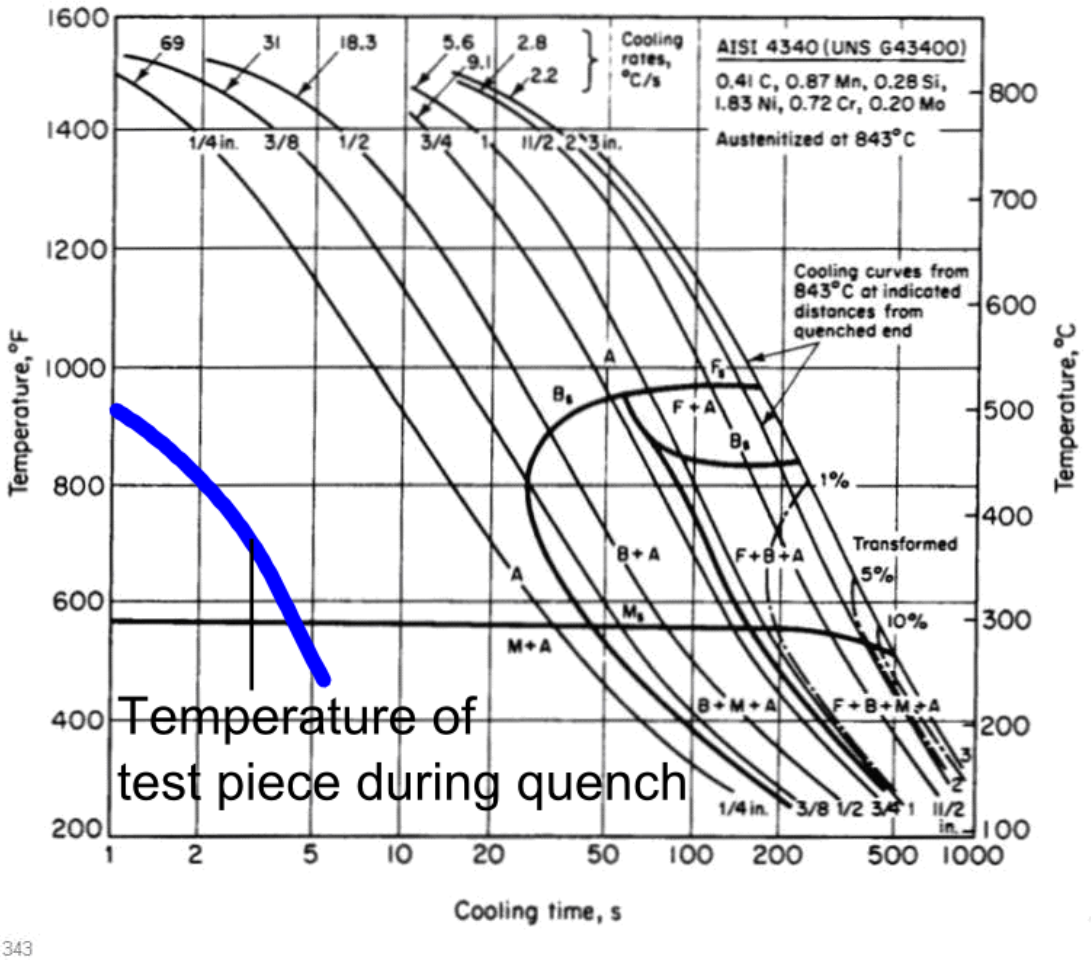

No. 343

Figure 4.13. Time-Temperature-Transformation diagram for a similar grade of steel to TATA FCS with measured test-piece temperature during cooling curve.[2]

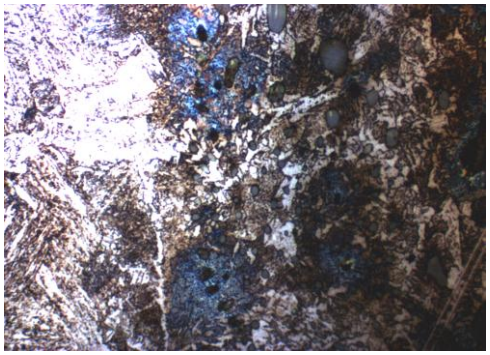

Figure 4.14. Martensitic structure observed in quenched free cutting steel.

[2] Courtesy of Bethlem Steel Company, USA

4.10 Results of mechanical testing

The theoretical results from this work encompass FEA of the damage models for the new test-piece, and the experimental results are concerned with hot forging of the new test-piece design and analysis of the damage measured from micrographs. As can be seen in Figure 4.15(a) and (b), the triaxiality is relatively constant with increasing strain in the range of triaxiality between -1/3 to 1/3. The distribution is relatively constant throughout the deformation at points A and C, e.g. changing by 5-10% in the tensile region after 10% strain at point C. The triaxiality changes with strain at point B, however, constancy with strain is most important at point C, near the surface where damage is greatest. The nearly linear (optimal) distribution along the line containing points A, B and C is shown in Figure 4.15 (c). This excellent result demonstrates the usefulness of the test-piece design for investigating triaxiality and the algorithm for developing the test-piece.

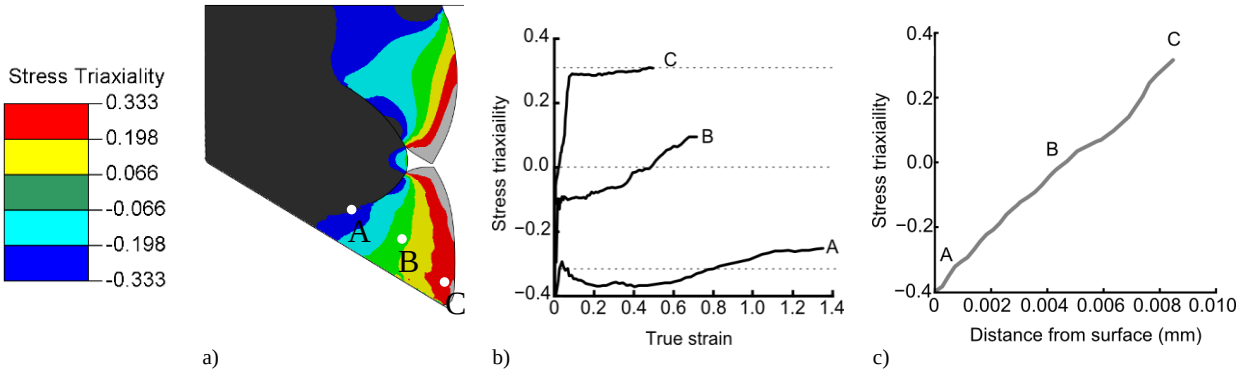

Figure 4.15. Distribution of triaxiality in the deformed test-piece a) finite element analysis (FEA), b) during deformation at three highlighted points and c) between two points in FEA.

The test-pieces were sectioned using Electrical Discharge Machining (EDM); the sections were cut as wedges of the axisymmetric shape. A further cut was made along the line A-C in Figure 4.15 (a), creating a planar surface perpendicular to the section shown in the figure. The surface was then polished to a 1 μm finish and micrographs were taken of the polished face.

Both plasticity and grain boundary damage could be seen in the micrographs (Figure 4.16). However, the relative amounts of each type of damage varied as a function of the test parameters. Examples of high rate with low temperature and low rate with high

temperature are shown in Figure 4.16 (a) and (b), respectively. There tended to be more plasticity induced damage around inclusions in the low temperature tests and more grain boundary damage in the high temperature tests.

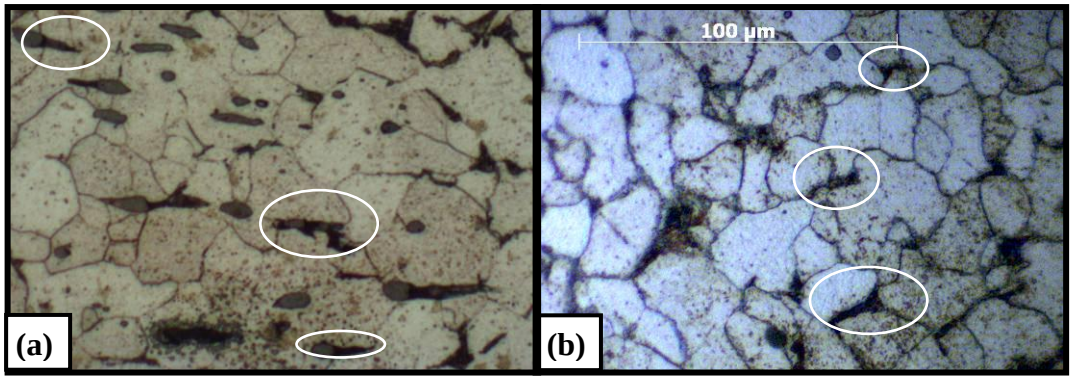

Figure 4.16. Two types of damage found; (a) fast low temperature test showing intragranular damage and (b) slow high temperature test showing mainly intergranular damage (scale is the same in both images).

A series of micrographs were taken from the surface of the test-piece, along the line from C to A in Figure 4.15, towards the centre until damage was no longer visible, illustrated in Figure 4.17. These images were concatenated into a single image. Damage was highlighted by contrast adjustment. The grain boundary and plasticity-induced damage were exported into separate layers in the image. The image was exported to Matlab and the scale bar was retained in the image in an area free from damage. Matlab converted the image to a binary w by h matrix, where w and h are the number of pixels in the width and height of the original image, respectively. Each value in the matrix was either zero or one, representing a pixel of damaged or undamaged matrix material, see Figure 4.18. The sum of each column of the matrix gave the damage per pixel from the surface of the test-piece. The scale bar was used to convert the distance in pixels to micrometers. The damage in each column was then divided by the maximum value for damage so that the value of damage ranged between zero and one, therefore allowing a comparison between the results of different tests to be made.

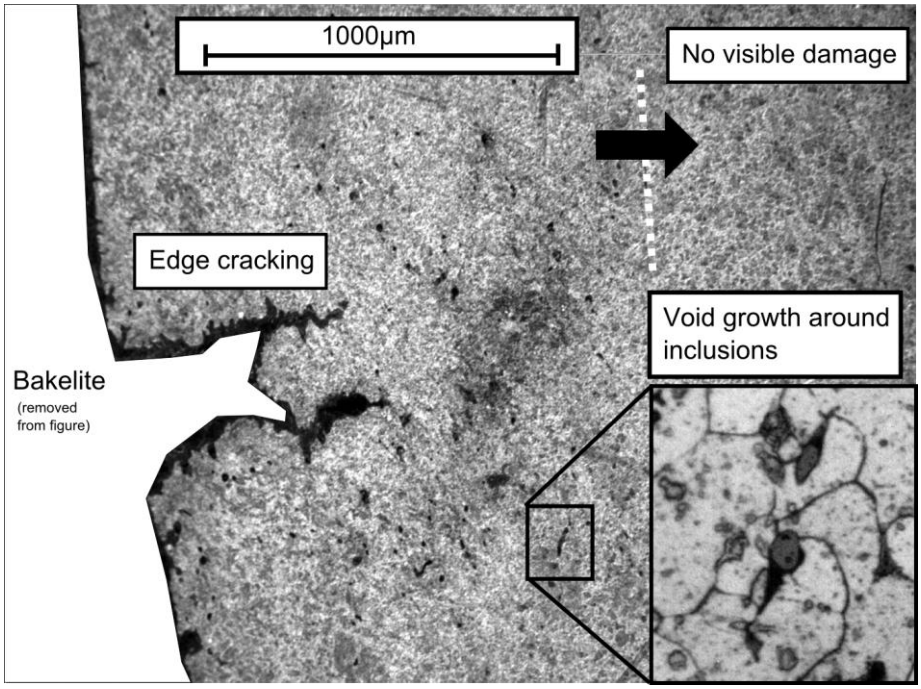

Figure 4.17. Damage distributed in section of deformed test-piece.

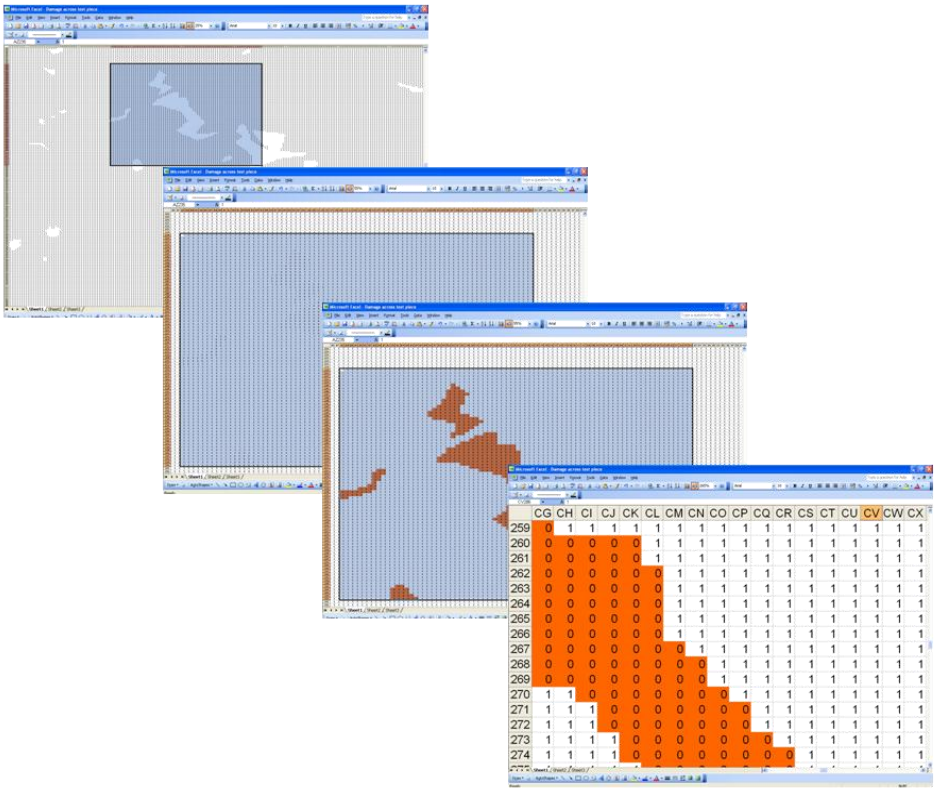

Figure 4.18. How damage sites are highlighted in a binary image.

In the higher rate tests highly localised damage occurred in the form of cleavage cracks, before significant damage growth could take place (see ‘not-ideal’ in Figure 4.19). This could be due to inhomogeneities in the microstructure. There are randomly distributed pores within the as-cast structure, which could act as local stress raisers and isolate damage to certain areas. The localised damage could also be caused by localised cooling due to the small size of the test-piece, which would leave areas with a lower ductility. However, the test was designed to avoid cooling of the conical end as contact with that section was only made when deformation was initiated. Voids created during the casting process can be as large as 2 mm in diameter. It is probable that this as-cast porosity would cause this kind of localised fracture, especially if it is close to the surface where higher triaxialities are experienced; indeed, this can be observed in Figure 4.19 (b). The tests conducted at low temperatures and higher rates failed in this way more often than the higher temperature and low rate tests.

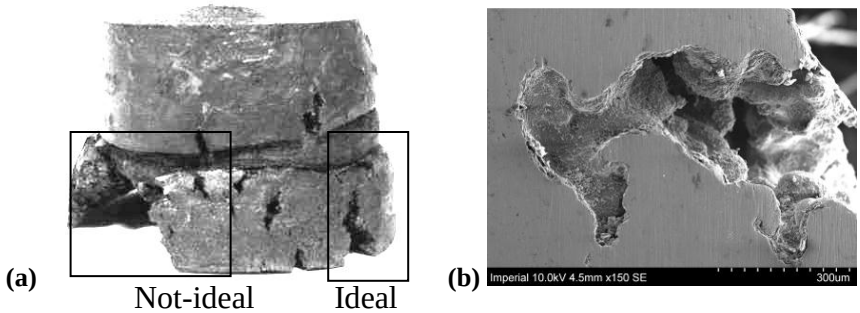

Figure 4.19. a) Test-piece, deformed at 900 °C at high rate, showing localised damage due to as-cast porosity b) as-cast porosity in LFCS.

Another test-piece that was reviewed for this paper, known as the ‘double collar’, has previously been tested with a similar free cutting steel (Farrugia 2008). The test was conducted using a much smaller test-piece having a 10 mm diameter; hence the region that experienced damage was small. However, a triaxiality of 1/3 was maintained close to the surface and the effect of inclusions was examined at that location. Figure 4.20 shows a comparison of the localised effect of inclusions on damage in the double collar test-piece and the same effect recorded in this study. The random distribution of inclusions

near the surface of the test-piece could explain why there was highly localised cleavage cracking in several tests, but not under the same conditions.

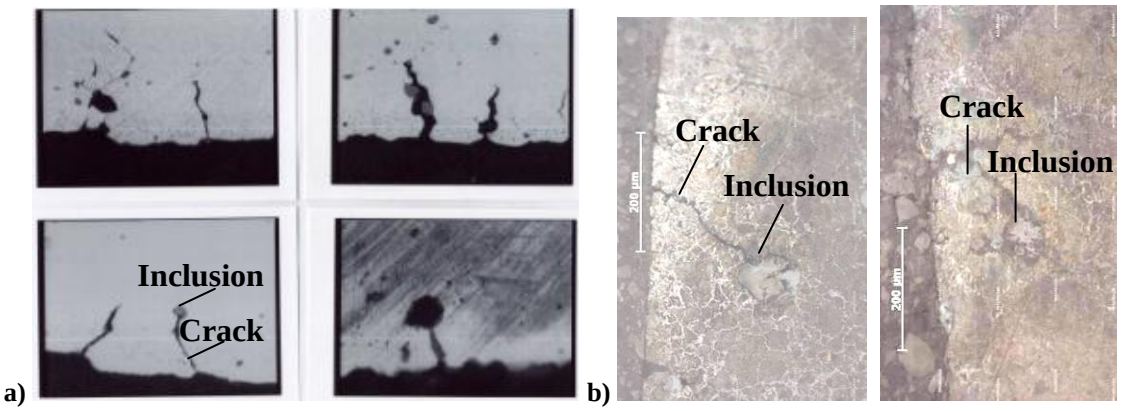

Figure 4.20. Inclusions close to the surface-accelerating damage; (a) double collar tests (Farrugia, Baillie et al. 2007; Farrugia 2008; Limited 2008) (b) current test-piece design.

Damage nucleation is thought to occur immediately due to the lead, precipitated at the inclusion-matrix boundary, melting at temperatures above 550 °C (Foster, Dean et al. 2007). Even without lead in the inclusion-matrix interface, some authors have concluded that the debonding energy at the MnS inclusion interface is negligible (Lenard, Pietrzyk et al. 1999).

Another notable damage mechanism seen in the microstructure was that of cracked inclusions, see Figure 4.21, which is probably due to manganese oxide (MnO) impurities in the inclusions (Farrugia 2008). It is generally accepted that inclusions greater than 5 μm in diameter will tend to contain microcracks as well as the possibility of impurities (Thomason 1990). The combination of debonding and inclusion cracking has been documented before (Garrison and Wojcieszynski 2007). As the inclusions in the material examined are between 20 and 40 μm, both inclusion debonding and cracking are expected in LFCS. However, it is more likely that inclusion cracking will occur in compressive stress states, where the void formed will be closed.

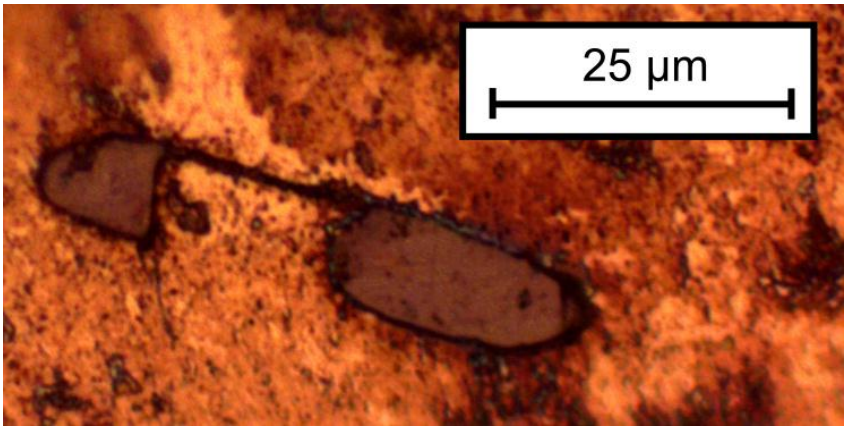

Figure 4.21. Inclusion cracking observed near centre of deformed test piece, where hydrostatic stress is compressive.

Work by Foster et al. on the test-piece depicted as option 3 in Figure 4.7 can be compared to this work (Foster, Lin et al. 2009). Inclusions are noted to have cracked, and coalescence was observed between neighbouring particles in regions where the triaxiality was -1/3. This was not observed in the current study. The stress state was found to alter significantly during simulations of the option 3 during test-piece deformation; this undesirable inability to associate a location with a particular stress state could explain Foster's observation of damage in negative triaxiality regions (Foster, Lin et al. 2006). This, however, is complicated by the local stress state, caused by the presence of the inclusion clusters. Generally, damage was found to be related to tensile triaxialities and coalescence due to cracks running normal to the local maximum tensile stress. Dunne et al. found that damage could be found around inclusions in compressive stress states in a titanium alloy using uniaxial compression test-pieces (Dunne and Katramados 1998). This has been attributed to the local stress state around the inclusion not being entirely compressive. It is stated that a tensile normal stress at the interface causes debonding. However, it is less likely that this will occur as the macroscopic stress state becomes even more compressive. Damage under compressive stress states will not coalesce by the mechanisms related to this work, hence can be ignored.

Some researchers have argued that voids will primarily occur at the interface between inclusions and the matrix, rather than at grain boundaries (Horstemeyer and Gokhale 1999). One such proponent of this theory developed a damage model for a

similar chemical composition of free cutting steel and removed all grain boundary damage from the material model (Foster 2007). It was argued by Foster that all observable grain boundary damage was related to inclusion-based damage, as it initiated at inclusions on or near the grain boundaries. This argument reduced the complexity of the model. However, grain boundary damage has been observed in tests conducted in this work, unassociated with inclusions.

Higher temperatures cause the relative inclusion-to-matrix plasticity to change, making the inclusions softer than the matrix and permitting the matrix to accommodate more deformation without debonding from the inclusions. As stored elastic strain energy both in the inclusions and matrix is lower at higher temperatures, there is less driving force for debonding. Instead, there would be more opportunity for grain boundary damage. However, even at the highest temperature, the grain boundary damage was not as prevalent as plasticity-based damage. The latter appeared to be the dominant damage mechanism in regions of tensile stress. However, as grains are three dimensional and generally irregular in shape, the line fraction of visible grain boundary damage is not necessarily representative of the actual area fraction of damaged boundary. As there are more grains than inclusions in the cross-sections, the grain boundary damage is more evenly distributed over the cross section than the plasticity induced damage. Further, individual voids tended to be smaller than those at the inclusion-to-matrix interfaces, making them more difficult to measure, and it is also possible that the material removed in the polishing process filled in some of those small voids (Maire, Buffiere et al. 2001). Hence, it is likely that the majority of the grain boundary damage was missed.

Not all inclusions showed debonding from the matrix in areas where damage growth was observed; this is in agreement with (Liu, Farrugia et al. 2006). There are three possible causes for this: One is that the lead was not evenly distributed at the inclusion interfaces (see Figure 4.22); the lead may have precipitated on a part of the interface where the normal stress was low or compressive, or the lead may not be present at the interface at all. Other possible causes are that the non-uniformity of the local stress state around individual inclusions may preclude damage growth in the plane examined. Alternatively, the orientation of the inclusions relative to the surrounding grains may be such that there is higher accommodation of the plastic strain. X-ray tomography could be

used to further clarify the role of lead in nucleation. Electron back scatter detection, EBSD, can be applied to study the role of relative orientation, but this is beyond the scope of this study.

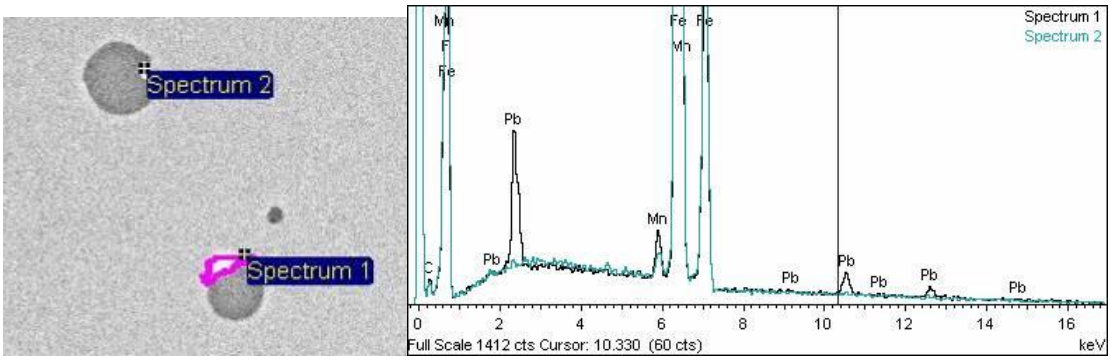

Figure 4.22. Variation in the LFCS distributions of lead at inclusion boundaries.

It is necessary to quantify the amount of damage occurring at both grain boundaries and at the inclusion-matrix interfaces in order to gain a satisfactory understanding of the processes. Despite the previously mentioned difficulties in measurement, the damage is plotted in Figure 4.23 along with the predictions of several models that have been calibrated for LFCS. The test-piece was designed to show the relation between damage and stress triaxiality. The result of Figure 4.23 (a) suggests that void growth around inclusions requires a minimum tensile triaxiality of 0.1.

Two repeat tests for each test condition were fully analysed and there was little to no grain boundary damage in the high rate tests, so a graph was not produced. The analysis of the micrographs showed that damage in the high-rate tests occurs irregularly. The perimeter of the conical section was measured for test-pieces where cleavage cracks led to premature failure, and in all cases the high rate tests had a smaller final diameter, at the conical section, than the low rate tests. Therefore, it could be concluded that the amount of strain required for coalescence is lower in the high-rate tests. Coalescence initiated at points of localised damage growth, due to inclusion clustering, inclusion alignment or other inhomogeneities in the material. The damage localisation of the inhomogeneities is more likely to occur in high rate tests.

The lower-rate tests permit more damage growth before coalescence due to the viscoplastic nature of deformation, allowing a more even distribution in damage from the

surface. The lower-rate results demonstrated grain boundary damage, which was found to occur in both tensile and compressive stress states. The actual amount of grain boundary damage is not easily comparable to the inclusion based damage, as the area fraction was far lower. Inclusions at grain boundaries may impede grain boundary sliding and resist diffusion flow. It has been reported that 60% of inclusions are found at the grain boundaries (Farrugia 2008). Therefore, it is possible that this decreases the possible grain boundary damage. The results reveal trends of damage mechanisms and indicate the quantity of damage related to stress state, but the interaction of the damage mechanisms is not clear. More work is required to understand and explain the complex interactions of grain boundary and plasticity-based damage mechanisms, as well as establishing their joint effect on coalescence.

FEA models were used to establish the variation in stress state with the distance from the surface. The measured area fraction of damage and the calculated damage from the FEA was then plotted against the stress state in the region examined (Figure 4.23). The damage plots that lay on top of one another were put into groups.

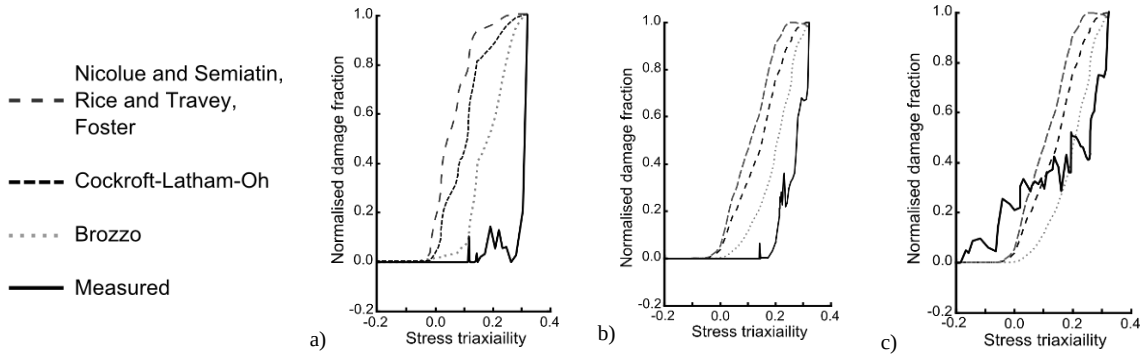

Figure 4.23. Void growth around inclusion versus stress triaxiality in the: (a) high-rate test and (b) low-rate test; (c) grain boundary damage in the low-rate test.

None of the damage models showed damage in compressive stress states. They all decreased at various rates from their maximum where the triaxiality is highest. However, the calculated amount of damage observed in tensile hydrostatic stress states can be divided into three groups. The model by Brozzo has the correct trend and is the most accurate, but the prediction is conservative. The Cockroft-Latham-Oh model also

overestimates damage but shows a change in the relationship of damage to triaxiality above a triaxiality of 0.1. A similar change in the relationship is noticeable in the other models, which almost plateau. Due to their exponential relationship to triaxiality, the Rice and Tracey, Nicolue and Semiatin and Foster models produced very similar results to each other. The Cockroft-Latham-Oh model produced a similar relationship but is noticeably closer to the measured result. The model by Brozzo, on the other hand, produced a more linear relationship to triaxiality than the other models. Most of the damage models did show damage at triaxialities less than 0.1, which was not observed in the measured plasticity-based damage. None of the implemented models captured the trend in grain boundary damage. On the other hand, the trends in damage are captured by the models, and, on a continuum level they are appropriate. However, as the damage growth predictions from the models are inaccurate, further development is required for a better fit to the measured damage.

The active damage mechanisms found in LFCS at different triaxialities are summarised in Figure 4.24. The relative proportions of the damage mechanisms varied with triaxiality and temperature. Grain boundary damage was only observed at high temperatures (shown in Figure 4.16 (b)). However, damage growth around inclusions (shown in Figure 4.16 (a)) prevailed over other damage mechanisms under all conditions.

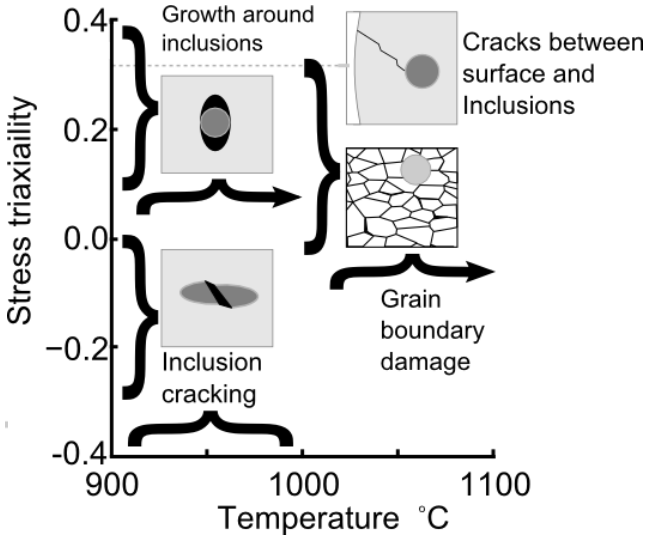

Figure 4.24. Damage mechanisms at various triaxialities and temperatures; arrows indicate the mechanism found up to melting.

4.11 Conclusions

A test-piece was designed that successfully demonstrates the effect of stress triaxiality on damage growth. The results can be analysed microscopically but comparison to finite element simulation is required to establish the stress states. The active damage mechanisms are altered by test parameters. Plasticity-based damage dominates at lower temperatures, but high temperatures and low strain rates permit grain boundary damage.

The experimental findings and model evaluation suggests that improvements could be made to the existing damage models. Plasticity-based damage is generally found to occur in the form of voids growing around inclusions. Inclusion cracking and cracks at inclusions close to the surface were also observed. Plasticity-based damage growth requires a tensile triaxiality of at least 0.1. Grain boundary damage is low in leaded free cutting steels but can be found in both tensile and negative stress triaxialities.

Chapter 5 Inclusion size and spatial distribution variation, and the effect on ductility

5.1 Introduction

This chapter will give examples and explain the detrimental effect that inclusions have on ductility. Following this, the results of varying the inclusion distributions on the ductility of high temperature uniaxial tensile tests are examined. Quantifying the change in ductility for different strain rates and temperatures is made by analysing the microstructure.

5.2 Background

Inclusions are a dispersed second phase of non-continuous material inside a continuous matrix. In the case of the free cutting steels described in this thesis, inclusions are mainly composed of manganese and sulphur. As discussed in chapter 2, their presence reduces the ductility of steel.

As the molten steel solidifies in the casting process, there is a temperature gradient that decreases from the centre to the surface of the billet. As the material cools the saturation limit is reached and second phases precipitate out. Precipitation will occur at energetically favourable locations, such as grain boundaries. The billet surface material remains at temperatures high enough to support inclusion growth for less time than the centre. The centre remains at higher temperatures for longer and the inclusions tend to nucleate at greater distances apart and are able to grow for longer periods of time. This leads to a variation in the size and spatial distribution of inclusions in an as-cast billet.

5.3 Damage related to inclusions

As demonstrated in the previous chapter, the matrix FCS carries the lead addition interstitially. The as-cast steel is often re-heated to forming temperatures (above 0.8 of the melting temperature, T_m) for rolling. These temperatures allow the interstitial lead to migrate to areas of high Gibbs free energy; preferentially the inclusion-matrix boundaries. The lead is liquid at temperatures above 600.61 °C and allows almost zero

cohesive strength between the inclusion and matrix. This effect was seen where the lead migrated to the inclusion-matrix interface (Foster, Dean et al. 2007).

Billet surface material shows damage softening at larger strains than the centre material (Foster, Lin et al. 2006). This response is thought to be due in some part to the smaller inclusions found in the surface of cast billets (Thomason 1990). Foster demonstrated that the smaller and further apart inclusions are, the greater the increase in ductility of FCS (Foster, Lin et al. 2006). This was represented by a factor ω, $=\left(d/l\right)^2$, which used the average diameter, *d*, and distance between inclusion centres, *l*, as a multiplier in the damage growth and coalescence rate equations. This effectively states that the rate of damage accumulation is proportional to the volume fraction of inclusions, f, due to Equation 5-1 (Shercliff and Ashby 1990). This agrees strongly with work by Thomason, who suggested that the strain to failure is proportional to the inverse of f (Thomason 1990). A similar factor was proposed, $\omega_{GG} = d^{1/2} / f^{1/3}$ (Gangalee and Gurland 1967).

$$f = \frac{2\pi r^2}{3L^2} \qquad \textbf{Equation 5-1}$$

The volume fraction is an important factor. However, for a given volume fraction, increasing the number of inclusions will increase the effective inclusion to matrix boundary area by $An^{1/3}$, where *A* is a constant and *n* is the number of inclusions. A larger number of smaller inclusions reduces the load-bearing cross-section but distributes damage growth over a larger area.

Transgranular and intergranular damage are both seen in hot deformation of FCS. Inclusions mainly affect intragranular damage. However, because 60% of MnS inclusions tend to form on grain boundaries, then they could also influence grain boundary damage (Farrugia 2008). Damage can be broken into various stages of its evolution. It is necessary to investigate the effect of inclusions on the nucleation, growth and coalescence of damage to establish the mechanisms at each stage.

5.3.1 Effect of inclusions on damage nucleation

Thomason has suggested that a critical stress is required for decohesion of the second phase from the matrix (Thomason 1990). Argon has put forward a concept for a critical strain, which decreases with increasing inclusion size (Argon, Im et al. 1975). However, there should be some dependence on the stress state (Brown and Stobbs 1971). Nucleation is expected in compressive, as well as tensile, stress states (Chan and Davidson 1999; Ervasti and Stahlberg 2005). Given a larger cross sectional area of inclusions in the surface material, the far field stress, σ_{field}, is more distributed. Therefore, a greater magnitude of σ_{field} is required to incur the local stress required for nucleation, σ_{crit}. A similar statement can be made about damage growth.

5.3.2 Effect of inclusions on damage growth

The shape of the growing voids is dependent on the triaxiality and the shape of the inclusions (Rice and Tracey 1969; Xia and Shih 1995; Kim, Gao et al. 2004; Bao and Wierzbicki 2005; Mashayekhi, Ziaei-Rad et al. 2007). It has been found that the voids tend to grow in the direction of principle stress and there is very little evidence of dilatational void growth in the stress states found in rolling (Lin 2004). Different size inclusions will have different local stress due to the distribution of the mean field stress state. The difference in size will affect damage growth rates. A homogeneous distribution of a larger number of smaller inclusions should dissipate the growth over a larger area. The growth rate will therefore be lower and it will take a larger strain before coalescence occurs.

Inclusion clustering is a known phenomenon reported by several authors (Foster, Lin et al. 2006; Farrugia 2008). The stress discontinuity caused by inclusions will be severely increased due to clustering. Although clustering has been noted, no attempt was made to evaluate its effect, in this section. A term to account for the likelihood of clustering and the magnitude of its effect is necessary for damage growth and damage coalescence models and is discussion in Chapter 7.

5.3.3 Effect of inclusions on damage coalescence

The coalescence of voids in FCS has been found to occur due to two distinct mechanisms: intersection and sheet. Intersection occurs via void growth, leading to the distance between voids being equal to the void diameter. The sheet mechanism requires the nucleation of a crack, which then propagates until it reaches another void. The active mechanism will depend on the strain rate, temperature and stress state.

In the case of the stress states experienced in hot rolling it is more likely that the sheet mechanism will be active. Benzerga et al. examined rolled material and took test-pieces at different orientations to the rolling axis identifying that coalescence will occur at a critical ligament size ratio (Benzerga, Besson et al. 2004). Weck used a laser to put circular voids at precise distances apart and demonstrated that the failure strain increased with void separation distance (Weck 2007). Therefore, the distance between inclusions is a critical parameter for coalescence if the damage nucleates at the inclusion-matrix interface. This mechanism is therefore greatly affected by inclusion clustering. The matrix is not homogeneously distributed with inclusions. Currently there is little modelling available to account for clustering.

Both of the above investigations demonstrate the active mechanisms but do not quantify the effect of the different inclusion size and distribution. A typical cast billet has a distribution of inclusions, which can be analyzed. The mechanism through which inclusion size and distribution affect the ductility at different temperatures is still not fully understood. Temperature and strain rate are known to be necessary for particular material mechanisms (Liu, Lin et al. 2005). This study will establish the effect of strain rate and temperature on the different inclusion distributions' influence on ductility. The following section describes uniaxial tensile tests, which have been used to compare the effects of temperature and strain rate on the matrix's ability to accommodate inclusions.

A mechanistic model has been developed to predict deformation and damage features during hot forming of steel, but which is generally applicable to a range of metal alloys experiencing grain-boundary-induced and plasticity-induced damage associated with inclusions or precipitates under hot forming conditions. The model takes into account the interplay of different key microstructural features, such as grain size, dislocation density, and inclusion or precipitate volume fraction and size. A cast billet's

surface material is known to be more ductile than the bulk material and acts as a protective layer against edge cracking during hot rolling. If the deformation parameters are changed then the surface and centre materials of the billet have different responses. Experiments with hot uniaxial tensile tests showed that damage rates varied with the average inclusion size and distribution in the different billet locations. The deformation parameters can be optimized to allow the surface material to increasingly inhibit edge cracking and increase formability. A discussion is presented accounting for the magnitude of the effect of inclusions at different strain rates and temperatures.

5.4 Experimental setup

5.4.1 Test material and facilities

The tensile tests were conducted using a Gleeble 3800. The test-piece is clamped between two electrically conductive jaws. The temperature is maintained using resistive heating with a feedback loop via a thermocouple, which is welded at the centre of the test-piece. A schematic of the Gleeble setup can be seen in Figure 5.1. Resistive heating allows precise control of the temperature but localises heating in the centre of the test-piece, which means that the gauge length can depend on the temperature. The length of the strained area is defined as the gauge length. Due to the neck in the chosen test-piece geometry, the gauge length is expected to be 6 mm, which is the length of the thinnest section where electrical resistance is a maximum (Figure 5.2). The gauge length was controlled by using a notched sample. The neck also reduced the effect of the temperature profile, allowing the ends of the neck to be within 5% of the control temperature.

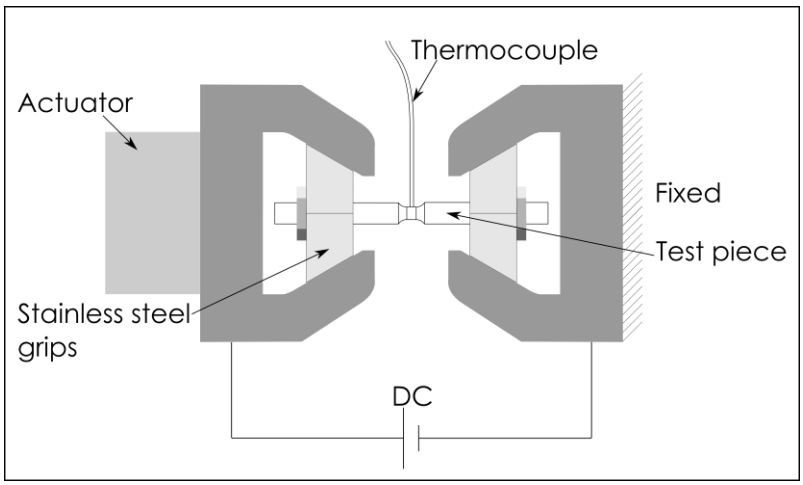

Figure 5.1. Schematic of Gleeble 3800 used for ex-situ testing.

The thermal cycle, which is shown in Figure 5.3, was designed to represent the typical reheat for the industrial hot forming operations. The soaking time of four minutes allows homogenisation of the microstructure. Following this, the test-piece was cooled to the test temperature of 900, 1000 or 1100 °C at which the test-piece was deformed (Figure 5.3 illustrates a temperature of 1000 °C). The displacement rate was controlled to maintain a constant strain rate of 0.1 s^{-1}. A C-gauge was used to record the change in diameter and the diametric strain was calculated. Several tests were conducted to failure to confirm the mechanical response and required displacement for particular strains.

The test-pieces were 10 mm diameter uniaxial cylinders with an 8 mm diameter notch, see Figure 5.2. The test matrix is shown in Table 5-1. The values represent the range of temperatures and strain rates experienced in a typical hot rolling schedule. Further to this, several tests at intermediate strain rates and temperatures were conducted to establish the nature of the relationships between these parameters and material response.

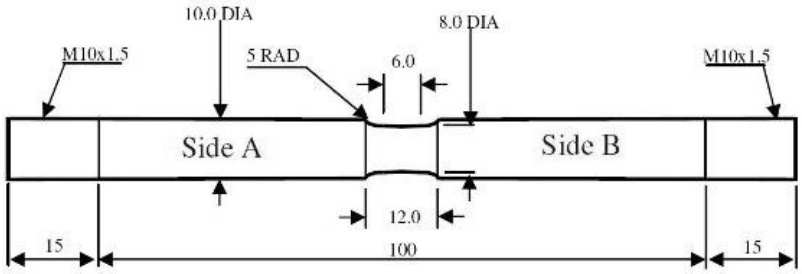

Figure 5.2. Uniaxial test-piece geometry (units in mm).

5.4.2 Test programme

Table 5-1. Test programme.

Test Number	Temperature [°C]	Strain rate [s^{-1}]	Material location
1	900	0.1	Centre
2	900	10	Centre
3	1100	0.1	Centre
4	1100	10	Centre
5	900	0.1	Surface
6	900	10	Surface
7	1100	0.1	Surface
8	1000	0.1	Centre
9	1000	0.1	Surface
10	900	1	Centre
11	1100	1	Centre

The chemical composition of the studied material is shown in **Table** 5-2. The samples were heated to 1200 °C at a rate of 40 °C/s and soaked for 250 s; the samples were then cooled at 10 °C/s to the test temperature and deformed. The thermal cycle is presented in Figure 5.3.

Table 5-2. Chemical composition of LFCS.

Chemical element	**C**	**Si**	**Mn**	**P**	**S**	**Pb**
%wt	0.07	0.01	1	0.05	0.3	<0.5

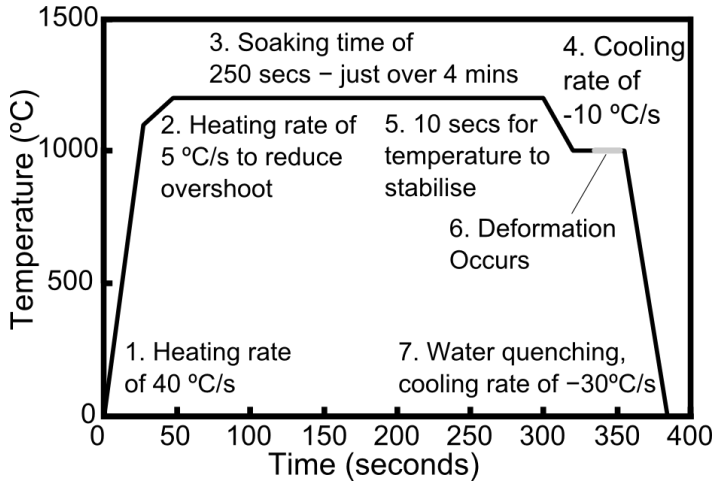

Figure 5.3. Temperature profile for test, highlighted section where deformation occurs at 1000 °C.

5.5 Effective gauge length

The Gleeble uses an electric current to heat the test-piece. However, this produces a temperature gradient between the clamps in a cylindrical specimen. The difference in temperature across the length of the test incurs a difference in material response across its length. Straining is localised around the centre of the test-piece where the temperature is highest.

The force, temperature and displacement data must be input into the Gleeble software. The displacement is calculated by rearranging Equation 5-2, where ε is the strain, l is the current gauge length and l_o is the original gauge length. Equation 5-3 is used to calculate the displacement for a particular strain and the time increment is calculated from the strain rate.

$$\varepsilon = \ln\left(\frac{l}{l_0}\right) \qquad \textbf{Equation 5-2}$$

$$l = l_0\left(e^{\varepsilon} - 1\right) \qquad \textbf{Equation 5-3}$$

5.5.1 Process

After the testing and quenching on the Gleeble, the test-piece was sectioned along the longitudinal direction. The samples were mounted in Bakelite and polished to 1 μm

surface finish. Micrographs of the samples were taken at this stage. The samples were then etched using a 0.5% Nittal solution.

Micrographs were taken in three areas, nearest the surface and at the centre as shown in Figure 5.4. Due to the different sizes of inclusions present, two different magnifications were used: 10,000 times and 50,000 times. The images were concatenated down the length of the surface.

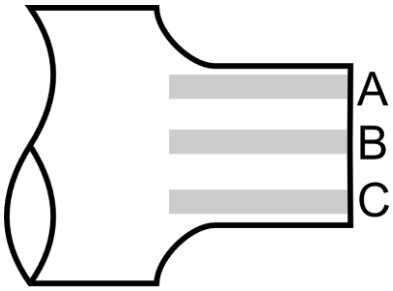

Figure 5.4. Section of test-piece, highlighting three areas examined.

The combined images were then processed to highlight the various damage sites and the inclusions. The quantified damage was then highlighted using the same method as described in Chapter 4, where the image is converted to a binary format and the amount of damage versus the distance from the fracture surface is calculated.

5.6 Experimental results and discussion

5.6.1 Effect of temperature

There is an increase in ductility due to the difference in inclusion distribution between the surface and centre of the billet material; the typical mechanical response of free cutting steels are shown in Appendix C. From here on, this increase in the ductility of the surface material will be referred to as the surface material ductility effect, or SMD effect. The percentages highlighted in **Table 5-3** are the change in strain to failure due to the different inclusion distributions; all other factors remain the same. The comparisons from here are made against the change in strain rate and temperature, and how they alter the SMD effect.

Table 5-3. Percentage difference in ductility due to material location.

Test Number	Temp (°C)	Strain Rate (s^{-1})	Material location	strain at failure	Percentage increase in ductility with surface material
1	1100	10	Centre	0.50	72.2%
2	1100	10	Surface	0.87	
3	900	10	Centre	0.33	48.5%
4	900	10	Surface	0.49	
5	900	0.1	Centre	0.36	60.7%
6	900	0.1	Surface	0.58	
7	1100	0.1	Centre	1.00	13.0%
8	1100	0.1	Surface	1.13	

Figure 5.5 (a) shows that the temperature alters the matrix's ability to accommodate different sizes and distributions of inclusions. The current models, which use a single factor for the effect of inclusion distributions, fail to include the mechanisms that the matrix uses to accommodate the inclusions under different test parameters. For instance, at lower temperatures the inclusions will be harder than the matrix and will debond from the matrix, potentially cracking along an oxide defect. However, at high temperatures the inclusions are reported to be softer than the matrix and will be easier to deform, hence there is less chance of voids nucleating around inclusions (Luo 2001).

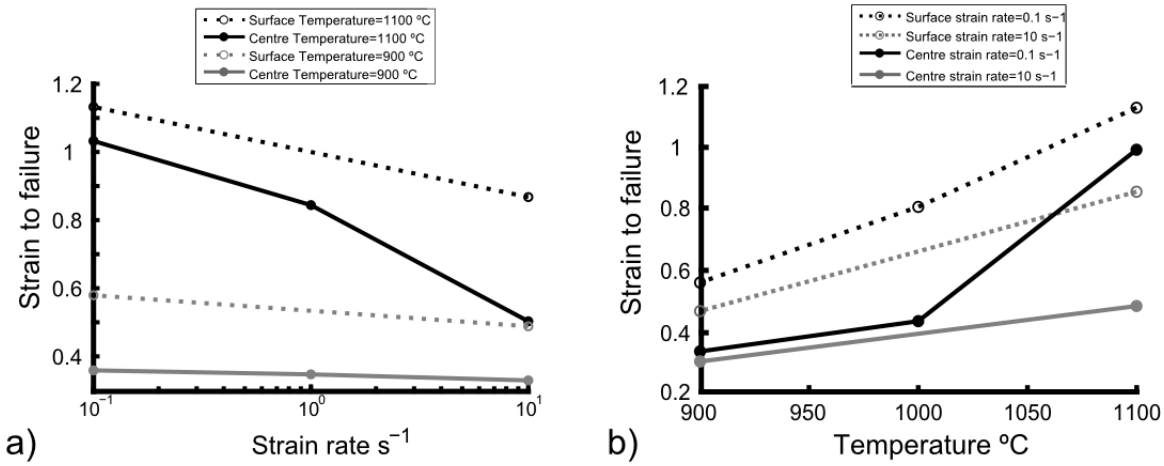

Figure 5.5. Strain to failure plotted against strain rate for two billet locations (dashed lines are for surface and solid lines are for centre billet material) for a) different strain rates; darker lines for lower strain rate and b) different temperatures; darker lines for higher temperatures.

The smaller inclusions will be harder to deform than larger inclusions, which may explain the decrease in the SMD effect at high temperatures. However, it is more likely that higher temperatures allow the energy for grain boundary-type damage mechanisms, which will be less affected by inclusions. The different mechanisms mean that a single factor is not appropriate, as the geometric effect will alter with active deformation mechanisms.

5.6.2 Effect of strain rate

A strain rate of 10 s^{-1} activates the same mechanism of inclusion accommodation in both centre and surface materials at low temperatures. However, at higher temperatures the centre material still forms voids around inclusions due to the larger stress discontinuities, whilst the surface material permits more grain boundary-type damage, hence the large difference in ductility. Two sets of micrographs from higher-temperature tests are shown in Figure 5.6. The micrographs show that variation in inclusion size makes a difference in the distribution of damage, with localized damage around larger inclusions in the centre material and highly distributed damage in the surface material. Enlarged images highlight the damage distributions in Figure 5.7, there is significantly more visible damage in surface material.

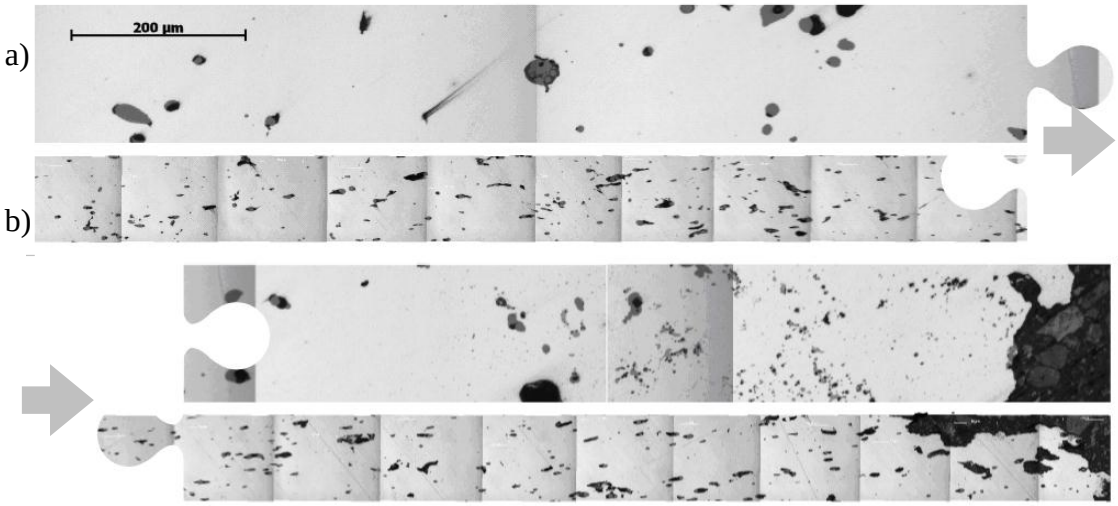

Figure 5.6. Concatenated micrographs of uniaxial tensile tests after deformation a) centre material (T = 1100 °C, $\dot{\varepsilon}$ =0.1 s^{-1}) b) Surface material (T = 1100 °C, $\dot{\varepsilon}$ =0.1 s^{-1}).

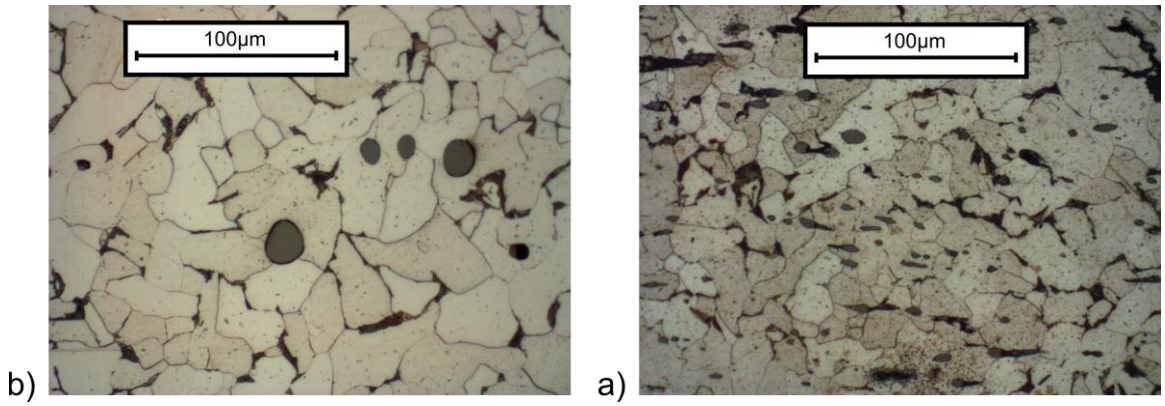

Figure 5.7. Single micrographs of uniaxial tensile tests after deformation a) centre material (T=1100 ℃, $\dot{\varepsilon}$ =0.1s^{-1}) b) Surface material (T=1100℃, $\dot{\varepsilon}$ =0.1s^{-1}).

The SMD effect can be partly accounted for by a factor, which includes the spacing and size of the inclusions in the form of $\omega_0 = d/l$. The two solid lines in Figure 5.5 b) demonstrate a linear correlation of the strain to failure and natural log of the strain rate. However, the different gradients of each line will be due to the interaction of various material mechanisms on the SMD effect. Given that the temperature and the strain rate are shown to alter the magnitude of the SMD effect, it is necessary to accommodate this by introducing a phenomenological parameter in an inclusion factor. The combination is given by Equation 5-4, where $\dot{\varepsilon}^0$ and T_o are material dependant constants. The equation

alters the magnitude of the inclusion distribution factor in accordance with the results described previously where a lower strain rate or a higher temperature diminishes the SMD effect.

$$\Omega = \omega_0 \left(1 + \frac{\ln \dot{\varepsilon}}{\ln \left| \dot{\varepsilon}^0 \right|} \right) \left(1 - \frac{T - T_o}{T_o} \right) \qquad \textbf{Equation 5-4}$$

This simple formula encapsulates the observed phenomena in the experimental results. It can be included in a plasticity-based damage equation to better model the effects of inclusion size and spacing on ductility. The constants $\dot{\varepsilon}^0$ and T_o are in the region of 2.3 and 1000, respectively. The constants could be calibrated with further testing but represent the turning points in the SMD effect as seen in the results. The factor to account for the SMD effect is shown to increase at lower temperatures and higher strain rates

The deformation parameters can be altered in industrial forming processes to increase the usefulness of the SMD effect. Before a forming process, such as hot rolling, the steel is reheated. This homogenises the microstructure but allows an oxide layer to form. Too high initial forming temperatures will turn the protective surface layer, with smaller inclusions, into oxide, which must be blasted off to avoid being rolled into the product. A lower reheat temperature will preserve the protective layer at the cost of increased forming pressures. However, a greater ductility will be observed with a lower reheat temperature as the tests 3 and 4 as well as 5 and 6 (see Table 5-1) indicate. The protective surface layer will eventually turn to oxide.

Higher strain rates are less detrimental to the surface than the centre material ductilities as seen in tests 1 and 2 compared to 7 and 8. If the reheat temperature remains high but the majority of deformation is to be completed before the surface layer is oxidized using high forming rates, then the overall formability could be improved.

The surface material has a larger number of inclusions but the same volume fraction found in the centre material. Therefore, there is a larger inclusion to matrix contact area in the surface material. The inclusion-matrix boundaries are known to be nucleation sites for damage. The average mean free path is reduced in the surface material, which should increase the hardening. The dislocation pile ups that cause hardening are also known to cause damage. This should mean that if dislocations had

significant interaction with inclusions then the rate of hardening should be increased in the surface material. It can be seen that the rate of hardening is similar in the centre and surface material in both high and low rate tests, as shown in results in Appendix C; Figures 9.2 and 9.3 respectively. Therefore, dislocation-inclusion interactions can be ignored.

The centre material has larger inclusions with larger and hence further reaching stress discontinuities. This is why the ductility is lower in the centre material. During the 'fast and cold' test the larger number of inclusions in the surface material allows a greater distribution of damage growth, which means that it takes greater strain for coalescence to take place. In the 'slow and hot' tests the grains have greater ease in deforming around the smaller inclusions.

5.7 Conclusions

As a cast billet cools, the manganese sulphide inclusions precipitate out at different rates according to the depth, due to the variation in temperature through the cross section. The different distribution of inclusions causes the surface to have better ductility than the billet material at the centre of the billet; this has been termed the 'surface material ductility' or SMD effect. The SMD effect can be related to the measurable inclusion sizes and distributions.

The SMD effect is altered by strain rate and temperature due to the matrix's varying ability to accommodate the inclusions under different forming parameters. The SMD effect is more apparent when plasticity-induced damage would normally dominate. High temperatures and low strain rates activates different accommodation mechanisms for a matrix with a second phase of different sizes.

A simple size and spatial factor is inadequate to encapsulate the effect of inclusions in a matrix under hot deformation conditions. An updated inclusion size and spacing factor is presented, which includes the effects of temperature and strain rate.

A lower reheat temperature before a hot forming operation or higher initial forming rates will preserve the protective surface layer, and therefore increase the overall formability of the billet.

Chapter 6 Metallurgical and mechanical characterisation of the materials through tension testing

6.1 Introduction

The following section details the variation of the material properties due to the different additions in the free cutting steels. The damage mechanisms are established for each steel. A comparison between the steels' different mechanical responses and ductility is made and explanations for the relative differences are given.

6.2 Alloying elements in FCS

As described in Chapter 2, steel is often machined after it is rolled, and there are additions of heavy metals that aid the machining process. Lead is by far the most common additive element due to its relative cost and availability. Other heavy metals, such as bismuth and tellurium, have similar chemical properties. Because of directives such as *2000/53/EC*, which promote replacing lead with alternative additions of heavy metal alloying elements to steel, it is predicted that more rigid guidelines will soon be enforced. Therefore, investigation of the use of bismuth and tellurium has been undertaken due to their similar ability to aid machining and their reduced toxicity compared to lead. Their similar attributes are due to their similar position in the periodic table. However, they are rarer and significantly more expensive than lead (George 2008).

Tellurium has a smaller atomic radius than bismuth and lead, as can be seen in Table 6-1. The smaller atomic radius may increase the diffusion of tellurium to the inclusion-matrix interfaces. The melting points of each element are well below the forming temperature of the free cutting steels. Although tellurium has the highest melting point, it also has the lowest boiling point, at 1261 K, which is close to the upper limit of the forming temperatures.

Table 6-1. Material properties of bismuth, tellurium and lead.

	Tellurium, Te	Lead, Pb	Bismuth, Bi
Atomic mass pm	127.6	207.2	208.98
Atomic number	52	82	83
Density g.cm^{-3}	6.24	11.34	9.78
Covalent Radius pm	135	147	146
Atomic Radius pm	140	175	170
Melting Point (K)	723	601	545
Boiling Point (K)	1261	2022	1837

There were three steels investigated: A plain Free Cutting Steel (FCS), FCS with Tellurium (TE-FCS), FCS with Bismuth (Bi-FCS); their chemical compositions are given in Table 6-2. It is well known that variation in alloying elements, other than heavy metals, affects the material response (Callister 2007). The percentage carbon content amongst the steels is different.

Table 6-2. Chemical composition of various free cutting steels.

	Element %weight					
Variety	C	Si	Mn	P	S	Other
FCS	0.07	0.003	0.98	0.059	0.31	n/a
Bi-FCS	0.07	0.004	1.03	0.063	0.28	Bi (+ <0.007Pb)
Te-FCS	0.36	0.18	1.49	0.015	0.27	Te

6.3 Objectives of experiments

There were two objectives for the examination of three different free machining, or free cutting, steels. The objectives were to investigate the relative ductility and establish the damage mechanisms for a range of temperatures and strain rates. Previous studies on leaded FCS showed that the materials are strain rate and temperature dependant (Foster 2007). The free cutting steels to be investigated will be similarly dependent on those parameters and the relative effects were investigated. As described in Chapter 2, the range of strain rates experienced in the industrial process are between 0.1 s^{-1} and 10 s^{-1}, and temperature are between 900 °C and 1100 °C. High strain rates and low temperatures permit different material mechanisms than low strain rates and higher

temperatures where creep can occur (Hayhurst, Lin et al. 2008). The upper and lower limits of the parameters were applied to ensure that the most disparate mechanisms were activated.

6.4 Uniaxial tensile test program

The specimen design is a standard G4A axisymmetric specimen, the design of which was reviewed in Chapter 5. The test programme is similar to previous test matrix presented in Chapter 5. The thermal profile follows the 5-stage process: Heating, soaking, cooling, stabilising for deformation and quenching, as shown in Figure 5.3. All tests were performed on a Gleeble 3800.

Ductility tests for the ductility of materials have been performed on a range of materials using a variety of test geometries by other researchers (Kalpakjian 1984); several geometries were reviewed in Chapters 4. For example, tests to compare materials have been carried out to demonstrate the effects of external pressures (Bridgman 1953), orientation (due to inhomogeneities or anisotropy (Hosseini, Temmel et al. 2007)) and material ductility comparisons under the same testing conditions (Foster 2007). The tests by Foster demonstrated the relative ductility of two free cutting steels. However, the tests made no effort to explain the differences. An understanding of what permits increased ductility can be used to aid production.

The material tested in this work was taken from the surface and the centre of the billet. The surface samples were taken from within 15 mm of the surface. There were three steels investigated: A plain free cutting steel (FCS), FCS with Tellurium (Te-FCS), and FCS with Bismuth (Bi-FCS). There were two tests performed on each material: A 'fast and cold' test with a strain rate of 10 s^{-1} and temperature of 900 ^{o}C, and a 'slow and hot' test with a strain rate of 0.1 s^{-1} and temperature of 1100 ^{o}C. The tests matrix is presented in Table 6-3.

Table 6-3. Tests Programme.

Test number	Material	Strain rate [s^{-1}]	Temperature [ºC]
1	FCS	10	900
2	FCS	0.1	1100
3	Bi-FCS	10	900
4	Bi-FCS	0.1	1100
5	Bi-FCS (surface)	10	900
6	Bi-FCS (surface)	0.1	1100
7	Te-FCS	10	900
8	Te-FCS	0.1	1100

6.5 Results

6.5.1 Mechanical testing

The results of the ductility tests are shown in Figure 6.1. The materials tested had different ductilities but similar hardening characteristics. The Te-FCS is least ductile, then Bi-FCS, followed by FCS, and all material close to the surface is more ductile than the respective centre material. The FCS material is 160% more ductile than the TeFCS. The BiFCS is 23% more ductile than the TeFCS. The reason for these differences was found by analysing micrographs of sections of the materials.

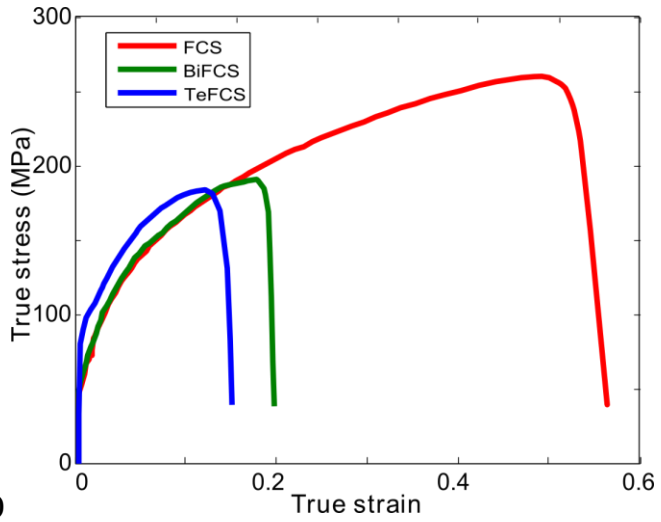

a)

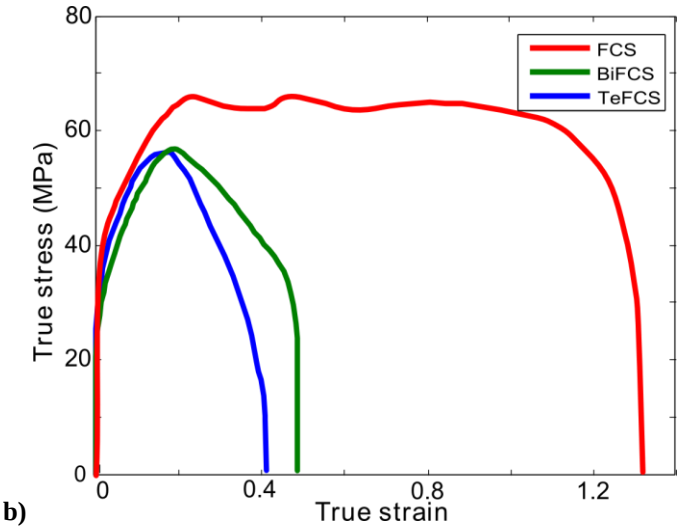

b)

Figure 6.1. True stress strain curves for the a) 'fast and cold' and b) 'slow and hot' tests.

It was identified in Chapter 2 that the inclusions in LFCS often have lead at the inclusion-matrix boundary. This has also been confirmed for the BiFCS using EDX-SEM Figure 6.2. Therefore the same thermally activated damage nucleation is expected. However, this does not explain the difference in ductility, which could be due to different equivalent carbon content, interstitial distributions of additions within the matrix or the volume fraction of inclusions.

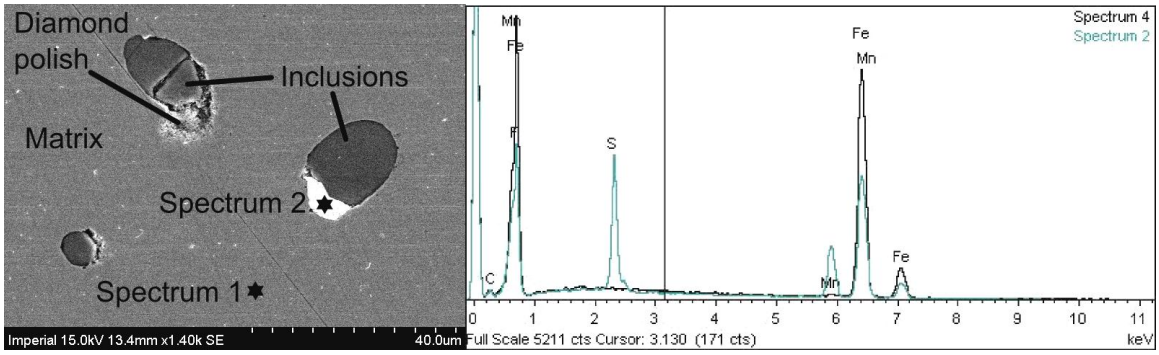

Figure 6.2. Bismuth identified at boundary between inclusion and matrix using EDX.

It may be possible the Bismuth and Tellurium remain dissolved within the matrix. However, an interstitial distribution should have an effect on the hardening rates causing them to differ significantly from that of the FCS, which is not observed, see Figure 6.1.

The difference in ductility is not the only noticeable result. The ultimate tensile strength reached exhibits a comparable trend to that of the ductility. In the high rate tests

the hardening rates are very similar and it appears that the limits of ability to accommodate void growth before coalescence causes the divergence. Therefore, the rate of damage softening increases to its peak before the rate of recovery is equal to that of hardening. This type of trend was noticed for different volume fractions of inclusions in the Chapter 5.

There is expected to be only a small amount of dynamic recrystallisation in the centre material for the ‘slow and hot’ tests, seen in Figure 6.1 (b) at a strain of 0.3 in the plain FCS. Surface material in all steels is more ductile and permits more recrystallisation than the centre material. The fluctuations in the mechanical response caused by recrystallisation are small but noticeable and dynamic recrystalisation could have a significant effect on ductility. However, the surface of the billet cools quickly during the rolling process and may be too cold for significant recrystallisation in the industrial process.

6.5.2 Analysis of micrographs

It is possible to identify damage mechanisms within the samples by looking at the fracture surfaces as well as sections cut perpendicular to the direction of straining. It was feasible to differentiate between grain boundary and plasticity induced damage. In all cases it was possible to identify void growth around inclusions. However, grain boundary damage was harder to identify because due to the cross section being relatively small, see Figure 6.3. However, damage density calculations from micrographs will not be accurate as much of the grain boundary damage is not included in a micrograph section. A micrograph of deformed FCS is presented and annotated in Figure 6.4, which includes several damage mechanisms. Similar damage mechanisms were observed in other free cutting steels, see Figure 6.5. No attempt was made to quantify each type of damage in these samples.

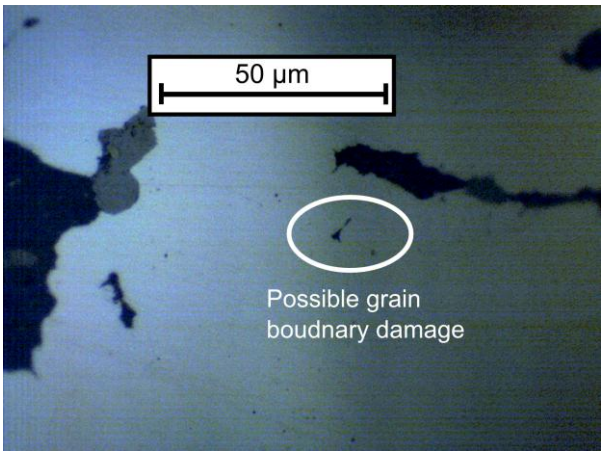

Figure 6.3. Optical micrograph from sectioned uniaxial tensile test showing grain boundary damage, fracture surface on right (BiFCS, T = 1100°C, $\dot{\varepsilon}$ = 0.1 s^{-1}).

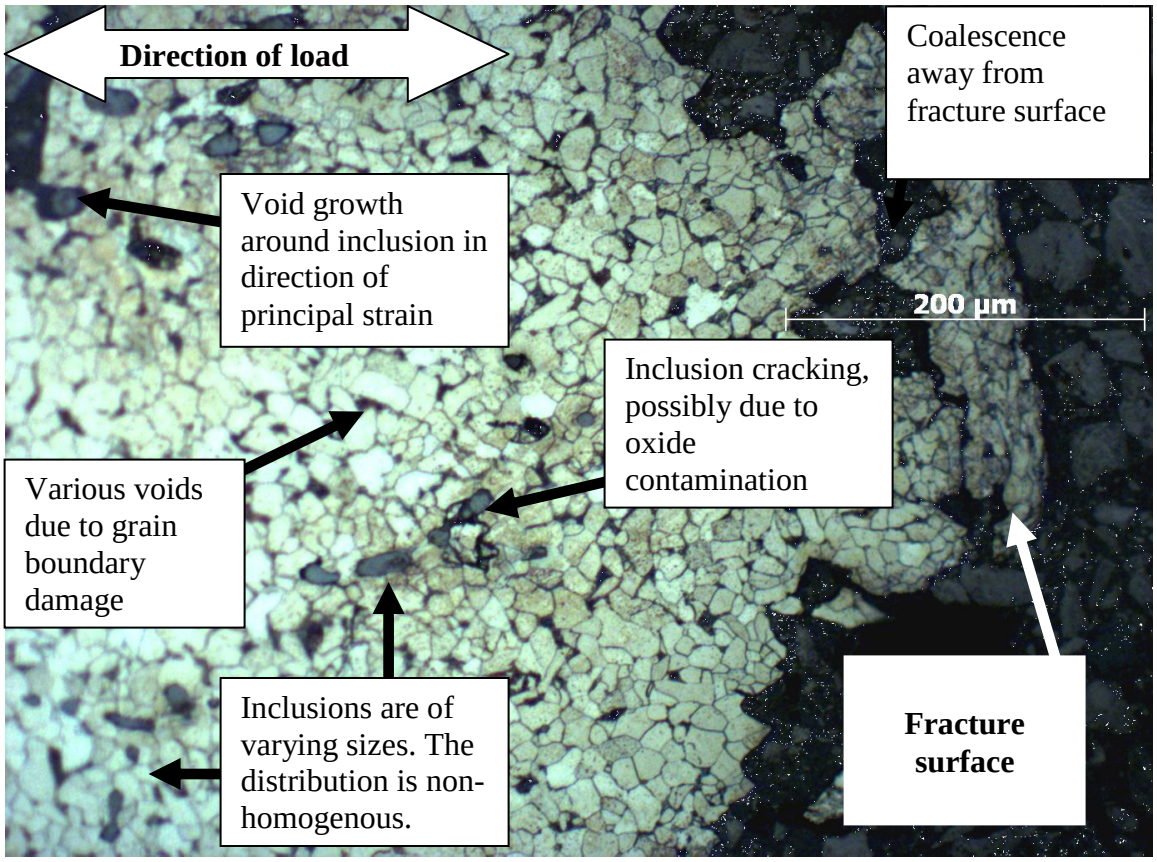

Figure 6.4. Optical micrograph from sectioned uniaxial tensile test-piece with active damage mechanisms identified, fracture surface on right (Free Cutting Steel, T = 1100°C, $\dot{\varepsilon}$ = 0.1 s^{-1}).

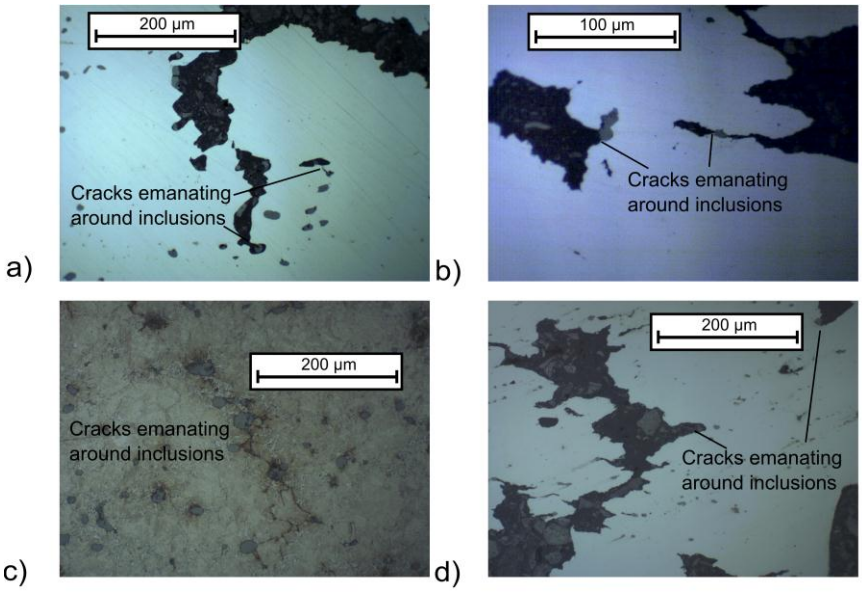

Figure 6.5. Optical micrographs from sectioned uniaxial tensile tests at T = 1100°C, $\dot{\varepsilon}$ = 0.1 s^{-1}, a) BiFCS (sample 1) b) BiFCS (sample 2) c) TeFCS (0.8 ε_f) d) TeFCS.

Grain boundary damage is easier to identify on the fracture surface, as can be seen in Figure 6.6. If the different samples' fracture surfaces are compared there are clear differences as can be seen in Figure 6.7, where the scale of image is decreased down the columns. The FCS has a distinctly smoother fracture surface between the peaks of the voids, which suggests more void growth around inclusions before coalescence. The creep based damage and plasticity-based damage are observable but not quantifiable from the fracture surfaces.

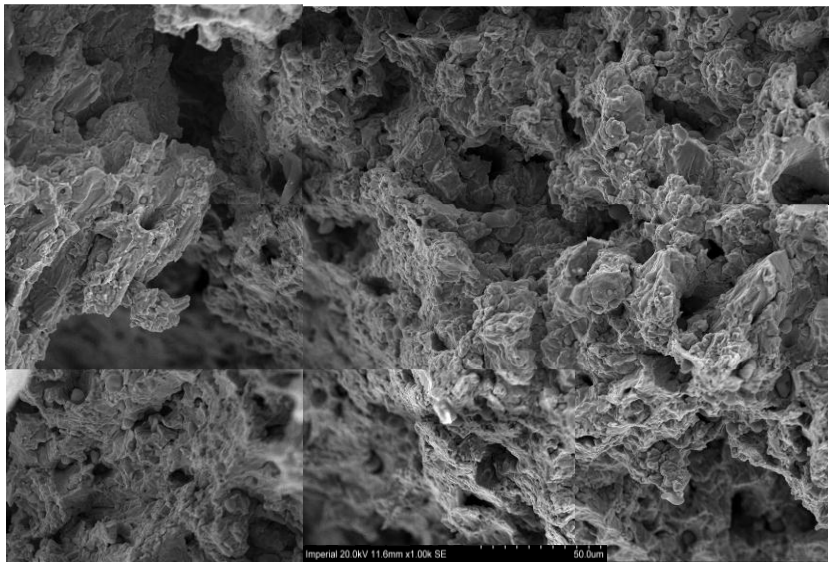

Figure 6.6. Fracture surface of uniaxial tensile test-piece (Bi-FCS, T = 1100°C, $\dot{\varepsilon}$ = 0.1 s^{-1}).

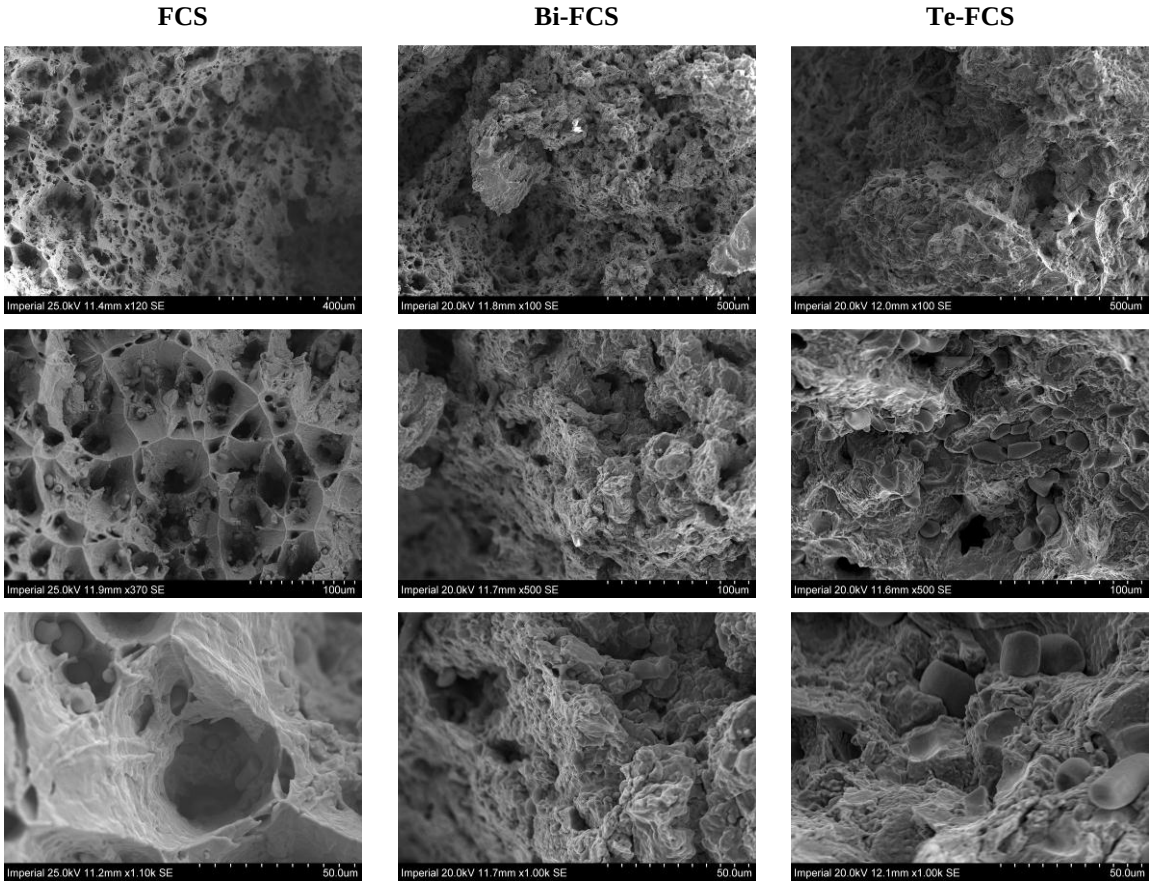

Figure 6.7. Fracture surface of uniaxial tensile test-pieces for various free cutting steels (T = 1100°C, $\dot{\varepsilon}$ = 0.1 s^{-1}).

Another observable damage mechanism was inclusion cracking, as was described in Chapter 4. The inclusions were capable of cracking multiple times as can be seen in Figure 6.8. However, the effect on ductility will be negligible compared to that of void growth around inclusions due to the overnumerousness of intact inclusions. If the fracture surface and micrographs are compared, it is clear that there are more inclusions on the fracture surface than in a flat section. At lower temperatures the fracture surface is peppered with inclusions, which indicates that the crack emanated from inclusion damage sites. The distribution of inclusions were shown to alter the ductility in Chapter 5, where the surface material ductility, or SMD, effect was introduced. The SMD effect was also found in different free cutting steels, as shown in Appendix C.

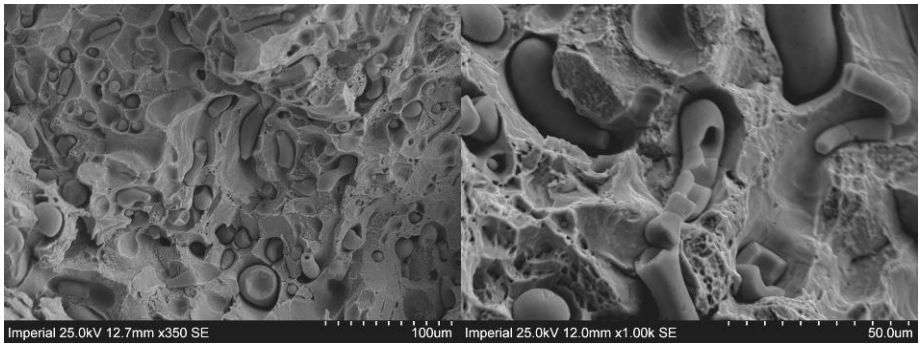

Figure 6.8. Example of inclusion cracking from fracture surface of uniaxial test (Bi-FCS, T = 900 °C, $\dot{\varepsilon}$ = 0.1 s^{-1}).

6.6 Conclusions

The material responses of several free cutting steels' were evaluated through uniaxial tensile tests at different strain rates and temperatures. The results can be used to establish the active mechanisms in each steel and hence identify appropriate damage models to encapsulate the observed damage.

The same mechanisms, of growth of voids and cracks around inclusions, were observed in the different steels but in different proportions related to chemical composition ($\%_{wt}$ Carbon, manganese and sulphide) as well as heavy metal additions. It is clear that the ductility is affected by the changes in chemical composition and this further affects the ultimate tensile strength reached. However, hardening is relatively insignificantly affected compared to ductility. Therefore the same material model could be used with a re-calibrated damage model for the different steels.

Chapter 7 Ex-situ X-ray microtomographic investigation

7.1 Introduction

A brief review of established damage growth theories is presented. Damage quantification techniques are reviewed and *ex-situ* XMT is shown to be the most appropriate technique for high-resolution quantification of damage at high temperatures. Uniaxial tensile samples deformed at 1100 °C and a strain rate of 0.1 s^{-1} were interrupted at various strains. *Ex-situ* synchrotron X-ray microtomography was then used to quantify the nucleation and growth of damage in hot deformation of leaded free cutting steel. Void growth was found to be nucleated at inclusions. The increase in average void diameter with increasing strain is taken to be damage. The number and volume fraction of voids was calculated for each sample. The local strain and stress state, evaluated using the Finite Element Method (FEM), were related to local void populations. The equivalent diameter, spacing and volume fraction of inclusions were measured at different strains. There was evidence that after necking the damage localised due to clustering inclusions. Damage localisation was confirmed with a three-dimensional mircomechanics model of 50 inclusions, whose distribution was taken directly from the XMT results, and a novel approach to extract the damage fraction is presented. A simple term was introduced to account for inclusion size, spacing and clustering, which is validated against the XMT results. The term remains constant throughout the deformation.

7.2 Background

Prior authors have demonstrated that void growth is affected by the presence of inclusions in a variety of materials (Thomason 1990; Horstemeyer and Gokhale 1999; Foster, Dean et al. 2007; Garrison and Wojcieszynski 2007). In these studies, the inclusions were found to either crack along faults or debond from the matrix material. This is the case for LFCS where high-temperature experiments have determined that the dominant damage mechanism is the growth of voids around inclusions (Farrugia 2008; Farrugia 2010). There is a relatively small amount of damage at grain boundaries in the matrix (Foster, Lin et al. 2009). The voids can grow to impingement or a crack can form

between voids in a void sheet mechanism. The ability of the voids to grow is dependent on the forming parameters; given higher temperatures and lower forming rates the matrix can accommodate a greater amount of growth before a crack is formed. It has been proposed that the dislocation density increases near a void, nucleating a crack (Zener 1948). These cracks cross the matrix between the voids creating larger voids and reducing the overall number of voids.

Several attempts have been made to model the effect of inclusions on damage softening. The Rice and Johnson model used a linear relation for the dependence of toughness on the inclusion spacing (Rice and Johnson 1970). The spacing of inclusions was demonstrated to be a significant factor by Weck *et al*., who used precision laser drilled holes to investigate the effect of separation distance of 10 μm holes on damage in aluminium (Weck 2007). More recent models used power law relationships of the volume fraction and average radius of inclusions, which intrinsically includes the spacing (Hahn, Kanninen et al. 1972; Horstemeyer and Gokhale 1999). The effect of the distribution of inclusions in FCS was examined in (Foster, Lin et al. 2006), where the square of the size and the reciprocal square of the spacing were found to best represent their relationship to toughness.

Damage mechanisms can be established by examining micrographs of polished sections of deformed material (Horstemeyer, Lathrop et al. 2000). However, the polishing process is known to fill the smaller voids and this makes it difficult to accurately quantify the damage volume fraction (Babout, Maire et al. 2001). An *in-situ* tensile test of a polished sample using a scanning electron microscope (SEM) avoids this but the surface stress state does not represent the internal stress state.

High resolution synchrotron X-ray tomography allows visualisation and quantification of the damage throughout the microstructure in three dimensions (Phillion, Hamilton et al. 2011). There have been several authors who have taken measurements of the damage in various metals with a second phase (Toda, Sinclair et al. 2004; Maire, Bouaziz et al. 2008; Weck, Wilkinson et al. 2008). Typically these were *in-situ* measurements from uniaxial tensile tests, interrupting the deformation whilst capturing the images. This allows tracking of the progression of individual damage sites. However, until the rate of capture increases during high temperature tests, the interruption allows

the material to recrystallise, which greatly affects damage propagation due to the annihilation of dislocations (Humphreys and Hatherly 1996; Liu 2004). When the amount of damage is quantified, statistical methods are used hence examining individual damage sites is generally redundant. Therefore, conducting the *ex-situ* tests and quenching to freeze the microstructure gives a better statistical representation of damage propagation during straining. An additional benefit of *ex-situ* tomography is that the resolution can be higher than *in-situ* tests. The signal to noise ratio and resolution are proportional to a function of the time available for a scan. The time for each scan is significantly lower during *in-situ* testing due to the static changes that occur at high temperatures. The increased time available for image capture in Ex-situ analysis means that the quality of the data is improved.

X-ray tomography has been used in the calibration of damage constitutive equations by applying several quantification methods (Babout, Maire et al. 2004; Phillion, Lee et al. 2008; Fuloria and Lee 2009). The number of voids can be counted, and the total volume fraction, damage surface area, shape of voids and distance between voids can be recorded. There are several stochastic methods that can be used to account for the change in damage during deformation (Everett and Geltmacher 1999; Phillion, Lee et al. 2008). The fraction of voids located at or near inclusions can be recorded separately, which is useful for understanding the effect of a second phase on damage.

7.3 Experimental methods

The following describes how the material response was found using uniaxial tensile tests and how a series of tests under the same conditions to various strains were conducted. The method of *ex-situ* X-ray tomography analysis using a synchrotron is described.

The material examined is as-cast leaded free cutting steel, which has the chemical composition as shown in Table 4. The casting process is known to leave a variation in size of inclusions, which are smaller closer to the surface (Foster, Lin et al. 2006). To avoid having a variable size, the samples were cut 200 mm from the billet surface within a 52 mm square section.

Table 4. Chemical composition of Leaded Free Cutting Steel

C	Si	Mn	S	Pb
0.07%	0.01%	1%	0.3%	<1%

The tensile tests were conducted using a Gleeble 3800. The test-piece is clamped between two electrically conductive jaws. The temperature is maintained using resistive heating with a feedback loop via a thermocouple, which is welded at the centre of the test-piece. Resistive heating allows precise control of the temperature but localises heating in the centre of the test-piece, which means the effective gauge length depends on the temperature. The gauge length was controlled using a notched sample, which localises the resistive heating due to the smaller cross section. The neck also reduced the effect of the temperature gradient allowing the extremities of the neck to be within 5 % of the control temperature. The notch diameter of 6mm was chosen to ensure the deformed sample fit into the X-ray tomographic field of view (FOV). The test-piece geometry is shown in Figure 7.1.

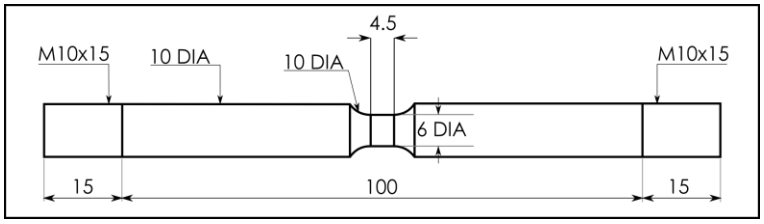

Figure 7.1. Dumb-bell specimen geometry.

The thermal cycle, which is shown in Figure 7.2, was designed to represent the typical reheat used in industrial hot forming operations. A soaking time of four minutes allows homogenisation of the microstructure. Following this, the test-piece was cooled to the test temperature of 1100 °C at which the test-piece was deformed. The displacement of the actuator was controlled to maintain a constant strain rate of 0.1 s^{-1}. A C-gauge was employed to record the diameter at the notch throughout the test in accordance with (DSI 2011). The change in diameter was used to calculate the true strain. Several tests were conducted to failure to confirm the mechanical response and required displacement for particular strains.

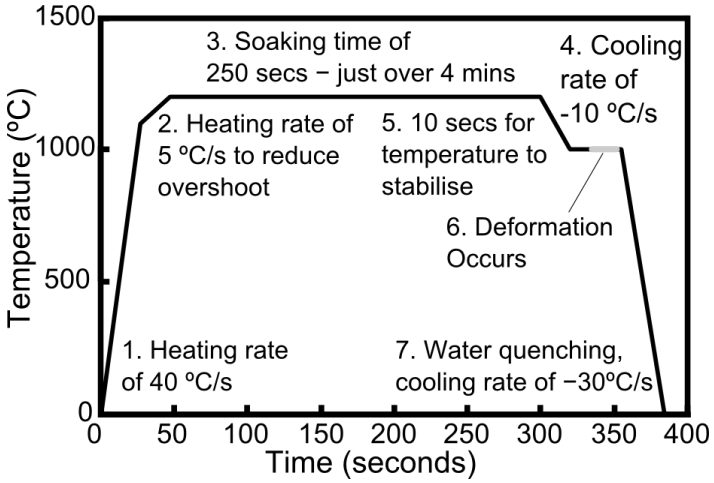

Figure 7.2. Thermal profile of test-piece.

The objective of this investigation was to examine the progression of damage, therefore two strains (ε = 0.33 and 0.38) after necking were analysed in different test-pieces by interrupting the test before failure. Immediately after the deformation was stopped, the material was quenched in water, which froze the microstructure. To ensure that the water made full contact with the specimen, the C-gauge was not used in the interrupted tests. The displacements of the actuator for the required strains were determined based on prior tests to failure. Applying a zero-force condition allowed the test-piece to cool with no further plastic deformation. The tests were then run under the same thermal profile and strain rate as the tests to failure but were stopped at the required displacements.

As the test-pieces are axisymmetric, only a section of the test-piece needs to be studied. The test-pieces were sectioned down the length. Two halves of different test-pieces were placed together for examination using ex-situ X-ray synchrotron tomography. The X-ray synchrotron tomography experiments were conducted at I12 – JEEP (Joint Engineering, Environmental and Processing) beamline, Diamond Light Source, UK. Full details on the tests are shown in Appendix B. The monochromatic X-ray beams (~76.5 keV) were applied through the specimens while they were continually rotating over 180 degrees. A series of 1441 projections were taken at one-second exposure times during the scan, resulting in the full set of data required for reconstructing a 3D volume. A high-

resolution camera was used to acquire images with the FOV of 7.2 × 4.8 mm (4008 × 2672 pixels) and at the spatial resolution of 1.8 μm/voxel. Dark-field images and flat-field images were also produced in order to improve the quality of the reconstructed images. The in-house reconstruction software, VT-reconstruction, based on the Filtered Back Projection (FBP) method was then performed to get a 3D volume of each specimen (Titarenko, Titarenko et al. 2010).

The sectioned test-pieces were also analysed using an optical microscope. After the test-pieces had been examined using X-ray synchrotron tomography, the samples were mounted in Bakelite and polished to a one-micron finish. Micrographs were made using 100 times magnification on a Compaq microscope fitted with an AxioVision camera. The images were concatenated to produce a composite image with a minimum of 500 inclusions, which is considered to be statistically significant.

The microstructural damage (inclusions and voids) at different strain levels, both in the bulk and local volume near the gauge centre, were quantified from X-ray synchrotron tomography and compared to FEA results. Firstly, a non-linear diffusion filter was applied to the reconstructed data in order to reduce the noise. The data were then thresholded to obtain the binary data of microstructural damage. The cubic volumes of 3000 × 2000 × 900 μm^3 at the centre of the gauge were cropped and analysed to represent the damage deformation behaviour of the bulk of each sample. The isosurface reconstruction of each connected damage site was triangulated via a Marching Cube Algorithm, which was then used to calculate the volume and the surface area of each inclusion/damage (Lorensen and Cline 1987). The orientation of inclusions/damage compared to the loading direction was also taken into account. The Principal Component Analysis (PCA) method, which is described in (Puncreobutr, Lee et al. 2012), was applied to indicate the preferred growth direction of voids, compared to the loading direction (i.e. 0 and 90 degrees represent parallel and perpendicular orientations, respectively).

For the sub-volume analysis, the hemicylindrical volumes of 1000 μm diameter and 1000 μm length at the centre of the sample gauge were selected. The damage in these regions was quantified. The increase in size of voids led to large voids intersecting the boundary of the analysed region, which would lead to their exclusion from the analysis.

To avoid this problem, the buffer zone method was implemented. Firstly, the centroids of all inclusions/voids in the cubic bulk volume were calculated. For every inclusion/damage that had its centroid located inside the hemicylindrical sub-volume, the measurement (e.g. volume, surface area, orientation) was conducted not only inside the hemicylindrical sub-volume, but also within the buffer zone. The buffer zone is generated as a hemicylindrical shape from the sub-volume, but its size is expanded by the mean diameter of all inclusions/voids in the bulk volume. Using this method, fewer inclusions/voids will be cut off and the results are much more statistically acceptable.

7.4 Results

The mechanical responses of the interrupted tests can be seen in Figure 7.3. The interrupt strains were taken from the point at which the displacement was stopped. The strain due to the change in temperature during quenching was ignored.

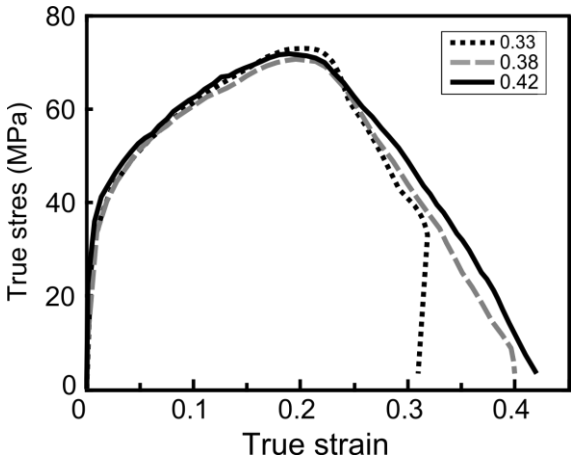

Figure 7.3. True stress versus true strain curves for a specimen strained to failure and specimens strained to: 0.33 and 0.38.

Optical micrographs of the test-pieces at the different strain levels show that inclusions elongated but not all the inclusions deformed. There is progressively more damage after a strain of 0.33, as seen in the optical micrographs of Figure 7.4 (a) (each column represents a level of strain; i, ii and iii for 0, 0.33 and 0.38 respectively). The micrographs highlight the presence of damage but identifying damage mechanisms usually requires other methods. The areas under question were examined using a SEM. The type of damage found in the different samples varied, as can be seen in Figure 7.4

(b). The inclusions are initially globular and, as described earlier, some have lead at their surfaces (see Figure 7.4 (b) i). There is as-cast porosity in the test material, which is identified by the relatively smooth surface of the void (see Figure 7.4 (b) ii). As the strain reached 0.33, there was visible coalesced damage, as shown in Figure 7.4 (b) iii. It was confirmed that this is not as-cast porosity due to the rough surface of the pore, which suggests transgranular cracking. This can be compared to the results from X-ray synchrotron tomography, which show that there is significant damage within the material. In column iii, close to failure, the voids have coalesced into a large void in the centre of the test-piece. There are inclusions on the surface of the coalesced void, which indicates that voids grew around the inclusions. There is a varied roughness of the fracture surface, which indicates a combination of intergranular and transgranular damage. However, it is possible that there is a combination of transgranular damage and porosity.

The X-ray synchrotron tomography produced both 2D longitudinal micrographs (Figure 7.4 (c)) and 3D reconstructed images (Figure 7.4 (d)). The threshold of smallest inclusion diameter that could be verified in this experiment was 2 μm. The smallest visible inclusions using SEM were found to be 1 μm. However, from the SEM measurements of the virgin material, inclusions smaller than 10 μm were lower than the 3rd percentile and were statistically insignificant. The difference between void and inclusion is not possible to discern due to their relative attenuation of X-rays, compared to the steel matrix. Therefore, the volume of inclusions and voids in the microstructure were combined as the microstructural damage. The progress of void growth and coalescence at different strain levels is highlighted by assuming that the virgin material has no void growth and any increase in average inclusion radius at larger strains is void growth. The difference in volume of the inclusions at the larger strains compared to the virgin material is highlighted as damage. The 3D reconstructed damage (inclusions and voids) from X-ray synchrotron tomography is shown in Figure 7.4 (d).

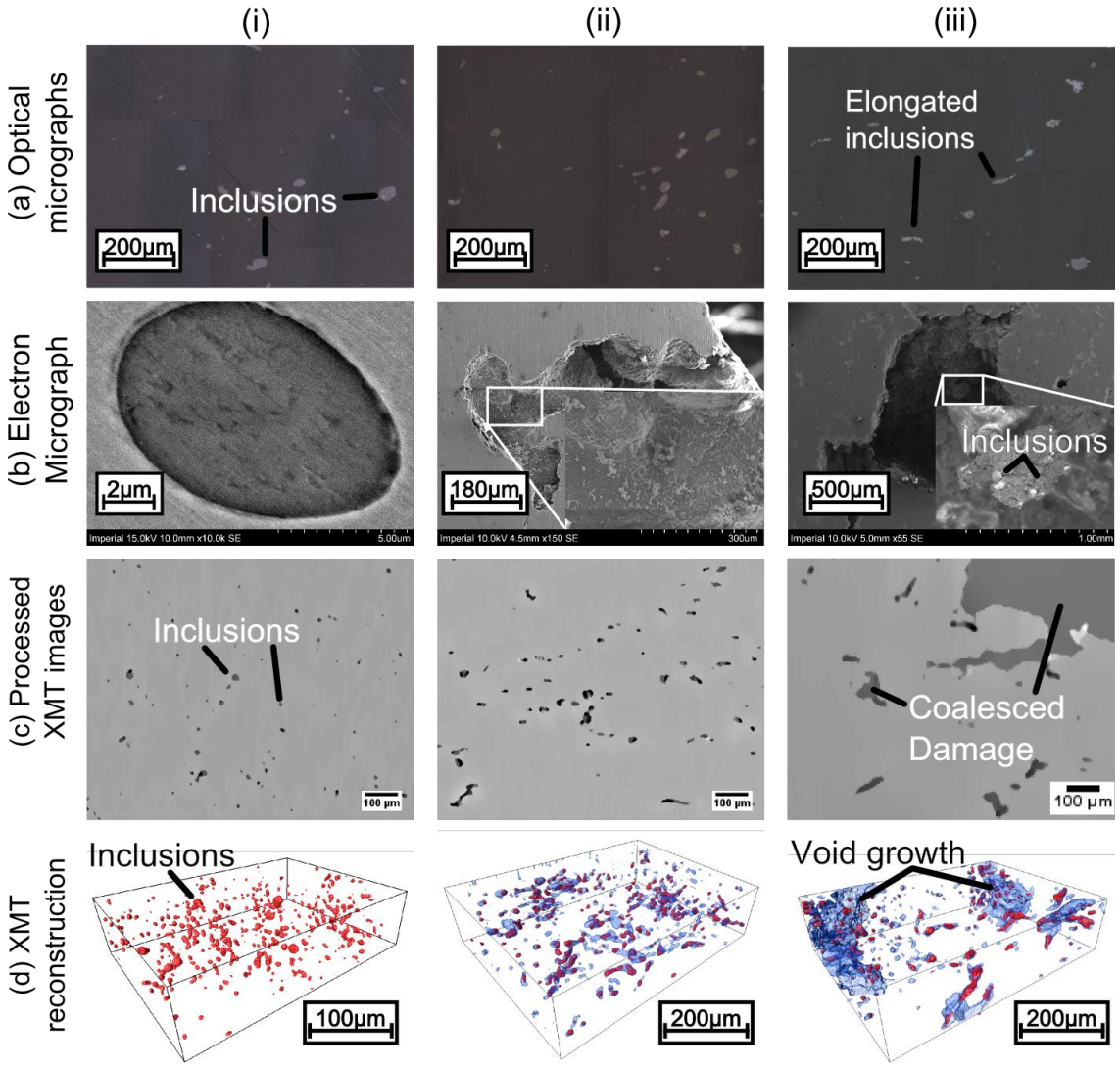

Figure 7.4. Visualisation of the inclusions in a) optical micrographs b) SEM c) longitudinal micrographs from X-ray tomography and d) 3D images from X-ray tomography, where i, ii and iii represent strains of 0, 0.33 and 0.42 respectively.

The images in Figure 7.4 (d) are useful for qualitative inspection of the void growth. It was also necessary to quantify the distributions of damage growth in each sample. The specimen is uniaxial but the local stress and strain within the specimen is not homogeneous: this needed to be considered for the quantification of inclusion distributions. A finite element model was built to establish the local stress state. A 4-node thermally-coupled axisymmetric quadrilateral, bilinear displacement and temperature mesh was used with reduced integration and hourglass control. A material model for

leaded free-cutting steels, LFCS, was implemented using an ABAQUS Variable User MATerial, *VUMAT*, subroutine for explicit calculations (Foster 2007). The model is a physically-based, temperature-dependent set of constitutive equations, which is fully described in Chapter 8.

The minimum mesh density was 5 elements per mm^2. However, higher densities were used in areas of stress concentration. Temperature was defined based on measured values in testing, and the defined temperatures are shown in Figure 7.5. Boundary conditions of axisymmetry were used in the vertical direction, and symmetry in the horizontal plane and the centre of the notch. The deformation uses the same displacement control as that in the experiments. The distribution of strain in the model is shown in Figure 7.5. There is a range of strain at different points in the neck. However, a square area of 1.2 × 1.2 mm^2 has a range in strain less than 10% of the average.

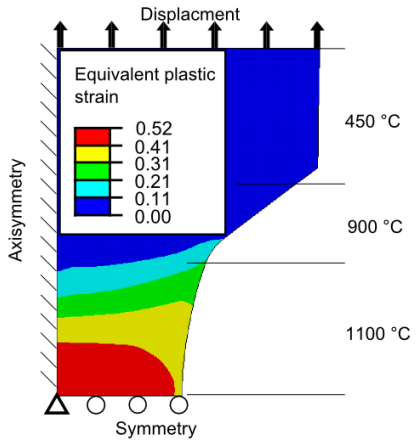

Figure 7.5. Modelled strain distribution in the test-piece.

During the deformation inclusions elongate and the voids grow at the inclusion's boundary to the matrix in the direction of the applied stress. Since the number of inclusions were different in the volumes analysed it was necessary to normalise the distribution. The volume fraction was calculated using Equation 7-1, where V_i is the volume of the i^{th} void and V_{norm} is the normalised volume fraction. The normalised volume fraction is plotted against equivalent damage diameters at various strains in Figure 7.6. The strain of 0.38 has large volumes of coalesced damage, which are two orders of magnitude larger than the voids. This coalesced damage is the separation of the

two ends of the test piece. The large void volumes of coalesced damage were removed from the analysis as they did not represent void growth and it allowed comparison of the voids at each strain to be made. The mode diameter in the virgin sample is 11 μm. The mode diameter does not change significantly after necking. Therefore, the majority of inclusions are not associated with much damage growth. As the straining progresses more inclusions have associated localized damage growth. The increasing stress localization leads to coalescence.

$$V_{norm} = \frac{V_i}{\sum_{i=1}^{N} V_i}$$ **Equation 7-1**

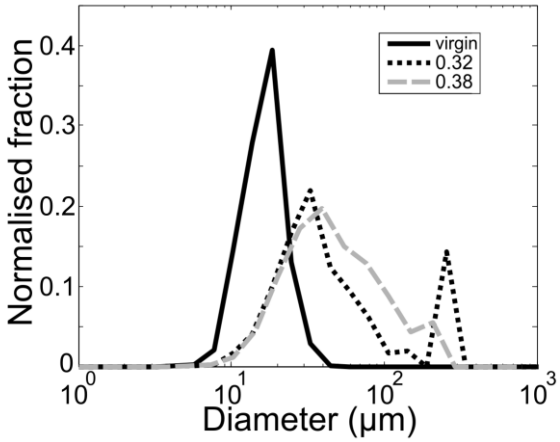

Figure 7.6. Comparing the average equivalent void diameter evolution during straining.

There are two distinct spatial distribution measurements for the inclusions; the spacing and the nearest neighbour. The nearest neighbour, *ƗO*, is the shortest distance from each inclusion to another inclusion. The spacing, *L*, is a statistical average of the distance from each inclusion to those inclusions that are near it. The *L* will always be a slightly greater value than *ƗO* and is a more robust figure in describing the distribution. *ƗO* will have a greater effect on the stress localisation between inclusions, which will affect the initiation of damage coalescence.

A Delaunay triangulation algorithm was used to calculate the vectors between inclusion centres from the XMT data. The line segments of the triangles formed are the vectors of the nearest neighbour. The results for spacing and nearest neighbour at different strains are shown in Figure 7.7(a) and (b), respectively. The mode nearest

neighbour in the virgin sample is 12 μm and increases by 20% to 14.5 μm at a strain of 0.33. This is due to the voids forming at inclusions, which increases the volume of the sample, despite the constant volume of the matrix. The increase in spacing, up to a strain of 0.33, is representative of damage formed prior to coalescence. After coalescence the inclusions with the largest associated voids will have agglomerated. Therefore, the remaining inclusions are those associated with less damage and are closer together. This causes a decrease in inclusion spacing at a strain 0.38.

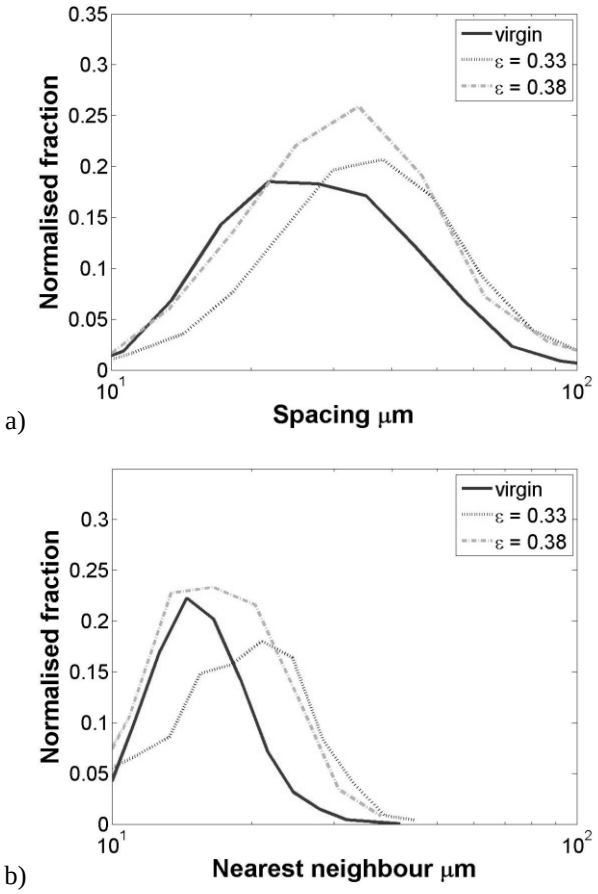

Figure 7.7. Distribution of inclusions at different strains a) spacing b) nearest neighbour.

The size and spacing distributions have been used by other researchers to create parameter combinations that are included in constitutive equations; one is shown in Equation 7-2, where *s* is a constant, originally given a value of 2 (Foster, Lin et al. 2006). The average of the measurements was taken in (Foster, Lin et al. 2006) for the nearest neighbour, *IO,* and diameter, *D*, of the inclusions. Using this method a larger inclusion very close to another inclusion would be lost in the statistics. It is more relevant to

calculate the ratio of the diameter to the nearest neighbour of each inclusion and use the mode of these results. However, by using the mode of IO and D to calculate ω for the virgin material gives a value of 0.143. The individual ω for each inclusion is denoted ω_i and named the inclusion distribution factor. The individual ω for each inclusion, using the spacing instead of the nearest neighbour is denoted ω_s. The distributions of ω_s *and* ω_i are shown in Figure 7.8(a) and (b), respectively. Calculating ω_i for each inclusion gives a similar distribution to that of ω_s, but with a mode of 0.367. The distribution of ω_i was measured at different interrupt strains and was found to be roughly constant throughout deformation. This suggests that the increase in diameter is counterbalanced by the increase in nearest neighbour, as they increase proportionally due to damage growth.

$$\omega_i = \left(\frac{D}{IO} \right)^s \qquad \textbf{Equation 7-2}$$

The terms described are useful for assessing the distribution of inclusions in different locations in the as-cast billet. However, they do not account for clustering of inclusions. Clustering is known to affect the interactions of stress discontinuities associated with inclusions (Huang, Chandra et al. 1998). The amount that inclusions interact affects the damage rates (Argon, Im et al. 1975). Being able to predict clustering can improve the accuracy of damage models (Kaye, Balint et al. 2010). The size and nearest neighbour of inclusions in LFCS is represented by ω_i, which is distributed as shown in Figure 7.8(b). For a homogenous size and spacing, there would be no distribution. However, as the variance in spacing increases, so does clustering. Clustering can be included in a constitutive model using the value of mean of ω_i plus three standard deviations, which is 1.87. This aspect of the distribution could be included in damage models to account for clustering.

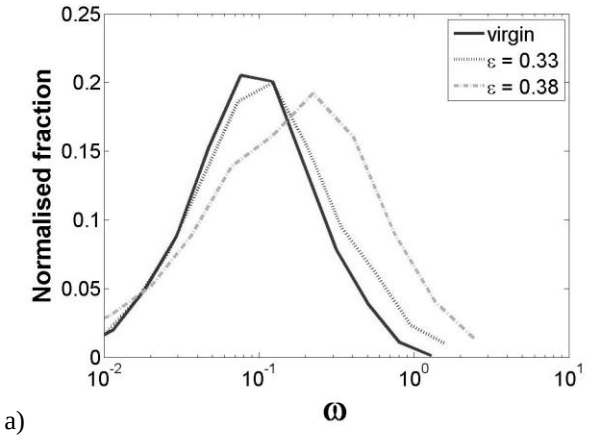

a)

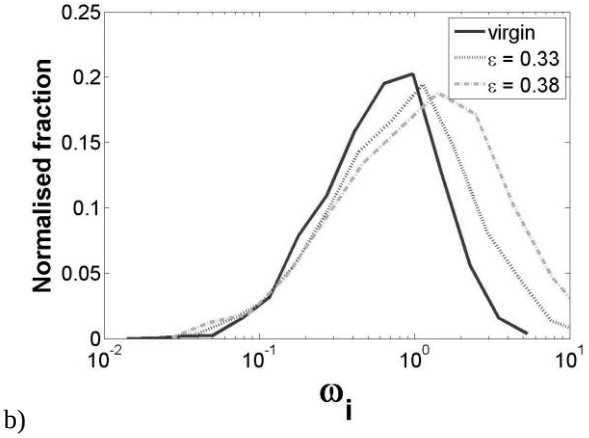

b)

Figure 7.8. Distribution of a) ω and b) ω_i at several strains.

7.5 Microstructural modelling

A model was generated to confirm the theories described regarding the effect of inclusion distribution on the local stress state and damage. The locations and sizes of inclusions were imported from XMT results of the virgin material into a 3D finite element simulation. It was assumed that the inclusions were spherical. The observed variation in distribution of size and nearest neighbour of inclusions was accommodated by breaking the XMT volume into 200 μm cubes: ω_i was calculated for each cube and the cube with the closest average ω_i to the mode of the population was chosen. This allowed a more representative simulation of the physical results. A buffer volume, at least 100 μm in thickness, was included around the cube of inclusions. A limit of 100 inclusions was chosen to reduce the computational expense.

The model used the displacement of nodes from a global model of the uniaxial tensile test to define its displacement boundary conditions and is therefore defined as a submodel. The matrix material used the same material model as described previously. The inclusions were modelled as purely elastic with Young's modulus and hardness properties 1.6 times those of the matrix. It is clear that under a tensile stress state, straining causes some amount of void growth around inclusions. The effect of triaxiality is to exponentially increase the rate of damage growth and coalescence (Gurson 1977). There is a range of stress triaxiality within a necking tensile sample (Mirone 2007). More robust investigations have been performed on the different locations within a neck (Maire, Bouaziz et al. 2008). This effect was not investigated further, but was considered for the locations of the nodes driving the submodel, which were taken from close to the centre of the uniaxial global model, see Figure 7.9. The pale square represents a cross section taken half way into the cube; the inclusions are visible in the centre of this cross section.

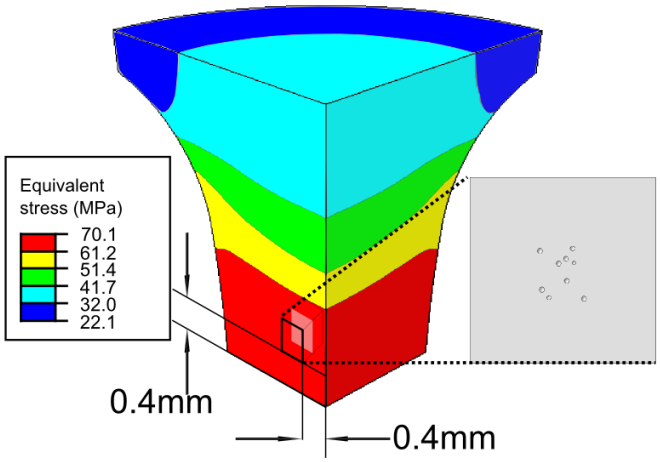

Figure 7.9. Location of submodel within global model.

The submodel results make evident that there are localised stresses around inclusions. By removing all elements with a stress below 82 MPa it was possible to visualise the stress localisation, see Figure 7.10. The stress in the matrix away from inclusions was 73 MPa. The higher stress appears around the inclusions in a plane perpendicular to the applied load. More importantly there is stress localisation between inclusions in three dimensions, especially for those that are closer together.

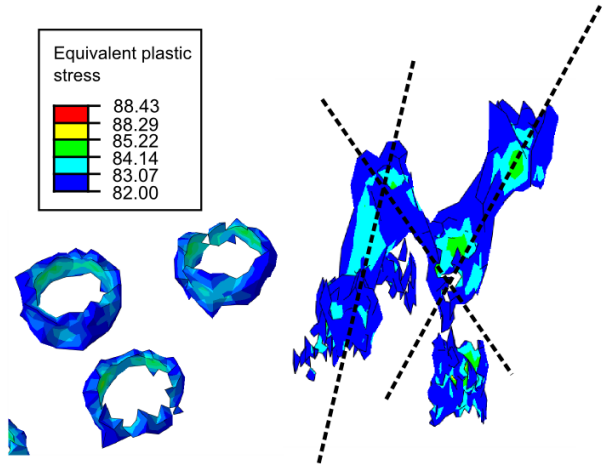

Figure 7.10. a) Stress localisation around inclusions, elements with stress below 82 MPa are hidden, b) Interaction of stress fields around inclusions in several directions.

The volume of the elements that had a damage of 1 was recorded in each step. The sum of the volumes of damaged elements was divided by the final volume fraction of damage to get a normalised damage. This damage fraction from the submodel is compared to the damage fraction recorded from XMT in Figure 7.11. The damage from the global FE model, averaged from the volume in the same position as the submodel, is also plotted. The values of damage fraction are different but the exponential increase in damage fraction occurs at a similar strain. The modelled damage shows an accelerated increase at the same strain as the XMT results and shows a matching exponential trend, which verifies the models. The lower strain to localisation will be due to the inclusion factor included in the matrix material model.

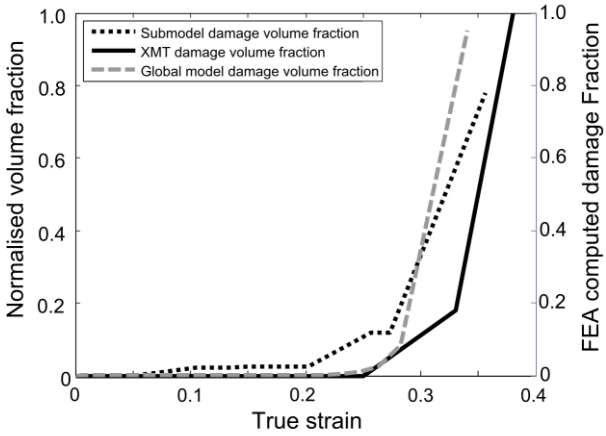

Figure 7.11. The evolution of damage in sample compared to FE model.

The submodel was adapted to model a uniform distribution of inclusions. A parametric study, using the micrsotructural sub-model, was used to investigate the effect of spacing of inclusions on stress localisation and damage growth. Two distributions were considered; where the inclusions are aligned so that the nearest neighbour is perpendicular to the direction of the applied load and another where it is aligned diagonally to the applied load. The matrix and individual inclusions can be considered as two separate continua, therefore the inclusions are scalable within the matrix. The diameter of the inclusions was kept constant, at 10 μm, and the spacing was altered in each simulation. The matrix was deformed until localisation of damage occurred, example distributions are shown in Figure 7.12. It is believed that the localisation of void growth is due to the interacting concentration of stresses around inclusions.

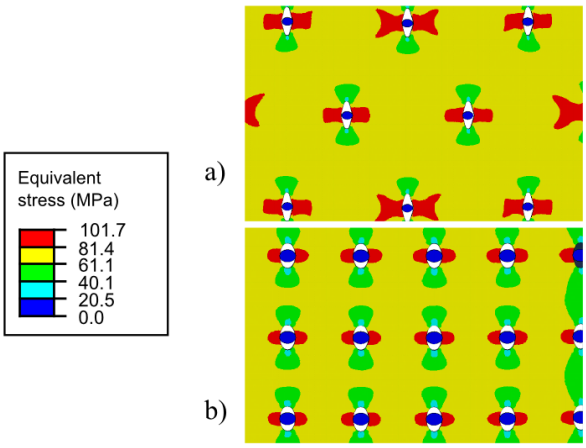

Figure 7.12. Localization of stress around inclusions: a) diagonally spaced, b) evenly spaced.

Localisation was defined as the point that the void growth no longer has a linear relationship to strain. The normalised void size was calculated by removing the inclusion area from the void area and dividing by the original void area. Initially the void growth had a linear relationship to strain but when localisation occurred, the rate of void growth was accelerated as shown in Figure 7.13.

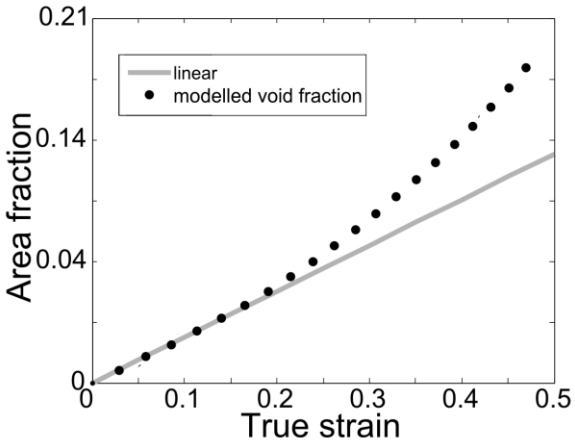

Figure 7.13. Void area fraction during deformation for a diameter-to-nearest neighbour ratio of 0.4.

The strain to localisation of void growth, ε_{loc}, was plotted against the diameter-to-nearest neighbour ratio as shown in Figure 7.14. The measured diameter-to-nearest neighbour ratio is included in the plot, and is close to the modelled results. When the spacing was ten times the diameter, there was no interaction between the inclusions and the void growth failed to localise.

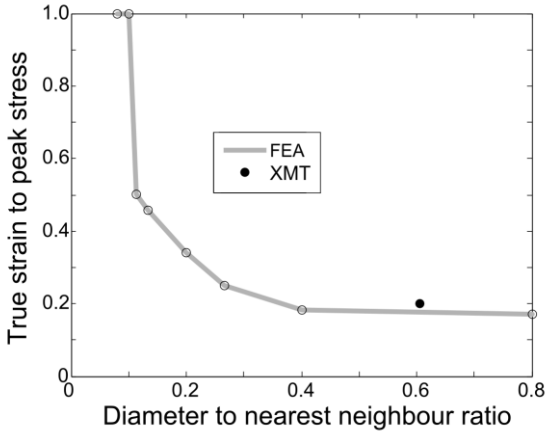

Figure 7.14. Strain to peak stress against the diameter-to-nearest neighbour ratio.

The size and spacing of inclusions is understood to affect the ductility. This was modelled in Equation 7-2, but the exponent, *s*, is yet to be properly evaluated. The microstructural model makes it possible to define a value for *s*. The strain to localisation of void growth was established by comparing the size of voids in each time step relative to their initial size. Void growth is linear with strain until localisation occurs (Maire,

Buffiere et al. 2001; Pardoen 2006), which is expressed in Equation 7-3, where k is a function of the stress state, strain rate and temperature but can be treated as a constant for each test under the conditions of uniaxial tension, a single temperature and a single strain rate. Equation 7-3 can be rearranged in terms of ω and set equal to Equation 7-2, as shown in Equation 7-4. As the rate of damage growth is constant, up to the strain of damage localisation for each distribution of inclusions, then this rate can be calculated from Equation 7-5. By taking logarithms of Equation 7-4, and applying Equation 7-5, the equation can then be rearranged in terms of s to create Equation 7-6.

$$\dot{D}_G = \omega \dot{k} \qquad \textbf{Equation 7-3}$$

$$\omega = \frac{\dot{D}_G}{\dot{k}} = \left(\frac{D}{IO} \right)^s \qquad \textbf{Equation 7-4}$$

$$\dot{D}_G = \frac{D_G^{loc}}{\varepsilon_{loc}} \qquad \textbf{Equation 7-5}$$

$$s = \frac{\ln \left| \frac{D_G^{loc}}{\varepsilon_{loc} \dot{k}} \right|}{\ln \left| \frac{D}{IO} \right|} \qquad \textbf{Equation 7-6}$$

All the terms in Equation 7-6 are either specified for the simulations or can be calculated from the results of the simulations, apart from k and s. The two unknown terms, k and s, can be determined through trial and error using Equation 7-6 and the values of the terms from two or more simulations with different distributions of inclusions. By altering the value for k it was possible to determine a value for s that was the same for all the different values of nearest neighbour. The value of s is determined to be 0.9. This value is within the range of values used in (Foster, Lin et al. 2006; Garrison and Wojcieszynski 2007).

7.6 Conclusions

Synchrotron x-ray tomography is a useful tool for the investigation into almost any material's microstructure. The inclusion diameter and spacing in steel were measured using *ex-situ* synchrotron x-ray microtomography, XMT, and are found to be distributed

with modes of 11 μm and 12 μm respectively. During hot deformation the mode of the spacing and equivalent diameter of inclusions increases until localisation of damage growth occurs leading to necking. After necking a minority of inclusions have further localised damage growth until coalescence between growth sites occurs. The cause of this localisation is the stress concentration caused by proximity and size of inclusions. The size and proximity of inclusions is accounted for by a measurable term. The term can also be used to account for clustering of inclusions, which is a significant factor on coalescence. Three dimensional simulations were used to highlight the stress localisations between inclusions. The models were verified against the XMT results and used to determine the effects of different uniform distributions of inclusions on damage. There is a limit of diameter to spacing of 0.1, below which the inclusions do not interact. The microstructural models permitted calibration of the inclusion distribution factor.

Chapter 8 Unified viscoplastic damage equations

8.1 Introduction

Based on the experimentally observed results, a mechanistic model has been developed to predict deformation and damage features during hot forming of steel within the strain rate range of 0.1 s^{-1} to 10 s^{-1} and deformation temperature range of 900 °C to 1100 °C. The model is generally applicable to a range of metal alloys experiencing grain-boundary and plasticity-induced damage associated with inclusions or precipitates under hot forming conditions. This chapter describes the modelling approach to encapsulate the experimental results described in Chapters 3 to 7. The computationally derived stress-strain relationships are presented and fitted with experimental results for the relevant strain rate and temperature range.

Several damage models were described in Chapter 3, some of which were based on a single mechanism to account for the softening due to void growth. The limitations of these models for use in hot forming of steel, due to the assumptions, were described in Chapter 3 and are not reviewed again here. The more sophisticated models, which include multiple mechanisms, can take into account the interplay of different key microstructural features, such as grain size, dislocation density, and precipitate volume fraction and size. This increases the accuracy of the model within the range of parameters where the mechanisms occur.

8.2 Theory of decomposition

8.2.1 Associated flow rule.

The strain, ε_T, can be partitioned into viscoplastic and elastic (reversible) components given subscript *p* and *e*, respectively:

$$\varepsilon_T = \varepsilon_p + \varepsilon_e \qquad \textbf{Equation 8-1}$$

Hooke's law can be used to calculate the stress, σ, using the Young's modulus, *E*, and the elastic strain:

$$\sigma = E\varepsilon_e$$ **Equation 8-2**

The Young's modulus is difficult to measure at high temperatures due to viscoplastic effects. As was seen in the results of previous Chapters (Figure 6.1) the high-temperature response shows no initial linearity and there is a relatively low yield stress. Equation 8-3 has been modified to better calculate the Young's modulus; where α (with units of 1/°C) is a constant and E_0 is a value of Young's modulus measured at a reference temperature, T_0 (Liu 2004).

$$E = \frac{E_0}{\cosh\left(\alpha\left(T - T_0\right)\right)^2}$$ **Equation 8-3**

8.2.2 Flow rule

A flow rule is used to relate the stress to plastic strain rate, $\dot{\varepsilon}_p$. Classical strain hardening rules can be combined with the equation by Norton, see Equation 8-4, where λ is a constant and n is the stress exponent (Norton 1929). This approach has been used by Lemaitre, and Lin, amongst others, to form Equation 8-5, where K is the drag stress (Lemaitre and Chaboche 1990; Lin, Liu et al. 2005). Equation 8-5 can be rearranged to form Equation 8-6, which can be used for simple models. However, softening phenomena are not included and yield is ignored, which has been empirically demonstrated to be inaccurate in previous chapters (see Appendix C).

$$\sigma = \lambda\dot{\varepsilon}_p^{1/n}$$ **Equation 8-4**

$$\sigma = K\dot{\varepsilon}_p^{1/n}\varepsilon_p^{1/m}$$ **Equation 8-5**

$$\dot{\varepsilon}_p = \left(\frac{\sigma\varepsilon_p^m}{K}\right)^n$$ **Equation 8-6**

By replacing the hardening rule with more appropriate and versatile hardening rules the applicable range of the equation is increased. Isotropic hardening laws have been applied to create Equation 8-7, κ is the yield stress and *H* is dislocation hardening (Lemaitre and Chaboche 1990; Lin, Liu et al. 2005). This approach has been applied to the rolling process (Foster 2007).

$$\dot{\varepsilon}_p = \left(\frac{\sigma - \kappa - H}{K} \right)^n \qquad \textbf{Equation 8-7}$$

The hardening exponent, *n*, and the dynamic yield point, κ, decrease with temperature (Dunne 1996). Parameters that are temperature-dependent can be accounted for using an exponential relation similar to that shown in Equation 8-8 where *R* is the gas constant and *T* is the temperature; it is similar to the Arrhenius equation. The values for *Q*, the activation energy, and material constant, κ_0, have to be determined.

$$\kappa = \kappa_0 \exp\left(\frac{-Q_k}{RT} \right) \qquad \textbf{Equation 8-8}$$

8.2.3 Hardening rule

Dislocation annihilation and dislocation accumulation dictate the macroscopic mechanical behaviour and microstructural evolution of any material. The mobility of dislocations is typically impeded by obstacles including other dislocations, grain boundaries and precipitates (Frost and Ashby 1969). The increase in flow stress that is required to facilitate the movement of dislocations through and around one another is known as strain hardening or work hardening.

Work hardening, *H*, is due to the immobilisation of dislocations (Kocks and Mecking 2003). It has been studied by many authors and is still not fully understood due to the varying complexities. The value for *H* is calculated based on a series of measurable variables and empirical studies. The energy required for dislocation slip is proportional to mean free path, *L*, which is the distance a dislocation can travel before it encounters a barrier. As the dislocation density increases, the mean free path decreases and the

mechanical strength increases. The work by Taylor demonstrated that the mean free path is proportional to the inverse of the square root of the dislocation density (Taylor 1938).

The dislocation density, ρ, ranges between the fully annealed state, ρ_0, which is the original dislocation density, and ρ_{max}, which is a fully saturated network. The normalised dislocation density, $\bar{\rho}$, can be calculated from Equation 8-9. The normalised dislocation density ranges between zero and one, for a fully annealed and fully saturated matrix, respectively.

$$\bar{\rho} = \frac{\rho - \rho_0}{\rho_{max} - \rho_0} \qquad \textbf{Equation 8-9}$$

The mechanical strength of obstacles to dislocation slip, $\hat{\sigma}$, is calculated using Equation 8-10, where α is a constant, G is the shear modulus, b is the Burger's vector and $\bar{\rho}$ is the normalised dislocation density (Estrin, Toth et al. 1998). The only parameter that alters for a particular material during deformation in this equation is the dislocation density. The other terms can be collected into a single temperature-dependent constant, B.

$$\hat{\sigma} = \alpha G b \sqrt{\bar{\rho}} \qquad \textbf{Equation 8-10}$$

$$H = B\sqrt{\bar{\rho}} \qquad \textbf{Equation 8-11}$$

Equation 8-12 was based on work by Kocks and Mecking and altered by Estrin to include the strain (Estrin, Toth et al. 1998; Kocks and Mecking 2003). Several authors have followed a similar method, whilst assuming no dynamic recovery, using Estrin's equation to form Equation 8-13, where k_1 is a constant, which can be used to evaluate the dislocation density rate.

$$\frac{\partial \bar{\rho}}{\partial \varepsilon_p} = \frac{M}{bL} \qquad \textbf{Equation 8-12}$$

$$\dot{\bar{\rho}} = k_1\left(1 - \sqrt{\bar{\rho}}\right)\dot{\varepsilon}_p \qquad \textbf{Equation 8-13}$$

If two dislocations have opposite signs and are on the same slip plane, they attract one another, and will annihilate each other when they meet (Ashby, 1983). This process is known as recovery and it is a softening mechanism. At high temperatures, the effect of the recovery mechanisms on the material microstructure is relatively high (Carrick, 2009). An equation for the static recovery was derived in the form of Equation 8-14. This equation was simplified by Lin et al. to form Equation 8-15, where c_1 is a temperature-dependent constant described in Equation 8-16 (Lin, Liu et al. 2005), and $\dot{\varepsilon}_0$ is a normalising factor with a value of zero. This can be combined with Equation 8-13 to form a dislocation accumulation and recovery balance as shown in Equation 8-17.

$$\dot{\bar{\rho}}_{static} = A\sinh\left(\frac{A_2\sqrt{\rho}}{kT}\right)\exp\left(\frac{-Q_R}{kT}\right) \quad \textbf{Equation 8-14}$$

$$\dot{\bar{\rho}}_{static} = c_1\bar{\rho}^{c_2} \quad \textbf{Equation 8-15}$$

$$c_1 = c_{1,0}\dot{\varepsilon}^0\exp\left(\frac{-Q_c}{kT}\right) \quad \textbf{Equation 8-16}$$

$$\dot{\bar{\rho}} = k_1\left(1-\sqrt{\bar{\rho}}\right)\dot{\varepsilon}_p - c_1\bar{\rho}^{c_2} \quad \textbf{Equation 8-17}$$

8.3 The unified viscoplastic constitutive equation set

The equations described previously can be combined to form the viscoplastic equation set, below. This equation set includes the creep and dislocation-related mechanisms and their mutual interactions.

$$\dot{\varepsilon}_p = \left\langle \frac{\frac{\sigma}{1-D_c} - (k+H)}{K} \right\rangle_+^{n_2} \quad \textbf{Equation 8-18}$$

$$\dot{\bar{\rho}} = k_1\cdot\left(1-\sqrt{\bar{\rho}}\right)\cdot\dot{\varepsilon}_p - c_1\bar{\rho}^{c_2} \quad \textbf{Equation 8-19}$$

$$\sigma = E(\varepsilon_T - \varepsilon_e) \quad \textbf{Equation 8-20}$$

$$H = B\sqrt{\bar{\rho}}$$ **Equation 8-21**

8.4 Viscoplastic damage

Chapters 2 and 3 described that there are three active damage mechanisms during the hot rolling of steel. The growth of voids around inclusions, the growth of voids at grain boundaries and their mutual effect of damage softening through coalescence have to be calculated separately.

8.4.1 Plasticity-based damage

The term plasticity-based damage encompasses the growth of voids around inclusions. Several parameters affect plasticity-based damage: the stress state, inclusion volume fraction, strain rate and temperature. Each of these parameters will be reviewed to establish the damage equation.

Voids grow in the direction of maximum principal stress. The change in damage area, ΔD_i, is proportional to the change in length of the void, δd, and the rate of increase of d with true strain is $\delta d = d \cdot \delta\varepsilon$; this is illustrated in Figure 8.1. It can be argued that the damage rate is proportional to the equivalent plastic strain rate, $\dot{D}_i \propto \dot{\varepsilon}_p$. This was observed empirically through uniaxial tensile tests.

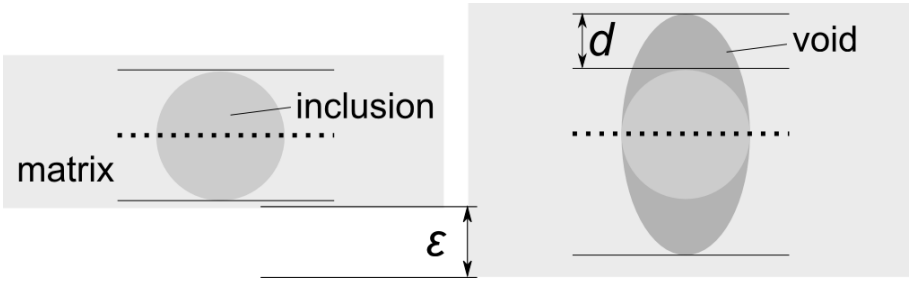

Figure 8.1. Symbolic representation of void growth.

A cast billet's surface material is known to be more ductile than the bulk material and acts as a protective layer against edge cracking during hot rolling. Experiments in Chapter 5 demonstrated that damage rates varied with the average inclusion size and

distribution in the different billet locations. If the deformation parameters are changed, then the surface and centre materials of the billet have different responses and the effect of the inclusion volume fraction is altered. This effect can be partly accounted for by a factor, ω_0, which includes the nearest neighbour, IO, and size, D, of the inclusions in the form of Equation 8-22. Given that the temperature and the strain rate are shown to alter the magnitude of the effect, it is necessary to accommodate this by introducing a phenomenological parameter. The combination is given by, Ω, Equation 8-23, where T_0 is a reference temperature.

$$\omega_0 = \left(D/IO\right)^s \qquad \textbf{Equation 8-22}$$

$$\Omega = \omega_0 \left(1 + \frac{\ln \dot{\varepsilon}}{\ln \left|\dot{\varepsilon}^0\right|}\right)\left(1 - \frac{T - T_o}{T_o}\right) \qquad \textbf{Equation 8-23}$$

Once the inclusion and matrix are debonded, growth in the direction of principal strain occurs. The physical testing described in Chapter 4 demonstrated that the stress state must be included in a damage model. It was found that the model by Brozzo was the best representation of the damage trends observed.

As flow is based on plasticity, it follows that temperature will affect damage softening within the matrix. Therefore, a temperature-dependent factor, z_1, is also introduced to calibrate the plasticity-based damage, in the form shown in Equation 8-25. The final equation is shown in Equation 8-24.

$$\dot{D}_{pl} = z_1 \Omega \frac{\dot{\varepsilon}_p^{\gamma_1}}{\dot{\varepsilon}_0^{\gamma_1 - 1}}\left(\frac{1}{3} + 2\frac{\sigma_m}{\sigma_{eq}}\right)^2 \qquad \textbf{Equation 8-24}$$

$$z_1 = z_{1,0} \exp\left(\frac{-Q_{z1}}{RT}\right) \qquad \textbf{Equation 8-25}$$

8.4.2 Grain boundary damage

Grain boundary damage is due to creep and as such is heavily strain rate dependent. The diffusive processes that permit the nucleation and growth of voids at

grain boundaries are complex. A review of the studies of this damage type is given in Chapter 2; it is generally accepted that the rate of creep damage increases with increasing strain rate. Grain boundary damage is mode I crack separation, and is dependent on the principal stress.

A phenomenological model is generated to account for the grain boundary type damage that has been observed in the previous chapters at higher temperatures and lower strain rates. The strain rate effect is investigated by taking the inverse of the strain rate to an exponent, γ_2. It is generally accepted that grain boundary damage is more significant at lower strain rates (Lin, Liu et al. 2005). Therefore the exponent (γ_2) must be optimised so that the grain boundary damage is lower than the plasticity-induced damage, particularly at high strain rates. The grain boundary damage is expressed by Equation 8-26.

$$\dot{D}_{gb} = z_2 \frac{\dot{\varepsilon}_p^{\gamma_2}}{\dot{\varepsilon}_0^{\gamma_2 - 1}} \left(\frac{\sigma_I}{\sigma_{eq}} \right) \qquad \textbf{Equation 8-26}$$

The constant, z_2, is temperature dependent in order to increase the rate of grain boundary damage at higher temperatures, and takes the form shown in Equation 8-27.

$$z_2 = z_{2_0} \exp\left(\frac{Q_{z_2}}{RT} \right) \qquad \textbf{Equation 8-27}$$

8.4.3 Damage coalescence

Cracks grow between voids in a direction normal to the principal stress, as was seen in micrographs (see Figure 6.4). Therefore, the maximum principal stress, σ_I, is the key parameter that affects the rate of damage coalescence, which is shown in 8. As the localised stress increases, the effect of maximum principal stress is accelerated and in turn, the rate of damage coalescence, $\dot{D}_c$, is increased.

$$\dot{D}_c = z_3 \left\langle \frac{\sigma_I}{1 - D_c} \right\rangle_+ \qquad \textbf{Equation 8-28}$$

Where z_3 is a temperature-dependent constant, which represents the matrix's ability to accommodate a crack given by Equation 3-29.

$$z_3 = z_{3_0} \exp\left(\frac{Q_{z_3}}{RT}\right)$$ **Equation 8-29**

The crack nucleation is possible due to the stored energy of dislocation pile-up at grain boundaries. It is proposed that the dislocations pile up at grain boundaries close to the inclusions as plastic flow is concentrated due to the stress localisation. As 60% of inclusions are found at grain boundaries, it is likely that a crack nucleates at the triple points between the inclusion and two, or more, grains (Farrugia 2008). To account for the dislocation pile-up, the square root of the normalised dislocation density is used.

A higher strain rate produces a stiffer material response. The harder material will be more resistant to plastic deformation and therefore will be less able to resist a crack. The strain rate is included with the term relating to plastic damage.

X-ray microtomography, XMT, was used to demonstrate that the volume fraction of damage is relatively small until close to the failure strain, when it increases rapidly. There is an exponential relationship between the rate of damage softening and the fraction of damage. Clustering and hence the distance between inclusions determines the location of the localised damage, which was observed in both XMT and finite element modelling. The smaller the distance between the inclusions, the greater the stress concentration.

The combined effects of plasticity-induced damage on coalescence are shown in Equation 8-30.

$$\dot{D}_c = \exp\left(\frac{z_4 \cdot \frac{\dot{\varepsilon}_p^{\gamma_3}}{\dot{\varepsilon}_0^{1-\gamma_3}} \cdot \sqrt{\overline{\rho}} \cdot D_{pl}}{L}\right)$$ **Equation 8-30**

The grain boundary damage will also accelerate damage coalescence. This effect is relatively small compared to that of damage growth around inclusions. The equation governing the effect of grain boundary damage on coalescence is given in Equation 8-31.

$$\dot{D}_c = \eta \cdot \exp\left(D_{gb}^{\gamma_4}\right)$$ **Equation 8-31**

The combined coalesced damage equation is presented below:

$$\dot{D}_c = z_3 \left\langle \frac{\sigma_1}{1-D_c} \right\rangle_+ \cdot \left\{ \exp\left(\frac{z_4 \cdot \frac{\dot{\varepsilon}_p^{\gamma_3}}{\dot{\varepsilon}_0^{1-\gamma_3}} \cdot \sqrt{\overline{\rho}} \cdot D_{pl}}{L} \right) + \eta \cdot \exp\left(D_{gb}^{\gamma_4}\right) \right\}$$ **Equation 8-32**

8.5 Calibration of model

The viscoplastic damage equation set (below) can be integrated simultaneously for a specified range of temperatures and strain rates. The equations in the model have a series of constants and temperature-dependent material constants that need to be calibrated for a particular material. This is possible by simultaneously integrating the equations and comparing to physical experimental test data of the materials. The complete viscoplastic damage equation set is presented below:

$$\dot{\varepsilon}_p = \left\langle \frac{\frac{\sigma}{1-D_c} - (k+H)}{K} \right\rangle_+^{n_1}$$ **Equation 8-33**

$$\dot{\overline{\rho}} = k_1 \cdot \left(1 - \sqrt{\overline{\rho}}\right) \cdot \dot{\varepsilon}_p - c_1 \overline{\rho}^{c_2}$$ **Equation 8-34**

$$\sigma = E(\varepsilon_T - \varepsilon_p)$$ **Equation 8-35**

$$H = B\sqrt{\overline{\rho}}$$ **Equation 8-36**

$$\dot{D}_{pl} = z_1 \Omega_{t,\dot{\varepsilon}} \frac{\dot{\varepsilon}_p^{\gamma}}{\dot{\varepsilon}_0^{1-\gamma}} \left(\frac{1}{3} + 2\frac{\sigma_m}{\sigma_{eq}} \right)^2$$ **Equation 8-37**

$$\dot{D}_{gb} = z_2 \frac{\dot{\varepsilon}_p^{\gamma_2}}{\dot{\varepsilon}_0^{1-\gamma_2}} \left(\frac{\sigma_1}{\sigma_{eq}} \right)$$ **Equation 8-38**

$$\dot{D}_c = z_3 \left\langle \frac{\sigma_I}{1-D_c} \right\rangle_+ \cdot \left\{ \exp\left(\frac{z_4 \cdot \frac{\dot{\varepsilon}_p^{\gamma_3}}{\dot{\varepsilon}_0^{1-\gamma_3}} \cdot \sqrt{\overline{\rho}} \cdot D_{pl}}{L} \right) + \eta \cdot \exp\left(D_{gb}^{\gamma_4} \right) \right\} \qquad \textbf{Equation 8-39}$$

The first stage in the calibration process is the determination of the boundary values. Several terms have fixed values based on their physical meanings (e.g. the mode inclusion nearest neighbour). There are evolutionary algorithms available that can be used to automatically calibrate the material constants (Li, Lin et al. 2002). However, this is computationally expensive, and requires assistance in implementation. As the majority of the constants have a limited range, it was possible to find the bounds for most of the constants but the remaining constants have to be determined by trial and error methods. There were also simplifications that could be applied to reduce the number of constants during calibration.

One simplification is to initially calibrate the constants for a single temperature and a range of strain rates. There are several temperature-dependent constants of the form shown in Equation 8-40, where z_{1_0} and Q_{z_1} are material-dependent constants. The equations were calibrated individually at temperatures of 900, 1000 and 1100 °C, which removed the temperature dependence. The material constants controlling the temperature-related constants were calibrated based on their related temperature-dependent constants at different temperatures.

$$z_1 = z_{1_0} \exp\left(\frac{-Q_{z_1}}{RT} \right) \qquad \textbf{Equation 8-40}$$

The constitutive equation set can then be integrated at a strain rate equal to 1 s^{-1} and a range of temperatures. Under this condition the strain rate exponents can be ignored.

Another simplification was to remove the equations representing mechanisms that had minimal effect at the particular stages of the deformation process. For instance, damage has a minimal effect at the start of deformation, as can be seen in Figure 8.2. As the damage is low, the effect of damage softening was negligible and these equations could be ignored. This assumption is in agreement with observations made using XMT in

Chapter 7. Therefore, the viscoplastic model was calibrated and then updated with the damage equations.

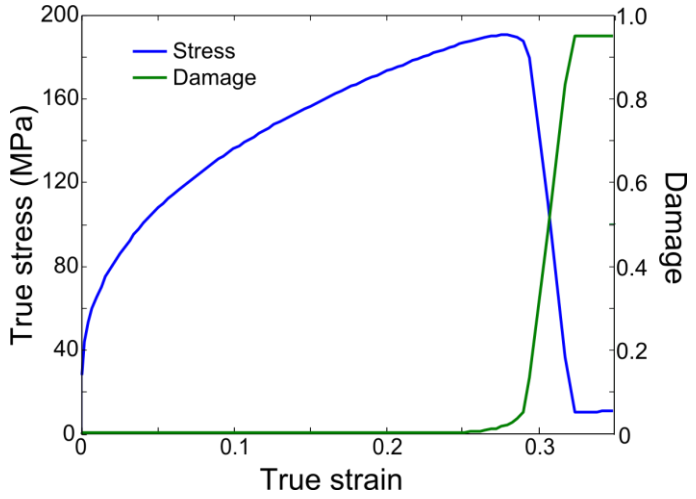

Figure 8.2. The evolution of stress and damage according to the viscoplastic equation set.

The constants in the viscoplastic damage equations were calibrated using experimental data from uniaxial tensile tests. The tests were performed at temperatures of 900, 1000 and 1100 °C and strain rates of 0.1, 1, and 10 s^{-1}. The calibrated constants are shown in Table 8-1.

Table 8-1. Material constants determined for viscoplastic model.

c_2	K	K_1	l	n	T_1
0.6	11	0.0031	14×10^{-5}	1.7	900
z_4	η	γ_1	γ_2	γ_3	γ_4
100	9×10^{-4}	0.5	-0.2	-0.99	2

Table 8-2. Constants related to temperature dependence, determined for viscoplastic model.

B_0	E_0	$c_{1,0}$	k	$k_{1,0}$	α	$\dot{\varepsilon}_0$
176	8800	13.1	0.2	1.1	0.0031	0
$z_{1,0}$	$z_{2,0}$	$z_{3,0}$	Q_{c1}	Q_{k1}	Q_{z1}	Q_{z2}
9×10^{-11}	15×10^{-5}	1×10^{-13}	4.23×10^5	4.21×10^5	2.62×10^5	2.62×10^3

The mechanical response measured from experiments (symbols) is compared to the calibrated model (curves) in Figure 8.3.

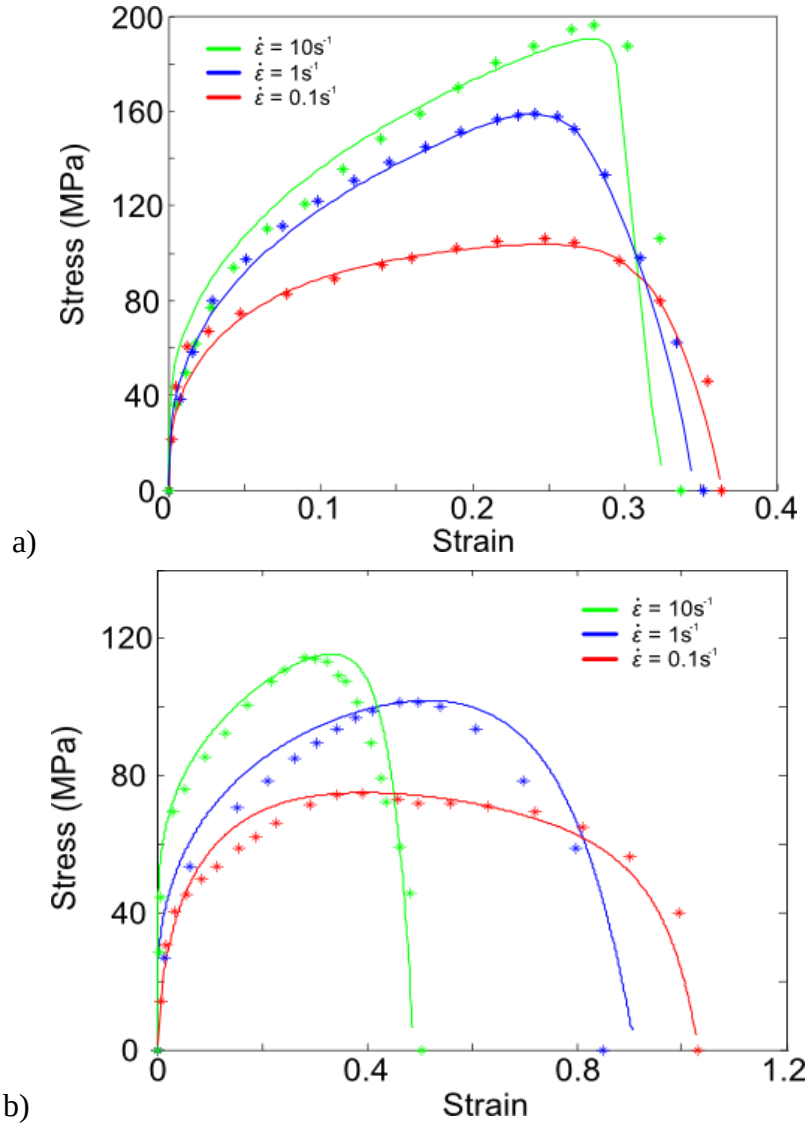

Figure 8.3. Calibrated viscoplastic damage model for leaded free cutting steel; markers for experimental data and solid lines for model a) Temp = 900 °C and b) 1100 °C.

8.6 Conclusions

The experiments and observations made for the previous chapters have been used to create a physically based model. The viscoplastic aspects of the model were developed from established theory. Test geometries with constant stress distributions were used to assess the most appropriate factor for stress state in Chapter 4. The active damage mechanisms were identified in Chapter 6. The effect of inclusion size and spacing at different temperatures was investigated in Chapters 5 and 7. The pertinent mechanisms

are included in the model and are applicable for a range of free cutting steels. The reduced number of constants means that the damage model can be calibrated based on uniaxial tensile tests. The matching material response of the model to experimental data confirms the validity of the model for leaded free cutting steel.

Chapter 9 Conclusions and future work

9.1 Observed damage mechanisms

The additions of heavy metals, which give free cutting steels increased machinability, are found to precipitate at the boundary between inclusions and matrix steel and so reduce the cohesive strength between them. Both grain boundary-type and plastic-type damage were observed during deformations between 900 °C and 1100 °C at strain rates between 0.1 s^{-1} and 10 s^{-1}. The relative amount of each type of damage was dependent on the deformation parameters. Generally, higher ductility was found with increased temperature and lower strain rates for all free cutting steels examined.

The distribution of inclusions varied through the cast billet, with more numerous and smaller inclusions found within the first 40mm of the surface. The surface material for the free cutting steels has increased ductility, which is termed the surface material ductility effect. This effect on ductility decreases at higher temperatures and lower strain rates.

9.1.1 Stress state

A test-piece designed to relate the stress state to damage demonstrated that growth around inclusions occurs at a stress triaxiality above 0.1. However, grain boundary damage was visible in negative stress triaxialties as long as the maximum principal stress was tensile. Inclusion cracking was found in compressive stress states, particularly at higher strain rates.

9.1.2 Strain rate and temperature

As demonstrated in previous studies the strain rate and temperature affect material response. A typical viscoplastic response has been observed, with increased strain rate producing a harder material response. The various damage mechanisms, grain boundary and plastic type, become active in the range of parameters examined.

9.1.3 X-ray microtomography

X-ray microtomography is a novel technology and was used to establish the distribution of inclusions, damage and as-cast porosity in three dimensions. This is used to verify the stress localising effects of these anisotropic micro defects on the evolution of damage within the matrix. The stress discontinuities caused by inclusions interact, which means that the local stresses are very different from the macroscopic stress. The results were used to measure a factor that represents the distribution and sizing of the inclusions.

9.2 Material modelling

The individual dominant mechanisms were modelled by taking a combined mechanistic and phenomenological approach. The model included dislocation hardening and softening, creep as well as damage due to dislocations and creep. The interactions of the various material mechanisms was encapsulated using a constitutive equation set. The equation set has been calibrated for leaded free cutting steel.

9.3 Future Work

9.3.1 Inclusion of back stress in viscoplastic model

Kinematic hardening is a more realistic representation of process that occurs in multiple-pass hot rolling due to the multiple reverse loading cycles that occur. A kinematic hardening term, *x*, could be introduced to the plastic strain rate calculation, as shown in Equation 9-1. This would be especially useful if static recrystallisation were included in the model.

$$\dot{\varepsilon}_p = \left\langle \frac{\sigma - (k + H + x)}{K} \right\rangle_+^{n_1} \qquad \textbf{Equation 9-1}$$

9.3.2 Calibration of model for other free cutting steels

The damage model is based on the deformation mechanisms observed in several free cutting steels, FCS. A full test matrix of each FCS will allow calibration of the equation set for each material. The same material model described in this thesis can be

used for each FCS. The damage models should be implemented into the industrial process.

9.3.3 Calibration at different stress states

The equivalent plastic strain to failure is markedly dissimilar in different stress states (Wierzbicki, Bao et al. 2005). For instance, the strain to failure in tension is very different than in compression. Several material models attempt to take the effect of stress state into account. However, the constants are calibrated against a particular stress state, usually plane strain or uniaxial tension. Thus, from what can be seen in the variety of mechanisms under different stress states, the damage equation's constants may have to be re-evaluated for different triaxialities. It would be useful to generate a series of simple tests to evaluate material response under different stress triaxialities for the purpose of calibrating the material model.

9.3.4 Grain size effects

Grain size is known to affect ductility. The grain size could be investigated, along with the inclusion distribution at different depths in the cast billet, to establish their mutual and combined effect on ductility. As inclusions can interfere with grain growth kinetics, this would be a complex problem.

9.3.5 In-situ X-ray microtomography

X-ray microtomography was used to identify damage sites through ex-situ tests, due to the increased precision of the data compared to in-situ tests. If ex-situ tests were performed on virgin samples an accurate measure of the inclusion distribution could be made. Following this high temperature in-situ tensile test could be performed on the same samples. This would establish the effects of the initial distribution, in particular clustering, of the inclusions on damage localisation.

9.3.6 Damage healing

Work has been done to show that damage can be healed. If a surface crack is closed during rolling it may not be beneficial as the cracks usually hide rolled-in oxides beneath the material's surface (Eriksson 2004). Therefore, damage healing should be

investigated up to void growth but not coalescence. Bogatov demonstrated that material can be forced to flow into voids and hence heal damage (Bogatov 2003). Bogatov described the heating as annealing leading the ‘healing’ processes. Kolmogorov looked at healing using heat under triaxial and uniaxial compression (Kolmogorov and Smirnov 1998). Uniform triaxial compression was found to initiate the development of metal micro-creep in internal discontinuities (compression was set to 8% yield strength). Although there was some undesirable permanent creep, the small strains proved sufficient for complete damage healing.

Appendix A – Flow diagram for triaxiality algorithm

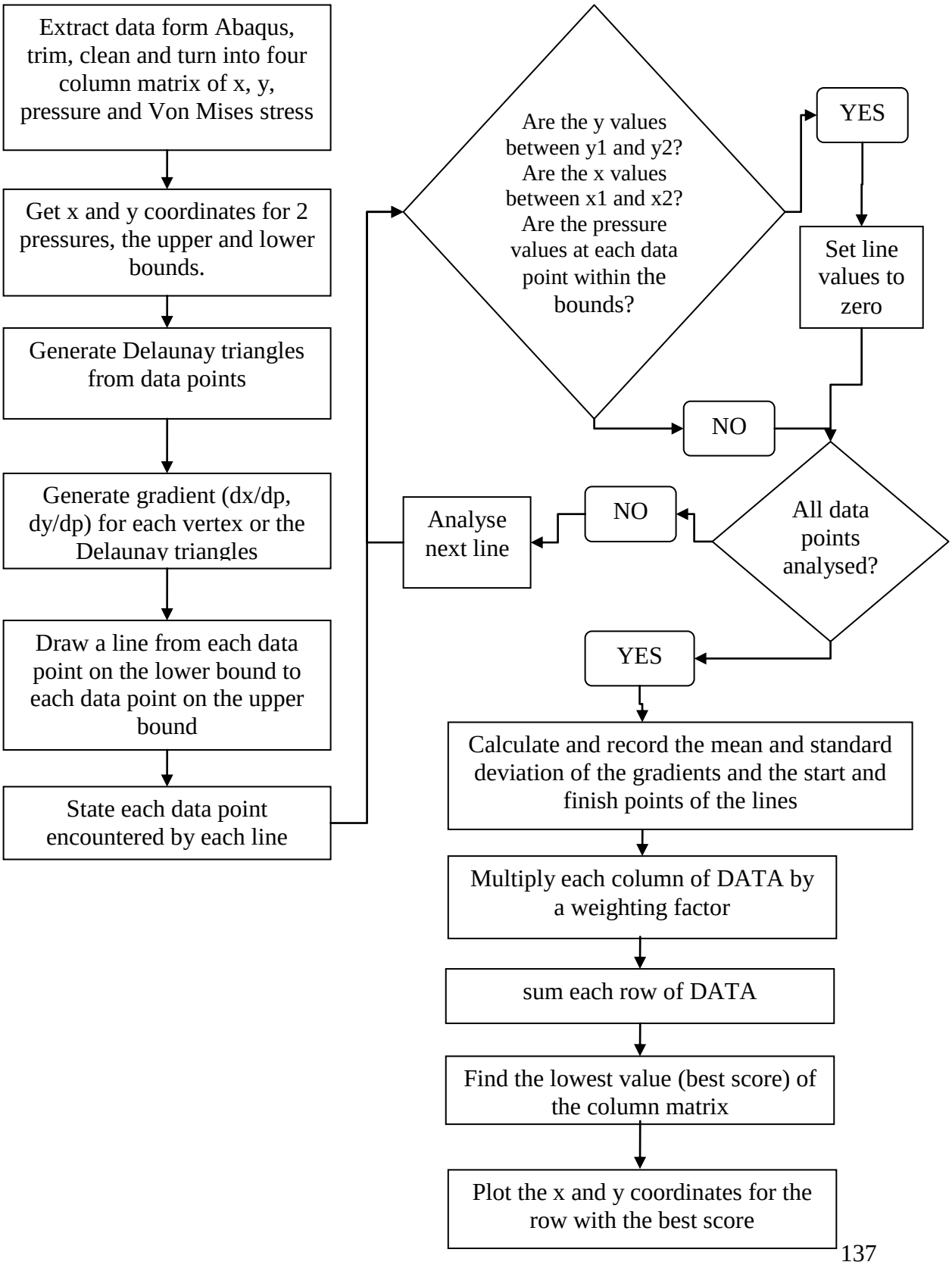

Appendix B - Synchrotron Tomography of FCS Interrupted test

Scanning Conditions

Experiment type	Tomography at I12 beamline
Camera	PCO 4000
Module	3
Field of view (pixels)	4008*2672
Pixel size (um)	1.8
Scintillator	85 um LuAG:Ce scintillator
Exposure time (ms)	~1000
Energy (keV)	76.5
Number of projections	3000
Rotation (deg)	0-180
Angular increment	0.06

Flat field and Dark field before and after scan are required.

The sample has Manganese Sulphide inclusions with diameter of 8 μm. An example of a previous (processed) scan is shown in Figure 9.1.

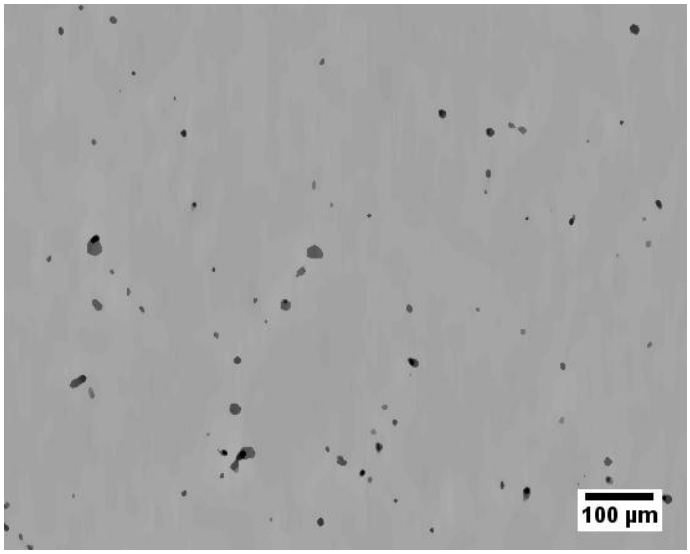

Figure 9.1. Slice of sample showing MnS inclusions within steel matrix.

Scanning Procedure

Please mount the sample onto the rotation stage and scan in the way that notched area between highlighted bars can be seen in the field-of-view at all time. The scanning conditions are shown above and the example of mounting procedure is shown in the figures below.

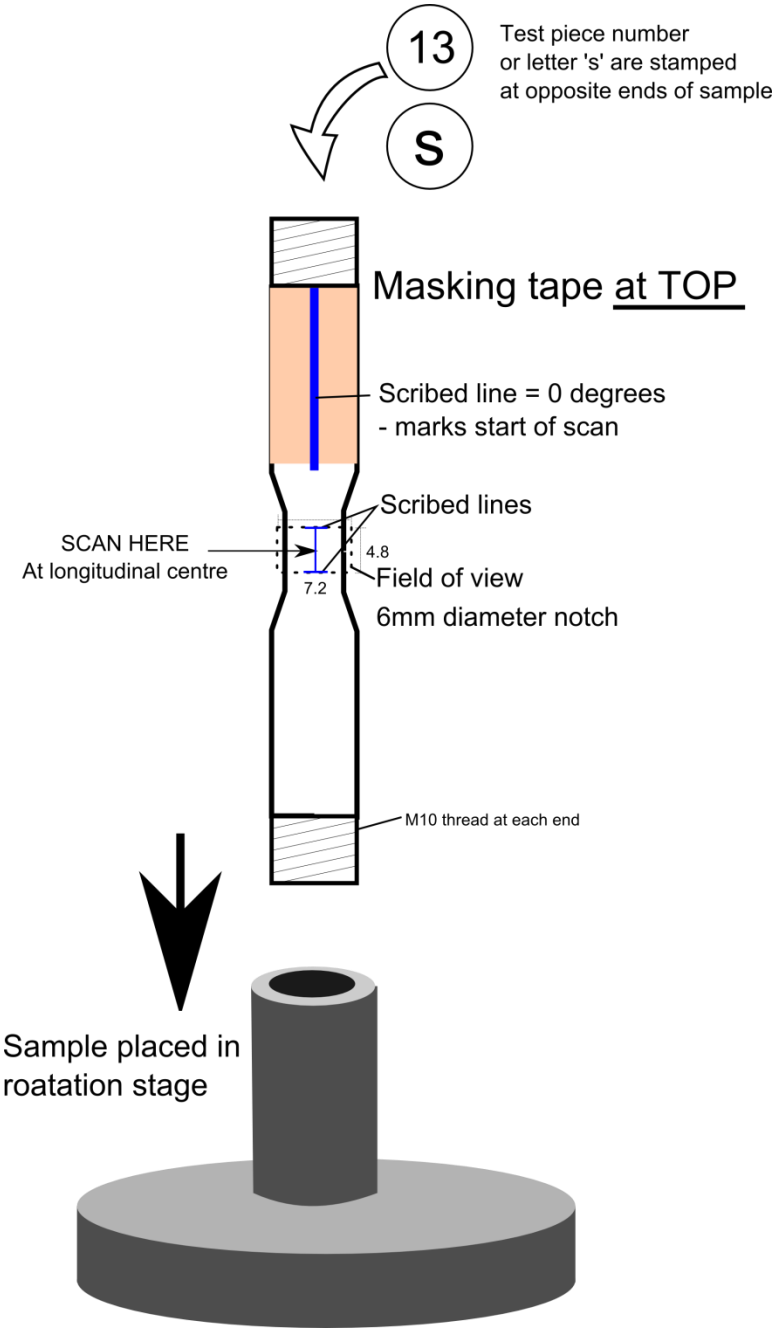

Figure 1: Notch region between two red lines must be always in the field-of-view

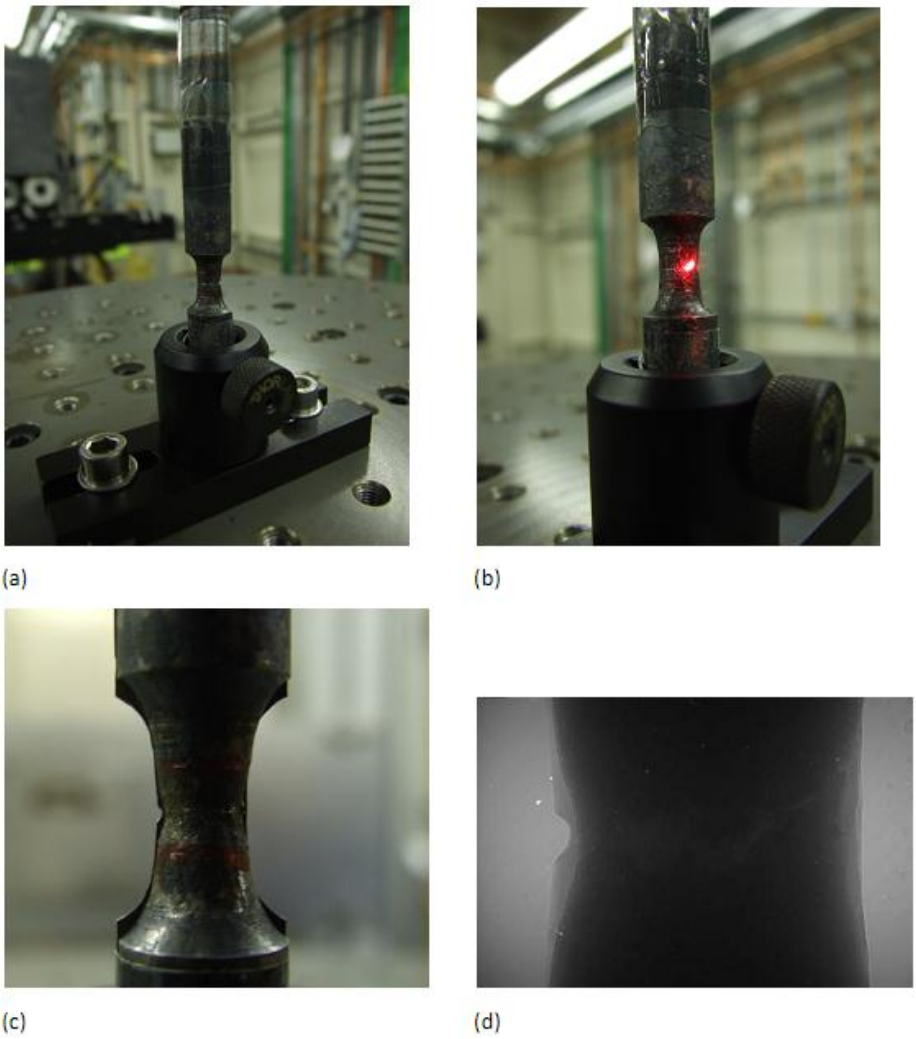

Figure 2: (a) Sample mounted ready for tomography. (b) Alignment laser showing approximate beam position, between the red lines. (c) Photo of sample when theta at 45 degrees, showing notch on
left. (d) Corresponding X-ray projection when theta at 45 degrees.

Sample information

Sample Information :	Free cutting steel
Sample Material or Protein (include all components)*	Steel
Sample Type*	metal, solid
Volume (including units)	7000mm3
Weight (including units)	100g
Chemical Formula or composition (include all components & isotopes)	FeC
CAS number	No
Special Storage Required?	No
Special Storage Details	
Sample Holder, container or substrate	No
Crystallographic Parameters	No
a	
b	
c	
alpha	
beta	
gamma	
At temperature	
Space Group	
Step 6b: Sample Environment	
Standard Equipment*	
Sensitive to Air?	*No*
Sensitive to Vapour?	*No*
Lower Temperature	*293*
Higher Temperature	
Lower Pressure	*1*
Higher Pressure	*1*
Lower Magnetic	*0*
Higher Magnetic	*0*
Step 6c: Sample Safety	
Is your experiment radioactive? *	*No*
If yes please give full details*	
Are there any other hazards associated with your sample?	*No*
If yes please give full details*	
Freezing: Please specify which cryogen you will be using, otherwise select none? *	*No*
Removal*	*Removed by User*
Step 6d: When is the sample at Diamond?	
Date	*During Experiment*

Appendix C – Test results for two free cutting steels

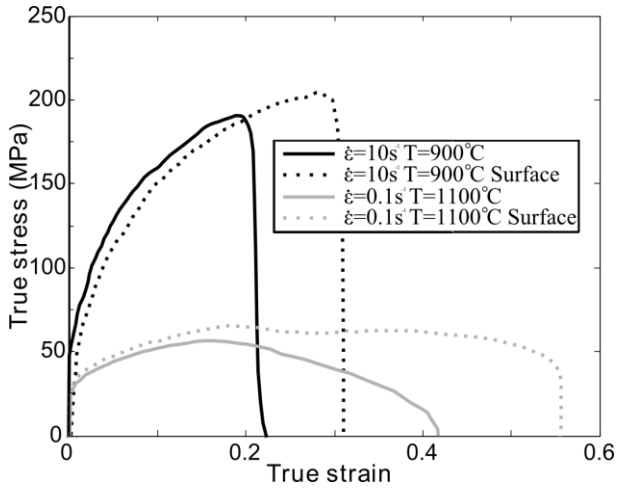

Figure 9.2. Uniaxial tensile test results for Bismuth-Free-Cutting-Steel (BiFCS).

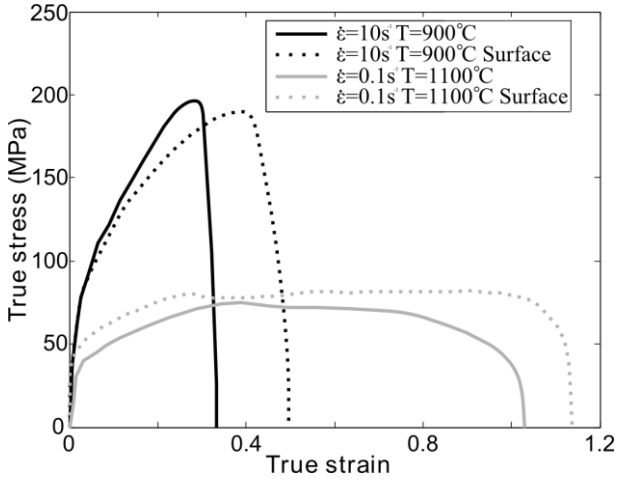

Figure 9.3. Uniaxial tensile test results for Lead-Free-Cutting-Steel (LFCS).

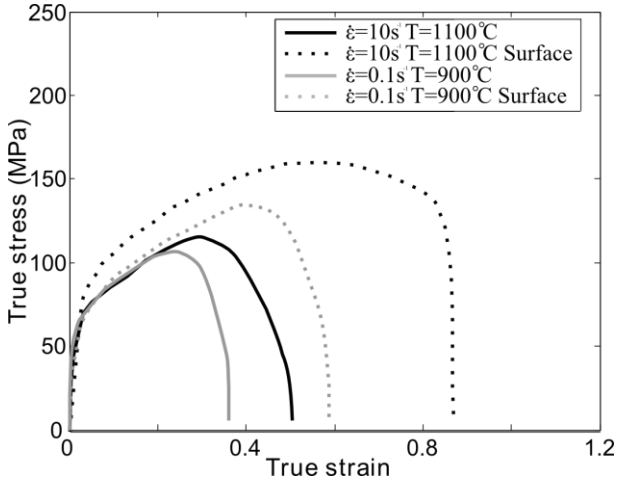

Figure 9.4. Uniaxial tensile test results for Lead-Free-Cutting-Steel (LFCS).

References

Andrade Pires, F. M., E. A. de Souza Neto, et al. (2004). "On the finite element prediction of dmage growth and fracture initiation in finitely deforming ductile materials." Computer methods in applied mechanics and engineering **193**: 5223-5256.

Argon, A., J. Im, et al. (1975). "Cavity formation from inclusions in ductile fracture." Metallurgical transactions **A 6**(4): 825-837.

Argon, A. S., J. Im, et al. (1975). "CAVITY FORMATION FROM INCLUSIONS IN DUCTILE FRACTURE." Metallurgical transactions **A 6**(4): 825-837.

Ashby, M. F. and D. R. H. Jones (1996). Engineering Materials 1, Butterworth Heineman, Oxford.

Babout, L., E. Maire, et al. (2001). "Characterization by X-ray computed tomography of decohesion, porosity growth and coalescence in model metal matrix composites." Acta Materialia **49**(11): 2055-2063.

Babout, L., E. Maire, et al. (2004). "Damage initiation in model metallic materials: X-ray tomography and modelling." Acta Materialia **52**(8): 2475-2487.

Bacha, A. and D. Daniel (2008). "Metal ductility at low stress triaxiality application to sheet trimming." Journal of materials processing technology **203**(1-3): 480-483.

Bacha, A., D. Daniel, et al. (2008). "Metal ductility at low stress triaxiality application to sheet trimming." Journal of materials processing technology **203**(1-3): 480-497.

Balluffi, R. W., S. M. Allen, et al. (2005). Kinetics of materials Hoboken, NJ ; Chichester : Wiley, John Wiley.

Bao, Y. and T. Wierzbicki (2004). "On fracture locus in the equivalent strain and stress triaxiality space." International Journal of Mechanical Sciences **46**(1): 81-98.

Bao, Y. and T. Wierzbicki (2005). "On the cut-off value of negative triaxiality for fracture." Engineering fracture mechanics **72**(7): 1049-1069.

Belov, V. A., A. A. Bogatov, et al. (1985). "A Study of the Change in Damage of the Steel 40Kh During Cold Plastic Deformation and Heat Treatment." Fizika metallov i metallovedenie **60**(5): 1004.

Benzerga, A., J. Besson, et al. (2004). "Anisotropic ductile fracture Part I: experiments." Acta Materialia **52**(15): 4623-4638.

Besson, J. (2010). "Continuum Models of Ductile Fracture: A Review." International journal of damage mechanics **19**(1): 3-52.

BIS (2010). The allocation of science and research funding 2011/12 to 2014/15, Department for Business Innovation and Skills.

Bogatov, A. A. (2003). The mechanics of the ductile damage under the metal forming. ESAFORM 2003.

Böhm, H. J., A. Eckschlager, et al. (2002). "Multi-inclusion unit cell models for metal matrix composites with randomly oriented discontinuous reinforcements." Computational materials science **25**(1-2): 42-53.

Bonora, N. (1997). "On the effect of triaxial state of stress on ductility using nonlinear CDM model." International journal of fracture **88**(4): 359-371.

Bonora, N., G. Newaz, et al. (2005). "Ductile damage evolution under triaxial state of stress: Theory and experiments." International journal of plasticity **21**(5): 981-1007.

Bouchard, P. O., L. Bourgeon, et al. (2008). "On the influence of particle distribution and reverse loading on damage mechanisms of ductile steels." Materials Science and Engineering: A **496**(1-2): 223-233.

Boyer, J.-C., E. Vidal-Sallé, et al. (2002). "A shear stress dependent ductile damage model." Journal of Materials Processing Technology **121**(1): 87-93.

Bridgman, P. W. (1953). Studies in Large Plastic Flow and Fracture with Special Emphasis on the Effects of Hydrostatic Pressure. New York, McGraw Hill Co.

Brown, L. and W. Stobbs (1971). "WORK-HARDENING OF COPPER-SILICA .1. MODEL BASED ON INTERNAL STRESSES, WITH NO PLASTIC RELAXATION." Philosophical magazine **23**(185): 1185.

Brozzo, P., B. Deluca, et al. (1972). A new method for the prediction of formability limits in metal sheets. 7th Biennial Conference of the International Deep Drawing Research Group.

Brust, F. W. and B. N. Leis (1992). "A NEW MODEL FOR CHARACTERIZING PRIMARY CREEP DAMAGE." International journal of fracture **54**(1): 45-63.

Callister, W. D. (2007). Materials Science and Engineering: An Introduction. New York, John Wiley & Sons

Chan, K. and D. Davidson (1999). "Evidence of void nucleation and growth on planar slip bands in a Nb-Cr-Ti alloy." Metallurgical and Materials Transactions; A; Physical Metallurgy and Materials Science **30**(3): 579-585.

Cho, K. S., J. H. Choi, et al. (2008). "A novel etchant for revealing the prior austenite grain boundaries and matrix information in high alloy steels." Materials characterization **59**(6): 786-793.

Chokshi, A. (1987). "A model for diffusional cavity growth in superplasticity." Acta metallurgica **35**(5): 1089-1101.

Clift, S. E., P. Hartley, et al. (1990). "Fracture prediction in plastic deformation processes." International Journal of Mechanical Sciences **32**(1): 1-17.

Cockcroft, M. G. and D. J. Latham (1968). "Ductility and the Workability of Metals." J. Inst. Met.(96): 6.

Cocks, A. C. F. and M. F. Ashby (1982). "On creep fracture by void growth." Progress in materials science **27**(3-4): 189-244.

Cusiminsky, G. and F. Ellis (1967). "An investigation into the influence of edge shape on cracking during rolling." Journal of the Institute of Metals **95**: 33-37.

Denissen, C. J. M., J. Liebe, et al. (2006). "Recrystallisation temperature of tungsten as a function of the heating ramp." International journal of refractory metals & hard materials **24**(4): 321-324.

Dodd, B. and P. Boddington (1980). "The causes of edge cracking in cold rolling." Journal of Mechanical Working Technology **3**(3-4): 239-252.

DSI (2011). Gleeble Operations Manual.

Duan, X. and T. Sheppard (2002). "Influence of forming parameters on static recrystallization behaviour during hot rolling aluminium alloy 5083." Modelling and Simulation in Materials Science and Engineering **no.3 4**(4): 363-380.

Dunne, F. and I. Katramados (1998). "Micro-mechanical modelling of strain induced porosity under generally compressive stress states." International journal of plasticity **14**(7): 577-595.

Dunne, F. P. E., A. J. Wilkinson, et al. (2007). "Experimental and computational studies of low cycle fatigue crack nucleation in a polycrystal." International journal of plasticity **23**(2): 273-295.

Duprez, L. (2002). "Flow stress and ductility of duplex stainless steel during high-temperature torsion deformation." Metallurgical and Materials Transactions; A; Physical Metallurgy and Materials Science **33**(7): 1931-1938.

Dyson, B. F. (1988). "Creep and fracture of metals: mechanisms and mechanics." Revue. de Physique Appliquee **23**: 605-613.

Dyson, B. F. and M. McLean (1983). "PARTICLE-COARSENING, SIGMA-0 AND TERTIARY CREEP." Acta metallurgica **31**(1): 17-27.

Eriksson, C. (2004). "Surface cracks in wire rod rolling." Steel research **75**(12): 818.

Ervasti, E. and U. Stahlberg (2005). "Void initiation close to a macro-inclusion during single pass reductions in the hot rolling of steel slabs: A numerical study." Journal of Materials Processing Technology **170**(1-2): 142-150.

Estrin, Y., L. S. Toth, et al. (1998). "A dislocation-based model for all hardening stages in large strain deformation." Acta Materialia **46**(15): 5509-5522.

Everett, R. K. and A. B. Geltmacher (1999). "Spatial distribution of MnS inclusions in HY-100 steel." Scripta materialia **40**(5): 567-571.

Farrugia, D. (2010). "High temperature ductile damage during rolling of free cutting steels." Ironmaking & steelmaking **37**(4): 298-305.

Farrugia, D. C. J. (2006). "Prediction and avoidance of high temperature damage in long product hot rolling." Journal of materials processing technology **177**(1-3): 486-483.

Farrugia, D. C. J. (2008). Research Programme of the Research Fund for Coal and Steel Steel RTD. Internal report. D. C. J. Farrugia. London, TGS4 Hot and cold rolling processes.

Farrugia, D. C. J. (2008). Revised plane strain mechanical testing for studying ductile damage of free cutting steel. 12th International Conference on Metal Forming, Verlag Stahleisen Mbh, Sohnstrabe 65, D-40237 Dusseldorf, Germany. **Sp. Iss. 2:** 361-368.

Farrugia, D. C. J., I. Baillie, et al. (2007). The prediction and avoidance of cracking in long product hot rolling. C. U. Limited, S. I. D, CEIT, I. S. O. An and Ascometal, Corus UK Limited, 30 Millbank, London, SW1P 4WY.

Fionn, D. and N. Petrinic (2005). Introduction to Computational Plasticity OUP Oxford

Foster, A. (2007). Damage modelling in free machining steels. Mechanical Engineering, The University of Birmingham. **PhD**.

Foster, A. D., T. A. Dean, et al. (2007). "Investigation into damage nucleation and growth for a free-cutting steel under hot-rolling conditions." The Journal of strain analysis for engineering design **42**(4): 227-235.

Foster, A. D., T. A. Dean, et al. (2007). "Modeling material flow characteristics over multiple recrystallization cycles." AIP conference proceedings **907**(1): 59-63.

Foster, A. D., J. Lin, et al. (2006). "Experimental investigation of the spatial variation in viscoplastic response of free-machining steels in hot rolling conditions." Journal of materials processing technology **177**(1-3): 497-500.

Foster, A. D., J. Lin, et al. (2009). "A Test for Evaluating the Effects of Stress-States on Damage Evolution with Specific Application to the Hot Rolling of Free-Cutting Steels." International Journal of Damage Mechanics: 1056789509343077.

French, I. (1975). "The influence of hydrostatic pressure on the tensile deformation and fracture of copper." Metallurgical and Materials Transactions; A; Physical Metallurgy and Materials Science **6**(3): 785-790.

Frost, H. J. and M. F. Ashby (1969). Deformation-Mechanism Maps, The Plasticity and Creep of Metals and Ceramics, http://engineering.dartmouth.edu/defmech/.

Fuloria, D. and P. Lee (2009). "An X-ray microtomographic and finite element modeling approach for the prediction of semi-solid deformation behaviour in Al-Cu alloys." Acta Materialia **57**(18): 5554-5562.

Gangalee, A. and J. Gurland (1967). Transaction of the Mettalurgical Society.

Gao, X., G. Zhang, et al. (2010). "A Study on the Effect of the Stress State on Ductile Fracture." International journal of damage mechanics **19**(1): 75-94.

Garcia-Mateo, C., B. Lopez, et al. (1999). "Influence of vanadium on static recrystallization in warm worked microalloyed steels." Scripta materialia **42**(2): 137-143.

Garrison, W. and A. Wojcieszynski (2007). "A discussion of the effect of inclusion volume fraction on the toughness of steel." Materials science & engineering. A, Structural materials: properties, microstructure and processing **464**(1-2): 321-329.

Gawdzinska, K., J. Grabian, et al. (2003). "Analysis of defects formation in as-cast metal saturated composites." METALURGIJA **42**(2): 135-140.

George, M. W. (2008). Selenium and tellurium. 2007 Minerals Yearbook, U.S. Geological Survey.

Ghadbeigi, H., C. Pinna, et al. (2010). "Local plastic strain evolution in a high strength dual-phase steel." Materials Science and Engineering: A **527**(18-19): 5026-5032.

Gomuc, R. and T. Bui-Quoc (1986). "An Analysis of the Fatigue/Creep Behavior of 304 Stainless Steel Using a Continuous Damage Approach." Journal of pressure vessel technology **108**(3): 280.

Gouveia, B. P. P. A., J. M. C. Rodrigues, et al. (1996). "Fracture predicting in bulk metal forming." International Journal of Mechanical Sciences **38**(4): 361-372.

Gurson, A. L. (1977). "Continuum theory of ductile rupture by void nucleation and growth: Part 1 - Yield criteria and flow rules for porous ductile media." Journal of Engineering Materials and Technology **99**: 2-15.

Hahn, G. T., M. F. Kanninen, et al. (1972). "Fracture Toughness of Materials." Annual Review of Materials Science **2**(1): 381-404.

Hammi, Y. and M. F. Horstemeyer (2007). "A physically motivated anisotropic tensorial representation of damage with separate functions for void nucleation, growth, and coalescence." International journal of plasticity **23**(10-11): 1641-1678.

Han, J., Z. Zhao, et al. (2007). "Inner Crack Heat-healing in Low Carbon Steel with Lanthanum." Materials science forum **539-543**: 4738-4743.

Harry, M. (1988). The Nature of six sigma quality. Rolling Meadows, IL:, Motorola University Press.

Hayhurst, D. R., J. Lin, et al. (2008). "Failure in notched tension bars due to high-temperature creep: Interaction between nucleation controlled cavity growth and

continuum cavity growth." International Journal of Solids and Structures **45**(7-8): 2233-2250.
Hearn, E. J. (1997). Mechanics of Materials: v. 1: An Introduction to the Mechanics of Elastic and Plastic Deformation of Solids and Structural Materials, Butterworth-Heinemann Ltd.
Hirth. John., P. and L. Jens (1992). Theory of dislocations. Malabar, Florida, Krieger publishing company.
Horstemeyer, M. and A. Gokhale (1999). "A void-crack nucleation model for ductile metals." International journal of solids and structures **36**(33): 5029-5055.
Horstemeyer, M. F. and A. M. Gokhale (1999). "A void-crack nucleation model for ductile metals." International Journal of Solids and Structures **36**(33): 5029-5055.
Horstemeyer, M. F., J. Lathrop, et al. (2000). "Modeling stress state dependent damage evolution in a cast Al-Si-Mg aluminum alloy." Theoretical and Applied Fracture Mechanics **33**(1): 31-47.
Hosseini, S. B., C. Temmel, et al. (2007). "An in-situ scanning electron microscopy study of the bonding between MnS inclusions and the matrix during tensile deformation of hot-rolled steels." Metallurgical and materials transactions. A, Physical metallurgy and materials science **38A**(5): 982-989.
Huang, Y., A. Chandra, et al. (1998). "Void-nucleation vs void-growth controlled plastic flow localization in materials with nonuniform particle distributions." International Journal of Solids and Structures **35**(19): 2475-2486.
Humphreys, F. J. and M. Hatherly (1996). Recrystallization and related annealing phenomena. Oxford, Elsevier.
Hwang, B., S. Lee, et al. (2005). "Analysis and prevention of side cracking phenomenon occurring during hot rolling of thick low-carbon steel plates." Materials science & engineering. A, Structural materials **402**(1-2): 177-187.
Irwin (1958). Fracture I Handbuch der Physik. Flugger, Springer.
J. Cao, J. L. T. A. D. (2008). An implicit unitless error and step-size control method in integrating unified viscoplastic/creep ODE-type constitutive equations. **73:** 1094-1112.
Kachanov, L. M. (1958). "Rupture time under creep conditions." Izvestia Akademii Nauk SSSR, Otdelenie tekhnicheskich nauk **8**: 26-31.
Kalpakjian, S. (1984). Manufacturing processes for engineering materials Addison-Wesley.
Kalpakjian, S. (1984). Manufacturing Processes for Engineering Materials. Reading, Addison-Wesley.
Kao, A. (1990). "Influence of superimposed hydrostatic-pressure on bending fracture and formability of a low-carbon steel containing globular sulfides." Journal of engineering materials and technology-transactions of the ASME **112**(1): 26-30.
Kaye, M., D. D. S. Balint, et al. (2010). "Quantifying the effect of mns precipitate distributions on the ductility of free cutting steels." Journal of Multiscale Modelling.
Kim, J. (1999). "Microstructural analysis on boundary sliding and its accommodation mode during superplastic deformation of Ti-6Al-4V alloy." Materials science and engineering a-structural materials properties microstructure and processing **263**(2): 272-280.

Kim, J., X. Gao, et al. (2004). "Modeling of void growth in ductile solids: effects of stress triaxiality and initial porosity." Engineering Fracture Mechanics **71**(3): 379-400.
Kocks, U. F. and H. Mecking (2003). "Physics and phenomenology of strain hardening: the FCC case." Progress in materials science **48**(3): 171-273.
Kolmogorov, V. L. and S. V. Smirnov (1998). "Restoration of the margin of metal plasticity after cold deformation." Journal of materials processing technology **74**(1-3): 83-88.
Koplik, J. and A. Needleman (1988). "Void growth and coalescence in porous plastic solids." International Journal of Solids and Structures **24**(8): 835-853.
Kovac, M. and L. Cizelj (2005). "Modeling elasto-plastic behavior of polycrystalline grain structure of steels at mesoscopic level." Nuclear engineering and design **235**(17-19): 1939-1950.
Krompholz, K. and D. Kalkhof (2003). "Fracture initiation of geometrically scaled, notched three-point-bend bars of a low-alloy ferritic steel." Engineering Fracture Mechanics **70**(17): 2459-2472.
Leckie, F. and D. Hayhurst (1977). "Constitutive equations for creep-rupture." Acta metallurgica **25**(9): 1059-1070.
Lemaitre, J. and J. L. Chaboche (1990). Mechanics of Solid Materials.
Lenard, J. G., M. Pietrzyk, et al. (1999). Mathematical and physical simulation of the properties of hot rolled products, Elsevier.
Leroy, G. (1981). "A model of ductile fracture based on the nucleation and growth of voids." Acta metallurgica **29**(8): 1509-1522.
Lewandowski, J. (1991). "Observations on the effects of particulate size and superposed pressure on deformation of metal matrix composites." Scripta metallurgica et materialia **25**(1): 21-26.
Li, B., J. Lin, et al. (2002). "A novel evolutionary algorithm for determining unified creep damage constitutive equations." International journal of mechanical sciences **44**(5): 987-1002.
Limited, C. U. (2008). Research Programme of the Research Fund for Coal and Steel Steel RTD. Internal report. D. C. J. Farrugia. London, TGS4 Hot and cold rolling processes.
Lin, J. (2004). "Investigation of damage features in hot metal forming materials processing and design: modeling, simulation and applications, pts 1 and 2." AIP conference proceedings **712**: 1851-1856.
Lin, J. and F. P. E. Dunne (2001). "Modelling grain growth evolution and necking in superplastic blow-forming." International Journal of Mechanical Sciences **43**(3): 595-609.
Lin, J., Y. Liu, et al. (2005). "A review on damage mechanisms, models and calibration methods under various deformation conditions." International journal of damage mechanics **14**(4): 299-319.
Lin, J., Y. Liu, et al. (2005). "Development of dislocation-based unified material model for simulating microstructure evolution in multipass hot rolling." Philosophical magazine **85**(18): 1967-1987.
Lin, J. F., T. K. Huang, et al. (1991). "Evaluation of lubricants for cold strip rolling." Wear **147**(1): 79-91.

Liu, Y. (2004). Characterisation of microstructure and damage evolution in hot deformation. Manufacturing and Mechanical Engineering. Birmingham, The University of Birmingham. **Ph.D**.

Liu, Y., D. C. J. Farrugia, et al. (2006). "On micro-damage in hot metal working - part 1: experimental investigation." Engineering transactions **54**(4): 271-287.

Liu, Y., D. C. J. Farrugia, et al. (2005). "A numerical and experimental study of cavitation in a hot tensile axisymmetric testpiece." The Journal of strain analysis for engineering design **40**(6): 571-586.

Liu, Y., J. Lin, et al. (2005). "A numerical and experimental study of cavitation in a hot tensile axisymmetric testpiece." The Journal of strain analysis for engineering design **40**(6): 571-586.

Lorensen, W. E. and H. E. Cline (1987). Marching cubes: A high resolution 3D surface construction algorithm. Proceedings of the 14th annual conference on Computer graphics and interactive techniques, ACM**:** 163-169.

Luo, C. (2001). "Evolution of voids close to an inclusion in hot deformation of metals." Computational materials science **21**(3): 360-374.

Maire, E., O. Bouaziz, et al. (2008). "Initiation and growth of damage in a dual-phase steel observed by X-ray microtomography." Acta Materialia **56**(18): 4954-4964.

Maire, E., O. Bouaziz, et al. (2008). "Initiation and growth of damage in a dual-phase steel observed by X-ray microtomography." Acta Materialia **56**(18): 10.

Maire, E., J. Buffiere, et al. (2001). "Characterization by X-ray computed tomography of decohesion, porosity growth and coalescence in model metal matrix composites." Acta Materialia **49**(11): 2055-2063.

Mamuzic, I., M. Longauerova, et al. (2005). "The analysis of defects on continuous cast billets." METALURGIJA **44**(3): 201-207.

Margevicius, R. (1991). "The effects of hydrostatic-pressure on the mechanical-behavior of NiAl." Scripta metallurgica et materialia **25**(9): 2017-2022.

Mashayekhi, M., S. Ziaei-Rad, et al. (2007). "Ductile crack growth based on damage criterion: Experimental and numerical studies." Mechanics of Materials **39**(7): 623-636.

Medina, S. F., J. I. Chaves, et al. (2007). "Influence of austenite grain size on recrystallisation-precipitation interaction in a V-microalloyed steel." Materials science & engineering. A, Structural materials **447**(1-2): 11-18.

Metaxas, A. C. (1996). Foundations of electroheat: a unified approach. Chichester, John Wiley and Sons Limited.

Mirone, G. (2007). "Role of stress triaxiality in elastoplastic characterization and ductile failure prediction." Engineering fracture mechanics **74**(8): 1203-1221.

Moody, N. R., W. M. Garrison, et al. (1993). "The roll of inclusion and pore content on the fracture-toughness of powder-processed blended elemental titanium-alloys." Metallurgical transactions. A, Physical metallurgy and materials science **24**(1): 161-174.

Moroli, V. and R. Piancaldini Apparatus and methods for control of surface quality of elongated products. C.-O. M. J. I. P. Application. Italy. **PCT/IB2004/052383**.

Munther, P. and J. G. Lenard (1995). "Tribology during Hot, Flat Rolling of Steels." CIRP Annals - Manufacturing Technology **44**(1): 213-216.

New York : Marcel, D. (2004). Mechanical Tribology.

Nicholson, A., D. Smith, et al. (1968). Hot workability testing at united steel companies. ISI Publication 108, The Iron & Steel Institute**:** 161-167.

Norton, F. H. (1929). The creep of steel at high temperatures. New York, McGraw-Hill.

Othman, A. M., J. Lin, et al. (1993). "Comparison of creep rupture lifetimes of single and double notched tensile bars." Acta Metallurgica et Materialia **41**: 17-24.

Pardoen, T. (2006). "Numerical simulation of low stress triaxiality ductile fracture." Computers & Structures **84**(26-27): 1641-1650.

Pardoen, T., D. Dumont, et al. (2003). "Grain boundary versus transgranular ductile failure." Journal of the Mechanics and Physics of Solids **51**(4): 637-665.

Perevezentsev, V. N., V. V. Rybin, et al. (1992). "Overview no. 97: The theory of structural superplasticity - II. Accumulation of defects on the intergranular and interphase boundaries. Accommodation of the grain-boundary sliding. The upper bound of the superplastic strain rate." Acta Metallurgica et Materialia **40**: 895-905.

Petkovic, R. A., M. J. Luton, et al. (1975). "Recovery and recrystallization of carbon steel between intervals of hot working." Canadian metallurgical quarterly **14**(2): 137-145.

Phaniraj, M. P., B. B. Behera, et al. (2006). "Thermo-mechanical modeling of two phase rolling and microstructure evolution in the hot strip mill." Journal of materials processing technology **178**(1-3): 388-394.

Phillion, A., R. Hamilton, et al. (2011). "In situ X-ray observation of semi-solid deformation and failure in Al-Cu alloys." Acta Materialia **59**(4): 1436-1444.

Phillion, A., P. Lee, et al. (2008). "Quantitative assessment of deformation-induced damage in a semisolid aluminum alloy via X-ray microtomography." Metallurgical and materials transactions. A, Physical metallurgy and materials science **39A**(10): 2459-2469.

Porter, D. A. and K. E. Easterling (2001). Phase transformations in metals and alloys Cheltenham : Nelson Thornes.

Puncreobutr, C., P. D. Lee, et al. (2012). "Quantification 3D characterization of solidification structure and defect evolution in Al alloys." Journal of Modelling.

Rajak, S. A. and N. V. Reddy (2005). "Prediction of internal defects in plane strain rolling." Journal of Materials Processing Technology **159**(3): 409-417.

Reed, R. C. (2006). The Superalloys; Fundamentals and Applications, Cambridge University press.

Revidriego, F. J., I. Gutierrez, et al. (1996). "Influence of incomplete dissolution of precipitates on static recrystallization of vanadium microalloyed steels." Scripta materialia **34**(10): 1589-1594.

Rice, J. R. and M. A. Johnson (1970). "The Role of Large Crack Tip Geometry Changes in Plane Strain Fracture." Inelastic Behavior of Solids **McGraw-Hill, N.Y.**

Rice, J. R. and D. M. Tracey (1969). "On the ductile enlargement of voids in triaxial stress fields." Journal of the Mechanics and Physics of Solids **17**(3): 201-217.

Rosochowski, A. and L. Olejnik (1988). "Damage evolution in mild steel." International journal of mechanical sciences **30**(1): 51-60.

San Marchi, C. (2002). "Quasistatic and dynamic compression of aluminum-oxide particle reinforced pure aluminum." Materials science & engineering. A, Structural materials **337**(1-2): 202-211.

Saxena, A. (1997). "Edge cracking in hot-rolled coils of semi-killed steels." Journal of materials engineering and performance **6**(5): 605-610.
Schey, J. A. (1966). "Prevention of Edge Cracking in Rolling by Means of Edge Restraint." Journal of the Institute of Metals **94**: 193-200.
Shercliff, H. R. and M. F. Ashby (1990). "A process model for age hardening of aluminium alloys--i. The model." Acta Metallurgica et Materialia **Vol. 38,** (No. 10): 1789-1802.
Shercliff, H. R. and M. F. Ashby (1990). "A process model for age hardening of aluminum-alloys .1. The model." Acta Metallurgica et Materialia **38**(10): 1789-1802.
Spindler, M. (2004). "The multiaxial creep ductility of austenitic stainless steels." Fatigue & fracture of engineering materials & structures **27**(4): 273-281.
Staub, C. and J. C. Boyer (1996). "An orthotropic ductile damage model for visco-plastic materials." Journal of Materials Processing Technology **60**(1-4): 297-304.
Taylor, G. I. (1938). "Plastic strain in metals." Journal of the Institute of Metals **62**: 307-324.
Thomason, P. F. (1990). Ductile fracture of metals. Oxford, Pergamon Press.
Thomson, P. F. and N. M. Burman (1980). "Edge cracking in Hot-rolled Al-Mg Alloys." Materials Science & Engineering **45**: 95-107.
Titarenko, V., S. Titarenko, et al. (2010). "Improved tomographic reconstructions using adaptive time-dependent intensity normalization." Journal of synchrotron radiation **17**(5): 689-699.
Toda, H., I. Sinclair, et al. (2004). "A 3D measurement procedure for internal local crack driving forces via synchrotron X-ray microtomography." Acta Materialia **52**(5): 1305-1317.
Traiviratana, S., E. M. Bringa, et al. (2008). "Void growth in metals: Atomistic calculations." Acta Materialia **56**(15): 3874-3886.
Trattnig, G., S. Kleber, et al. (2008). "Damage evolution in nickel-base alloy torsion specimens and its influence on subsequent tensile deformability." Engineering Fracture Mechanics **75**(12): 3727-3734.
Troiano, E., P. J. Cote, et al. (1997). "Fatigue Reclamation: The Concept of Self-Healing " Army armament research development and engineering center Watervliet NY Benet labs **A250723**(JUN 97): 14.
Tvergaard (1981). "Influence of voids on shear band instabilities under plane-strain conditions." International journal of fracture **17**(4): 389-407.
Tvergaard (1990). "Analysis of tensile properties for a whisker-reinforced metal matrix composite." Acta Metallurgica et Materialia **38**(2): 185-194.
Tvergaard (1990). "Effect of fiber debonding in a whisker-reinforced metal." Materials science & engineering. A, Structural materials: properties, microstructure and processing **125**(2): 203-213.
Tvergaard, V. and A. Needleman (2001). The modified Gurson model. Handbook of Materials Behavior Models. J. Lemaitre. London, Academic Press. **2:** 430-435.
Vetrano, J. S., E. P. Simonen, et al. (1999). "Evidence for excess vacancies at sliding grain boundaries during superplastic deformation." Acta Materialia **47**(15-16): 4125-4129.

Viggo, T. (1985). "Effect of grain boundary sliding on creep constrained diffusive cavitation." Journal of the Mechanics and Physics of Solids **33**(5): 447-469.
Volterra, V. (1905). "On the distortion of connected elastic solids." Rend. Lincei **5e**(14).
Wang, A., P. F. Thomson, et al. (1996). "Effect of gas pressure on pore closure during hot rolling " 2nd International Conference on Modelling of Metal Rolling Processes(1996): 68-75.
Weck, A. (2007). "Numerical simulations of void linkage in model materials using a nonlocal ductile damage approximation." International journal of fracture **148**(3): 205-219.
Weck, A., D. Wilkinson, et al. (2008). "Observation of void nucleation, growth and coalescence in a model metal matrix composite using X-ray tomography." Materials science & engineering. A, Structural materials: properties, microstructure and processing **488**(1-2): 435-445.
Weinrich, P. F. and I. E. French (1976). "The influence of hydrostatic pressure on the fracture mechanisms of sheet tensile specimens of copper and brass." Acta metallurgica **24**(4): 317-322.
Wierzbicki, T., Y. Bao, et al. (2005). "Calibration and evaluation of seven fracture models." International Journal of Mechanical Sciences **47**(4-5): 719-743.
Wright, T. W. and K. T. Ramesh (2008). "Dynamic void nucleation and growth in solids: a self-consistent statistical theory." Journal of the Mechanics and Physics of Solids **56**(2): 336-359.
WSA. (2009). "World steel producers 2009." 2010, from http://www.worldsteel.org/?action=programs&id=53.
Xia, L. and C. F. Shih (1995). "Ductile crack growth--II. Void nucleation and geometry effects on macroscopic fracture behavior." Journal of the Mechanics and Physics of Solids **43**(12): 1953-1981.
Yoshizawa, M. and H. Ohsawa (1997). "Evaluation of strain-rate sensitivity in superplastic compressive deformation." Journal of Materials Processing Technology **68**(3): 206-214.
Zener (1948). "The micro-mechanism of fracture." Fracturing of metals.
Zhou, Y., R. Qin, et al. (2000). "Reversing effect of electropulsing on damage of 1045 steel." Journal of materials research **15**(5): 1056.
Zhu, G. and S. V. Subramanian (2006). "Ultra-fine grain size control and mixed grains elimination in industrial multi-pass rolling processing." Materials science & engineering. A, Structural materials **426**(1-2): 235-239.